UNIVERSITY OF CALIFORNIA

Los Angeles

# Investigations of Copper-based Catalysts for Electrochemical Carbon Dioxide Reduction

A dissertation submitted in partial satisfaction

of the requirements for the degree

Doctor of Philosophy in Materials Science and Engineering

by

Jin Cai

2022

ABSTRACT OF THE DISSERTATION

Investigations of Copper-based Catalysts for Electrochemical Carbon Dioxide Reduction

by

Jin Cai
Doctor of Philosophy in Materials Science and Engineering
University of California, Los Angeles, 2022
Professor Yu Huang, Chair

The increasing atmospheric carbon dioxide ($CO_2$) level is calling for more efficient $CO_2$ fixation systems to re-balance the carbon cycle. At the same time, $CO_2$ can be a cheap and abundant carbon source for synthesizing various valuable fuels. The renewable-electricity-powered $CO_2$ reduction reaction ($CO_2$RR) offers a means to synthesize various valuable fuels and store intermittent electricity as stable chemical forms. To date, Copper (Cu) remains the most effective electrocatalyst for $CO_2$RR in producing hydrocarbons and oxygenates. However, Cu-based catalysts usually suffer from insufficient product selectivity. Generating mixed products causes a high economic penalty in post-reaction separation, largely limiting the broad implementation of electrochemical $CO_2$RR. A lack of understanding of the complicated reaction mechanism further hindered the catalyst development. Thus, I have focused on Cu-based electrocatalytic $CO_2$RR catalysts with high efficiency through surface defects and co-catalyst engineering. Three types of Cu-based catalysts have been designed and investigated; Cu foil with rich twin boundaries (tw-Cu), Cu-Ag NWs with the atomically intimate interface, and trimetallic CuPdAg plates, which successfully improved $CO_2$RR performance. Electrochemical and advanced spectroscopies coupling with computational simu-

lation provided mechanistic understandings of the influence of defect engineering on $CO_2RR$ selectivity.

Overall, these researches demonstrate that tuning surface defect structure and atomic arrangement of Cu-based co-catalysts are effective strategies in improving the activity and selectivity of electrocatalytic $CO_2RR$, thus suggesting a path towards rational designs of Cu-based catalysts for tunable $CO_2RR$.

The dissertation of Jin Cai is approved.

Qibing Pei

Ximin He

Xiangfeng Duan

Yu Huang, Committee Chair

University of California, Los Angeles

2022

*To my parents, Lingcang Cai and Lili Jia,*

*who are always there for me.*

TABLE OF CONTENTS

LIST OF FIGURES

LIST OF TABLES

# ACKNOWLEDGMENTS

First and foremost, I would like to express my deepest gratitude to Prof. Yu Huang, who provided me with great research opportunities, supported me, and guided me throughout my Ph.D. study. She has a great impact on my life and work ethic. She taught me that research should be driven by intrinsic curiosity and directed me to think independently and critically. Most impotently, she trained me to become the independent researcher I am today. None of the achievements would be possible without her guidance, and I am forever grateful.

I would also like to thank all my committee members, Prof. Qibing Pei, Prof. Ximin He, and Prof. Xiangfeng Duan. Thank you for the insightful comments and constructive advice. I also learned a lot from asking questions and communicating with other UCLA members. Matthew Mecklenburg, Jared, Judy, Ivo, Adam, and Mike at CNSI; Ignacio and Bob at the chemistry department and Noah at Nanolab are my mentors in tool operation and helped me a lot with troubleshooting. Thank you all.

Moreover, I would like to thank my lab mates for their support, advice, and friendship during these years. I'm especially grateful to Dr. Chungseok Choi and Dr. Enbo Zhu, who mentored me at the early stage of my Ph.D. and provided me with many valuable suggestions for my research. I would also like to thank Yang Liu, Haotian Liu, Dr. Huaying Ren, and Jin Huang for their collaboration and help with my projects. I want to thank Chengzhang Wan, Dr. Zipeng Zhao, Zeyan Liu, Bosi Peng, Ao Zhang, and Dr. Hongtu Zhang for valuable insights and discussions that helped me design and understand the electrochemical $CO_2$ reduction experiment. I'd like to thank my office mates: Dong Xu, Dr. Peiqi Wang, Dr. Guangyan Zhong, Dr. Zhong Wan, Dr. Qi Qian, Dr. Dehui Zhang, and Boxuan, whom I have enjoyed working with and learning from. I had many delightful lunch and coffee break discussions with them. Lastly, I would like to thank Dr. Bocheng Cao, Dr. Michelle Flores, Dr. Zhihong Huang, Dr. Zhaoyang Lin, Xucheng Yan, Dr. Sung-joon Lee, and all other group members and collaborators. I feel very fortunate to work with you all.

Next, I want to thank my collaborators outside the Materials Science and Engineering department who instilled valuable insights. I'm grateful to Prof. Emily A. Carter and Dr. Qing Zhao at Princeton University; Dr.John Mark P. Martirez at the Department of Chemical and Biomolecular Engineering, UCLA, for their input on the simulation part of the work. I enjoyed our weekly meeting and learned a lot about not just the fundamentals of $CO_2$ reduction but also the skill of planning, organizing, and presenting scientific works. I want to thank Prof.Chih Chen and Wei-You Hsu at National Yang Ming Chiao Tung University (NYCU), who are extremely kind in providing samples and exchanging ideas. I hope our paths will cross again in the future. A big thank you to Dr. Mingjie Xu at UCI, who helped me with the EBSD measurements.

To the friends who have brightened my graduate days, even in the darkest hours, I'd like to thank them for being part of my life at UCLA. Zihang, Xiaotian, Xia Sang, Tianyi and Dong. A special thank you to Juncheng, who has been a constant source of support and encouragement during the challenges of graduate school.

In addition, this work, and my graduate career as a whole, has been supported financially by the Office of Naval Research (ONR) under grant no. N000141712608 and by the University of California, Los Angeles.

Lastly, I would like to thank my parents for the best childhood I could ever dream about. I was surrounded by love and company. They encouraged me to be curious and explore the world fearlessly. I'm most grateful that my parents guided me to observe the world from multiple perspectives and nurtured a child's imagination in creativity.

Chapter two is a version of [Submitted manuscript] Author list: Jin Cai, Qing Zhao, Wei-You Hsu, Chungseok Choi, John Mark P. Martirez, Chih Chen, Jin Huang, Emily A. Carter, and Yu Huang.DFT simulation of $CO_2$ reduction process on Cu is conducted by Qing Zhao.

Chapter Three is a version of [Nano Research] Author list: Chungseok Choi, Jin Cai,

Changsoo Lee, Hyuck Mo Lee, Mingjie Xu, and Yu Huang. 2021, 14(10), 3497-3501.DOI: https://doi.org/10.1007/s12274-021-3639-x.

# VITA

2016 B.S.
Materials Science and Engineering,
Wuhan University of Technology, Wuhan, China

2017-2022 Graduate Student Researcher
Department of Materials Science and Engineering
University of California, Los Angeles
Los Angeles, CA

# PUBLICATIONS

Oral presentation at ACS Fall 2022 National Meeting  Exposition in Chicago, IL, August 21 - 25, 2022. Division: Division of Energy and Fuels. Session: Electrochemistry-Enabled Catalysis for Energy, Chemicals  Materials. Title: Highly selective electrochemical reduction of $CO_2$ into Methane on Nanotwinned Cu.

Chungseok Choi, Jin Cai, Changsoo Lee, Hyuck Mo Lee, Mingjie Xu, and Yu Huang. Intimate atomic Cu-Ag interfaces for high $CO_2$RR selectivity towards $CH_4$ at low over potential. Nano Research, 14(10):34973501, 2021.

Qi Qian, Huaying Ren, Jingyuan Zhou, Zhong Wan, Jingxuan Zhou, Xingxu Yan, Jin Cai,Peiqi Wang, Bailing Li, Zdenek Sofer, et al. Chiral molecular intercalation superlattices. Nature, 606(7916):902908, 2022.

Chungseok Choi, Soonho Kwon, Tao Cheng, Mingjie Xu, Peter Tieu, Changsoo Lee, Jin Cai, Hyuck Mo Lee, Xiaoqing Pan, Xiangfeng Duan, et al. Highly active and stable stepped cu surface for enhanced electrochemical $CO_2$ reduction to $C_2H_4$. Nature Catalysis, 3(10):804812, 2020.

Enbo Zhu, Wang Xue, Shiyi Wang, Xucheng Yan, Jingxuan Zhou, Yang Liu, Jin Cai, Ershuai Liu, Qingying Jia, Xiangfeng Duan, et al. Enhancement of oxygen reduction reaction activity by grain boundaries in platinum nanostructures. Nano Research, 13(12):33103314, 2020.

Enbo Zhu, Xucheng Yan, Shiyi Wang, Mingjie Xu, Chen Wang, Haotian Liu, Jin Huang, Wang Xue, Jin Cai, Hendrik Heinz, et al. Peptide-assisted 2-d assembly toward free-floating ultrathin platinum nanoplates as effective electrocatalysts. Nano letters, 19(6):37303736, 2019.

# CHAPTER 1

# Introduction

In this chapter, I will start with introducing the research background of electrostatic carbon dioxide ($CO_2$) reduction ($CO_2$RR) on copper (Cu)-based catalysts, including the motivation of this technology application in renewable energy, followed by the description of performance metric, research challenges and development of Cu-based catalysts for $CO_2$RR. Central to this discussion will be the relationship between the structure of the catalyst and the kinetics of $CO_2$RR pathways. The aim of this chapter is not to cover the background exhaustively but rather to selectively discuss some advances and pertinent challenges in this field. My research themes seek to understand the structural-performance correlation of electrochemical $CO_2$RR with the ultimate objective of effective catalyst design and control of the reaction.

## 1.1 Motivation

The electrochemical $CO_2$ reduction reaction ($CO_2$RR) study is primarily driven by the interests of promoting renewable energy usage, decreasing $CO_2$ emission, and eventually converting human society energy consumption to a more efficient and environmentally friendly mode. According to the U.S. Energy Information Administration (EIA) Annual Energy Outlook[1], global energy usage has been projected to continually increase while traditional fossil fuel is still the primary energy source, emitting $CO_2$ during energy extraction. Based on the current energy consumption mode, there is a conflict between maintaining global economic growth and preventing further carbon accumulation in the atmosphere. Though carbon-free renewable energy like solar, wind, and hydropower are predicted to gain more market,

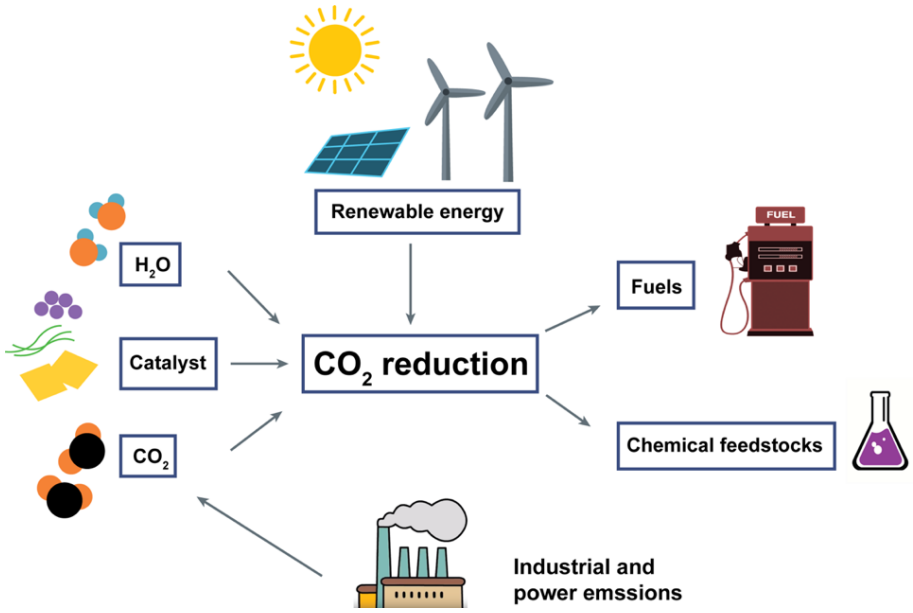


**Figure 1.1:** Schematic of a $CO_2$ reduction process using renewably sourced electricity.

their unpredictable and inconsistent nature limits the further application of these renewable sources.[2] $CO_2$RR driven by clean electricity is a potential technology to store these intermittent renewable energies in stable and convenient forms to utilize chemicals while consuming $CO_2$ at the same time. Local industry emissions containing high concentration $CO_2$, such as breweries, cement manufacturing, and petroleum refineries facilities, can be transferred to the value-added chemicals through efficient electrochemical $CO_2$ reduction technology utilizing inconsistent clean electric power sources. Storing these renewable energies in chemical form by reducing $CO_2$ to fuels and chemical feedstocks is a promising solution for renewable energy output intermittency and transportation problems. Figure 1.1 illustrates the overall path of combining $CO_2$ reduction with clean power utilization.

## 1.2 Overview of Electrochemical $CO_2$ Reduction

The electrochemical $CO_2$ reduction includes a cathode that reduces $CO_2$ into hydrocarbons/oxygenates and an anode that supplies a corresponding oxidative process. Most com-

monly, the anode reaction is water oxidation ($E^o$ = 1.23 V vs. the reversible hydrogen electrode (RHE))[3]:

$$2H_2O \rightarrow O_2 + 4H^+ + 4e^- \tag{1.1}$$

The cell is filled with electrolyte as a conductive medium. The electrolyte can be liquid, solid, or a combination of both. The cathode chamber and the anode chamber are commonly separated by a membrane that conducts ions with liquid electrolyte. The separation prevents the crossover of anode and cathode materials, also the reduction and oxidation products. Under their collective effect, the possibility of cross-contamination and parasitic side reactions can be raised. Figure 1.2 show a typical H-shaped, two-compartment electrochemical cell (H-cell) setup, which is largely used in the fundamental study of $CO_2$ reduction reaction.

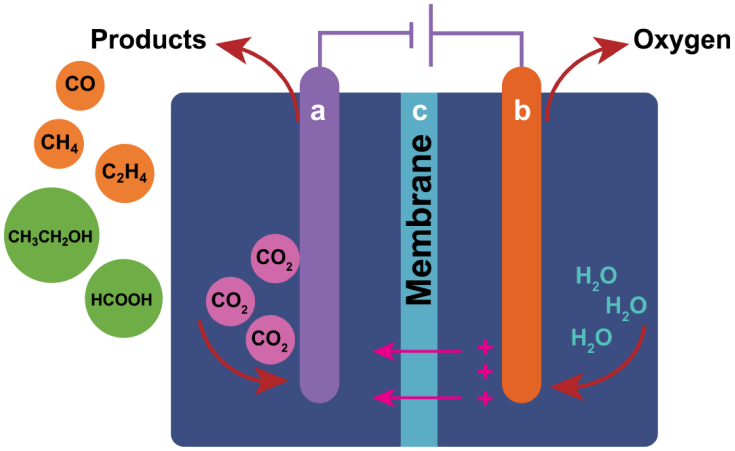


**Figure 1.2:** Schematic of a typical H-cell for electrolytic $CO_2$ reduction. The principal components are (a) the cathode reducing $CO_2$, (b) the anode conducting a corresponding oxidative reaction supplying both protons and electrons to the cathode, (c) the membrane (including proton exchange membrane (PEM), anion exchange membrane (AEM), and bipolar membrane (BPM)). Both the cathode chamber and anode chamber are filled with electrolyte-conducting electrons and protons.

$CO_2$ reduction reaction, including multiple proton-electron transfers and accounts for a

**Table 1.1:** List of commonly reported cathodic half cell reactions in $CO_2$RR and their equilibrium potentials table is adapted from Ib Chorkendorf. et al.[3]

| **$CO_2$RR Products** | **# e$^-$** | **Reaction** | **E$^o$ (V vs. RHE)** |
|---|---|---|---|
| **Formic acid** | 2 | $CO_2 + 2H^+ + 2e^- \rightarrow COOH_{(aq)}$ | -0.12 |
| **Carbon monoxide** | 2 | $CO_2 + 2H^+ + 2e^- \rightarrow CO_{(g)} + H_2O$ | -0.1 |
| **Methanol** | 6 | $CO_2 + 6H^+ + 6e^- \rightarrow CH_3OH_{(aq)} + H_2O$ | 0.03 |
| **Methane** | 8 | $CO_2 + 8H^+ + 8e^- \rightarrow CH_{4(g)} + 2H_2O$ | 0.17 |
| **Acetic acid** | 8 | $CO_2 + 8H^+ + 8e^- \rightarrow CH_3COOH_{(aq)} + 2H_2O$ | 0.11 |
| **Acetaldehyde** | 10 | $CO_2 + 10H^+ + 10e^- \rightarrow CH_3CHO_{(aq)} + 3H_2O$ | 0.06 |
| **Ethanol** | 12 | $CO_2 + 12H^+ + 12e^- \rightarrow C_2H_5OH_{(aq)} + 3H_2O$ | 0.09 |
| **Ethylene** | 12 | $CO_2 + 12H^+ + 12e^- \rightarrow C_2H_{4(g)} + 4H_2O$ | 0.08 |
| **Ethane** | 14 | $CO_2 + 14H^+ + 14e^- \rightarrow C_2CH_{6(g)} + 2H_2O$ | 0.14 |
| **Propionaldehyde** | 16 | $CO_2 + 16H^+ + 16e^- \rightarrow C_2H_5CHO_{(aq)} + 5H_2O$ | 0.09 |
| **Propanol** | 18 | $CO_2 + 18H^+ + 18e^- \rightarrow C_3H_7OH_{(aq)} + 5H_2O$ | 0.1 |

range of possible reactions. The most commonly reported $CO_2$RR reduction products, the corresponding reactions, and the standard reduction potentials for these species are listed in table1.1.[3] The standard reduction potentials are calculated by the Gibbs free energy of the reaction. It is worth noting that along $CO_2$RR, hydrogen evolution reaction (HER) with standard reduction potential E$^o$ of 0 (V vs. RHE) serves as a competing reaction:

$$2H^+ + 2e^- \rightarrow H_2 \tag{1.2}$$

The similar standard reduction potential ranges of HER and multiple products of $CO_2$RR result in producing mixed products, which leads to a high economic penalty in post-reaction separation, thus essentially limiting the broad implementation of electrochemical $CO_2$RR.

$CO_2$ reduction is a thermodynamically uphill reaction that demands energy input. The actual electrode potentials required to drive the $CO_2$RR reductions are more negative than the equilibrium potential due to the kinetic barriers of elementary steps. The Arrhenius

equation describes the relationship between reaction rate and activation energy ($E_a$):

$$k = ve^{\frac{-E_a}{k_B T}} \tag{1.3}$$

Where k is the rate constant, v is a prefactor, $k_B$ is the Boltzmann constant, and $T$ is the absolute temperature. The reaction rate increases exponentially as the activation energy decreases. Heterogeneous catalysts lower the activation barrier of the chemical reactions by changing the energy levels of bound intermediates relative to one another. The Sabatier principle states that "an ideal catalyst must bind to the reactant at an optimum strength." If the binding is too weak, the reactant rarely interacts with the catalyst, whereas if the binding is too strong, the reactant does not desorb from the surface and prohibits further interaction."[4] Figure 1.3 shows the most favorable elementary steps for carbon monoxide (CO) and formate ($HCOO^-$) formation (simplest products of $CO_2$RR, needing only two proton-electron pairs) calculated in the explicit water model.[5] For $CO_2$ reduction to CO, the rate-determining steps (RDS) is the physisorbed $CO_2$ to chemisorbed $CO_2$ ($*CO_2$), with a free energy barrier of $\Delta G = 0.43$ eV, followed by protonating $*CO_2$ to form $*COOH$ and then dissociating $*COOH$ to form $*CO$. While for $HCOO^-$ formation, the RDS is the reaction of physisorbed $CO_2$ with a proton (along with electron transfer) to form $HCOO^-$, with a free energy barrier $\Delta G = 0.80$ eV.[5]

The overall rate-limiting steps and kinetic barriers for each product dependent highly on the catalyst structure and reaction environment. An ideal catalyst should be able to achieve a high rate of reaction and high selectivity toward desired product by controlling the kinetics of the reaction.

The $CO_2$RR catalysts researched in this work is operated under aqueous condition (0.1 M $KHCO_3$). The $CO_2$ dissolution process is shown below[6]:

$$CO_2(g) \rightleftarrows CO_2(aq) \tag{1.4}$$

$$CO_2(aq) + H_2O \rightleftarrows H_2CO_3(aq) \tag{1.5}$$

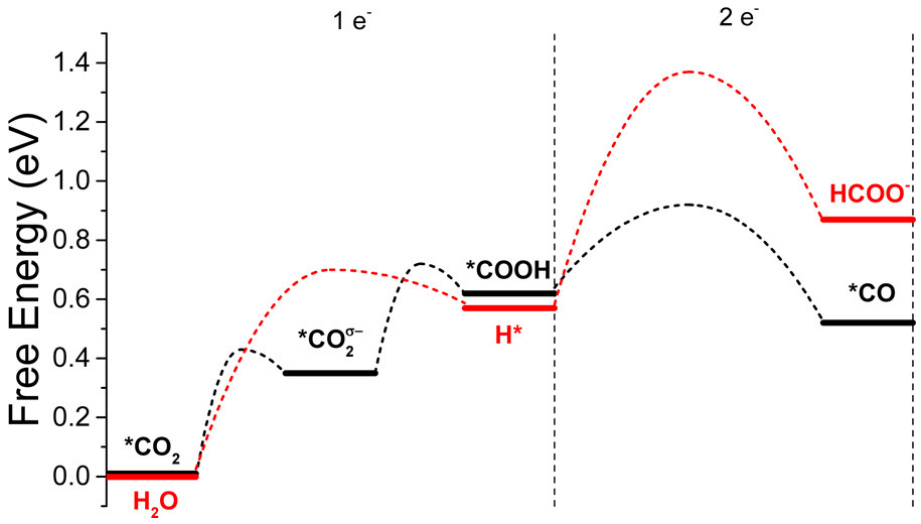


**Figure 1.3:** Most Favorable Kinetic Pathways for the Electrochemical Reduction of $CO_2$ to $*CO$ and Formate ($HCOO^-$) in Water Solvent at pH 7.[5]

$$H_2CO_3(aq) \rightleftarrows H^+(aq) + HCO_3^-(aq) \tag{1.6}$$

The solubility of $CO_2$ can be calculated by Henrys law under ideal condition[7]:

$$[CO_2]_{aq,0} = K_0[CO_2]_g \tag{1.7}$$

At 1 atm, the $CO_2$ concentration in water is approximately 34 mM.[6] During the $CO_2$ reaction, the local pH is increased due to proton consumption, which further decreases the concentration of $CO_2$ near the catalyst surface. The potential also affects the reaction pathway. It is observed in the experiment that there is a potential dependence of products. CO-CO dimerization is favored under low potential. It has been found that increasing the size of alkali cation tends to enhance the selectivity for CO and $C_2H_5OH$. Overall, the local pH, applied potential, and local ion concentrations should be considered when optimizing the catalyst's performance.

## 1.3 Performance Metrics and Challenges in Electrochemical $CO_2$ Reduction Reactions

### Current Density

Current density, denoted by j, represents the rate at which products are generated. It indicates the catalyst activity. Current density equals the total current divided by the geometric area of the active catalyst at a given potential. Electrochemically active surface (ECSA) is also used to account for the explicit activity of the catalyst. In this study, ECSA is estimated by measuring the double-layer capacitance of the electrode-electrolyte interface.[8] Double-layer capacitance can be measured by performing cyclic voltammetry (CV) in a potential range where no Faradaic processes occur. In this range, the measured current is only due to the charge of the electrochemical double layer. The charging current, $i_c$, is related linearly to the scan rate v in CV scans, and the slope is equal to the double-layer capacitance ($C_{DL}$):

$$C_{DL} = \frac{i_c}{v} \tag{1.8}$$

This measured capacitance ($C_{DL}$) can be compared to a reference surface to obtain a relative roughness factor (SRF) for the electrocatalyst:

$$SRF = \frac{C_{DL_{sample}}}{C_{DL_{reference}}} \tag{1.9}$$

ESCA can be calculated by multiplication of the SRF and the geometric surface area (A):

$$ECSA = SRF \times A \tag{1.10}$$

A high current density is essential for industrialized application of $CO_2$ electrolyzer since it decreases the overall electrolyzer size, which leads to lower capital investment. Current density is affected by multiple factors, such as catalyst structure, catalyst loading, and transport rate of reactants and products to and from the electrode. The current density of $CO_2$RR

is limited, especially for the low solubility of $CO_2$ in water, along with poor diffusion characteristics near the catalyst surface. Reported current density has been stagnating at less than 100 mA/cm$^2$ in H-cell due to the limited $CO_2$ solubility in aqueous electrolyte, while over 300 mA/cm$^2$ are suggested for commercial usage to make capital costs minimal versus operating costs for $CO_2$RR.[9] Flow cell setups combined with the membrane electrode assembly (MEA) are reported to overcome the limitation of $CO_2$ diffusion and increase current density effectively. Strasser's group has reported a 700 mA/cm$^2$ current density using a nitrogen-doped porous carbon catalyst in the flow cell.[10] Sargent's group has reported an ethylene partial current density of 1.3 A/cm$^2$ with a Cu-catalyst: ionomer bulk heterojunction (CIBH) architecture in an ultraslim flow cell.[11]

**Faradaic Efficiency (FE)**

The Faradaic Efficiency (FE) describes the selectivity of $CO_2$ reduction. It is the ratio between the current contribution to the specific product and the total current. Higher target product FE is desirable as there are usually multiple products generated from a single catalyst.

**Overpotential**

The overpotential is the absolute difference between a product's applied potential and the thermodynamic equilibrium potential. Reducing overpotentials lowered the overall power input and increased the energy transfer efficiency.

**Stability**

Reaction stability describes the degradation of the catalyst along with the whole electrochemical system. It is crucial for commercial catalyst usage as the performance should be constant during operation. Low stability increases the replacement and maintenance costs.

PEM water-splitting electrolyzers have been demonstrated to operate beyond 20 000 h under mild conditions.[12] However, reported $CO_2$ electrolyzers usually fail with 20 hours of operation in H-cell. The low stability of the $CO_2$ electrolyzer is usually due to the catalyst structure break-off under negative voltage, impurity from the electrolyte, or counter electrode deposition on the catalyst surface. Liu et al. found that they could run a $CO_2$ electrolyzer at 200 mA/ $cm^2$ for 3,800 h at room temperature using a zero-gap cell configuration.[13]

**Challenges**

$CO_2$RR is a complicated reaction, and research on $CO_2$RR is relatively young compared to the water electrolyzer. The cost of electrochemical $CO_2$RR mainly comes from the electricity input, product separation, and electrolyzer maintenance.[14] To scale $CO_2$RR for commercialized utilization, the activity, selectivity (FE), and stability should meet the techno-economic requirement. In other words, the electrolyzer system should be operated to produce a single valuable product with high current density at low overpotential for long time operation. Significant improvement is required to make $CO_2$RR competitive with conventional chemical products.[15] Several economic analysis[14,16,17] has been reported to evaluate the desired range of $CO_2$RR performance metrics, which largely depend on the renewable electricity price (FE >80% for $C_2$ products at >500 mA/$cm^2$ are preferred for profitable production).[17]

A greater fundamental understanding of the catalysis mechanisms is needed to support the rational design of the catalyst and electrolyzer system. Theoretical simulation works have provided valuable insight and promoted the $CO_2$RR mechanism studies. However, they encountered issues that oversimplified the model and resulted in gaps between simulation findings and experiment observation. For example, DFT studies with generalized-gradient approximations to the exchange-correlation (XC) functional predict $*$CO adsorption on Cu (111) to be hollow site[18] while atop site[19,20] were observed by low-energy electron diffraction (LEED) and reflection absorption infrared spectroscopy (RAIRS) experimentally. Moreover, theoretical work applies different simplifying assumptions in modeling results in diverse sim-

ulation results, making it hard to compare the binding energy of intermediates and activation barriers between literature. In-situ investigation of the electrochemical reaction process is critical to complete to mechanism map. However, a higher detection limit of intermediates, better spatial resolution, time resolution, and smaller sampling depth are currently challenging.[21]

## 1.4 A Look at the Electrochemical $CO_2$ Reduction Pathways on Cu

$CO_2$RR on Cu is a complex reaction network involving many possible intermediates and reaction pathways that scientists have not fully revealed. Understanding the reaction mechanisms of CO2RR is essential for the researcher to design and develop effective catalysts. The mechanism understanding is especially limited when the carbon numbers of products increase. Still, progress has been made since Hori et al.[22] first reported the $CO_2$RR on Cu in 1985, which helps sketch a preliminary reaction pathways map of $C_1$ and $C_2$ Products as discussed and summarized in figure 1.4[3].

For the $C_1$ product, its commonly agreed that the first limiting step is the adsorption of $CO_2$[23], as described in the previous section. $*$COOH, which binds to the catalyst through the carbon atom, is the key intermediate for the CO pathway. $*$OCHO which binds through oxygen is the key for $HCOO^-$ formation. Norskov, Jaramillo, and coworkers found volcano trends of $*$COOH and $*$OCHO binding energy for the activity of $CO_2$RR to CO and $HCOO^-$ based on experimental and theoretical studies.[24] $*$CO, formed through $*$COOH, is the key intermediate to products requiring more than 2 electrons transfer. It is found that CO reduction gives similar products (except formate) with $CO_2$, which suggests $*$CO is intermediate for products requiring more than two electrons transfer.[25,26] The following limiting step in forming $C_1$ hydrocarbon has been proposed to be CO protonation to $*$COH[27] or $*$CHO[28,29], which further reduces to methane ($CH_4$) or methanol ($CH_3OH$). For $C_2$ products, the C-C

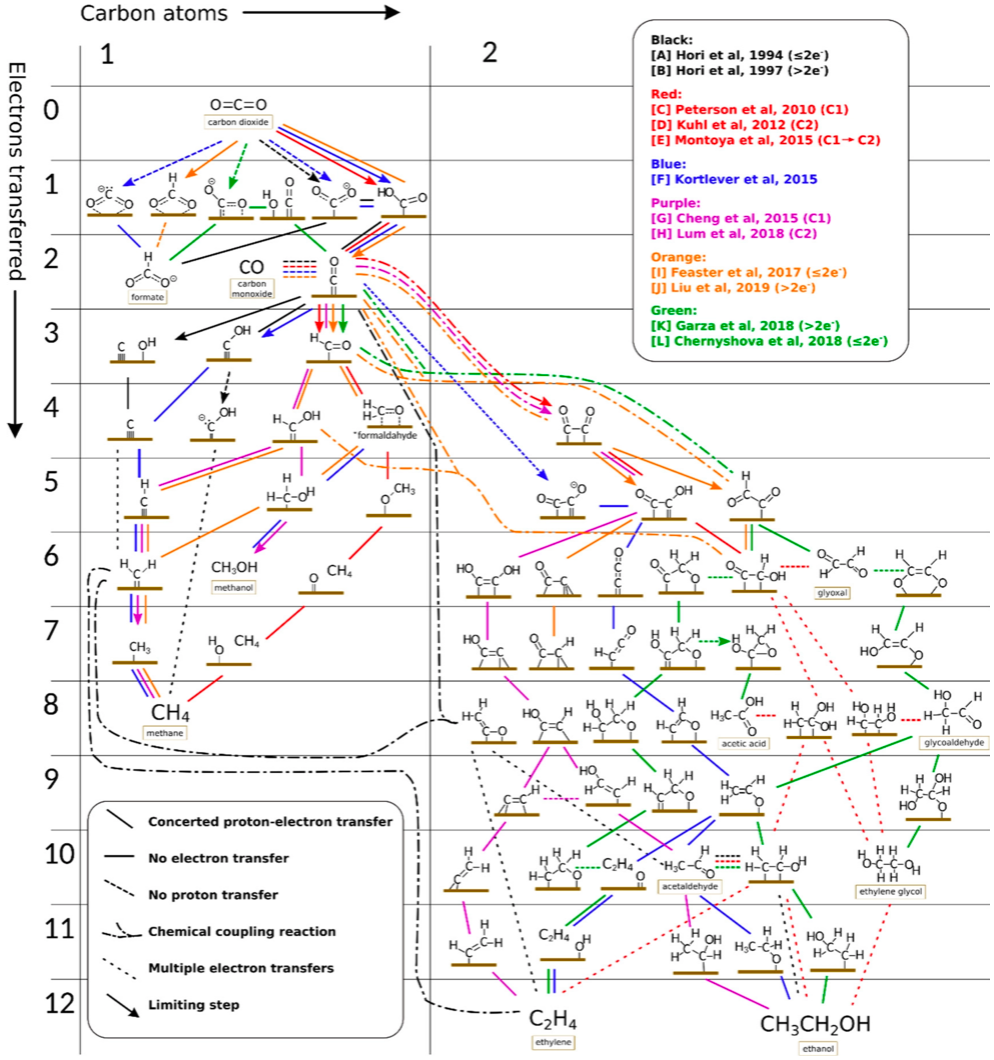


**Figure 1.4:** Possible mechanistic pathways of $CO_2$ reduction to $C_1$ and $C_2$ products on polycrystalline copper, grouped into different colored reaction schemes taken from the works in the top-right legend (respective references can be found in the original paper of Nitopi et al.[3]). The bottom-left legend states the meaning of the texture of the lines connecting intermediates. The image is adapted from Nitopi and co-workers from reference 3.

bond formation has been proposed mainly through:

$$*CO + *CO \longrightarrow OC**CO \xrightarrow{H^+ + e^-} OC**COH \ or \ O*CCHO \tag{1.11}$$

$$*CO + *CHO \xrightarrow{H^+ + e^-} O*CCHO \tag{1.12}$$

$$*CHO + *CHO \rightarrow *OCHCHO* \tag{1.13}$$

$$*COH + *CHO \rightarrow *COHCHO \tag{1.14}$$

$$*COH + *COH \rightarrow *COH*COH \tag{1.15}$$

The dimerization of ∗CO forming ∗OCCO is supported by theoretical simulation[29,30] and time-resolved attenuated total reflection-surface enhanced infrared absorption spectroscopy (ATR-SEIRAS) experiment[31]. The coupling of ∗CHO to form ∗OCHCHO∗,[32] coupling between ∗CHO, and ∗CO to form O∗CCHO at higher overpotentials are supported by the simulation.[30,33,34] These studies suggest that the C-C coupling process is sensitive to the catalysts' composition, structure, and reaction environment. The key factors determine whether the C-C coupling is kinetically favorable, including the local ∗CO concentration, the ∗CO binding energy on the catalyst, and the hydrogenation of ∗CO, if ∗CHO plays a role in the coupling process.[23] There is competition for the shared intermediates between the $C_1$ and $C_2$ pathways. The following chapter will discuss in detail the control of the reaction toward a single product.

## 1.5 Engineering of Cu-based $CO_2$ Reduction Reaction Catalyst

Much effort has been put into studying and engineering Cu-based catalysts, including adjusting the crystal size,[35] exposed facets,[36–38] defect,[39,40] strain engineering,[41–43] adjusting the Cu oxidation state[44,45], and bimetallic catalysts design[46,47]. In the following discussion, I will highlight the Cu facets, defect engineering, and bimetallic catalysts designing strategies which are the focus of this dissertation.

**Table 1.2:** The measurements were performed by chronopotentiometriy at 5 mA/cm$^2$ in 0.1 M $KHCO_3$. Table is adapted from Hori et al.[48,49]

| Cu orientation | Potential V vs. RHE | FE % | | | | | | |
|---|---|---|---|---|---|---|---|---|
| | | $CH_4$ | $C_2H_4$ | CO | Alc. | Ald. | HCOOH | $H_2$ |
| (100) | -1 | 30.4 | 40.4 | 0.9 | 12.0 | 4.4 | 3.0 | 6.8 |
| (111) | -1.15 | 46.3 | 8.3 | 6.4 | 3.3 | 2.7 | 11.5 | 16.3 |
| (110) | -1.15 | 49.5 | 15.1 | 0 | 7.4 | 3.1 | 6.6 | 18.8 |
| (311) | -0.97 | 36.0 | 23.8 | 2.6 | 5.2 | 3.4 | 14.0 | 13.3 |
| (711) | -0.94 | 5.0 | 50.0 | 1.1 | 14.2 | 6.4 | 4.6 | 15.6 |
| (210) | -1.12 | 64.0 | 13.4 | 2.2 | 7.3 | 1.5 | 5.5 | 7.0 |
| (510) | -0.98 | 8.1 | 42.3 | 2.1 | 29.5 | 5.6 | 2.9 | 10.5 |
| (610) | -0.97 | 7.6 | 44.7 | 0.9 | 29.3 | 2.7 | 1.4 | 9.0 |
| (810) | -0.98 | 6.4 | 45.1 | 1.4 | 28.8 | 2.0 | 1.5 | 8.7 |

Hori et al. studied $CO_2$RR on single-crystal copper prepared by mechanical and electrochemical polishing.[48,49] The product distribution for each facet is summarized in table 1.2. Among the three low-indexed facets, i.e. (111), (100), and (110), (100) is the most selective toward ethylene ($C_2H_4$), while (111) and (110) favor the production of $CH_4$. The reason behind this facet-dependent product distribution is still not entirely elucidated. Simulation work suggests this can be attributed to stronger CO binding[19] and lower CO dimerization barrier on (100) compared to (111),[50]. However, Cuenya et al.[51] recently published a work studying the $CO_2$RR on atomically well-ordered Cu(100) and Cu(111) flat surfaces under the ultrahigh vacuum (UHV) condition. Contrary to previous reports, they find that atomically ordered Cu(100) and Cu(111) favor $H_2$ production. A larger amount of hydrocarbons are generated only when defects are introduced to the flat surface by etching and plasma treatment. Unwin et al.[52] utilize scanning electrochemical cell microscopy coupled with

electron backscatter diffraction (EBSD) on polycrystal Cu. They show that the $CO_2$RR activity scales with the step and kink density. These works demonstrate the importance of considering defects in analysis, as most Cu-based catalysts reported in $CO_2$RR studies contain defects such as kinks, steps, dislocations, and grain boundaries. Even for single crystal catalysts, surface reconstruction during the $CO_2$RR could introduce defects-sites and further complicate the research. On the other hand, there is a great chance of utilizing defect engineering to improve the catalyst. Choi et al.[39] synthesized Cu nanowires with rich surface steps through in situ electrochemical activation, which shows $FE_{C_2H_4} > 70\%$ and 200 hours of stability. Their simulation work demonstrates a higher barrier for the $C_1$ path, along with a slower HER on the stepped surface compared with that of $C_2$, which leads to the greatly enhanced selectivity towards $C_2H_4$. The enhanced $FE_{C_2H_4}$ on defects has also been verified by Zhang and co-workers.[53] In their study, a Cu nanosheet with 2-14 nm nanodefects achieve a $FE_{C_2H_4}$ of 83%. They found that the nanodefects can enrich the local $*$CO and hydroxide ($OH^-$) concentration, thereby accelerating the C-C coupling.

However, defects include a large group of structures, including vacancies, dopants, dislocations, and grain boundaries. The explanation of the defect contribution toward $CO_2$RR is diversified. The assumption mainly includes stronger $C_2$ intermediate binding on low coordinated sites and local lattice strain in the defective site, which adjust the electronic structure.[42] Still, the study of the specific defect type is limited due to the lack of close defect structure control. Well-defined defective sites, in-situ characterization of catalyst structure, and examing local $CO_2$RR product production at the atomic scale are needed to reveal the catalytic role of each type of defect site.

Besides defect engineering, another way of tuning the reactivity of a catalyst is by designing the bimetallic structure. Scaling relations limit the design flexibility on a single catalysis site.Taking the $CO_2$RR to CO pathway as an example, $CO_2$ first proceeds to $*$COOH, followed by a proton-coupled electron transfer, leading to the formation of $*$CO. Next, $*$CO desorbs from the catalyst forming the gaseous CO product. Here, both $*$COOH and $*$CO

interact with the catalyst through C-metal bonds. As $CO_2$RR intermediates bind on a catalyst through similar C or O bonds, when one adsorbate binds more strongly/weakly, similar adsorbates tend to bind more strongly/weakly on the catalyst as well. Due to linear scaling relations, designing a catalysis site with ideal $*$COOH binding for forming $*$CO would likely result in non-ideal $*$CO binding for $*$CO desorption. Therefore, the binding energy for activation or release will be non-optimal, especially for more reduced products, unless scaling relations are broken.

Designing CuM (M denotes metal elements) structure which aligns Cu with secondary atoms that change the geometric and electronic structure of Cu is a promising strategy to break the linear scaling relationship and optimize multiple elementary steps of $CO_2$RR. Incorporating foreign elements into Cu supplies diverse catalysis sites that can be optimized for each step separately. Experiments studies have verified that both the structure and composition of CuM affect the catalytic performance. Jia et al. reported taht an electrodeposited CuAu alloy, with optimal $Cu_{63.9}Au_{36.1}$ composition, exhibited an FE of 15.9% for methanol ($CH_3OH$), which is 19 times higher than that of pure Cu.[54] This study claimed the binding of $*$CO was likely optimized for $CO_2$RR toward alcohols in this Cu-Au system. Ma et al. studied CuPd catalysts with ordered, disordered, and phase-separated atomic arrangements.[47] They found that the phase-separated CuPd achieves higher selectivity (>60%) for $C_2$, which may arise from a favorable geometric arrangement for molecular distance and low steric hindrance for C-C coupling.

In short, this chapter provided an overview of $CO_2$RR topics and discussed the background of Cu-based catalyst development that will be further extended in this thesis. Large improvements in efficiency and selectivity have been made by defects and Cu-M bimetallic structure engineering. In the few examples provided, the two approaches are promising in breaking the scaling relationship geometrically and controlling the mixed reaction pathway to the desired direction.

## Bibliography


[1] U EIA. Us energy information administration annual energy outlook 2020. *US Department of Energy: Washington, DC, USA*, 2020.

[2] Yael Parag and Benjamin K Sovacool. Electricity market design for the prosumer era. *Nature energy*, 1(4):1–6, 2016.

[3] Stephanie Nitopi, Erlend Bertheussen, Soren B Scott, Xinyan Liu, Albert K Engstfeld, Sebastian Horch, Brian Seger, Ifan EL Stephens, Karen Chan, Christopher Hahn, et al. Progress and perspectives of electrochemical $CO_2$ reduction on copper in aqueous electrolyte. *Chemical reviews*, 119(12):7610–7672, 2019.

[4] Paul Sabatier. Hydrogénations et déshydrogénations par catalyse. *Berichte der deutschen chemischen Gesellschaft*, 44(3):1984–2001, 1911.

[5] Tao Cheng, Hai Xiao, and William A Goddard III. Reaction mechanisms for the electrochemical reduction of $CO_2$ to CO and formate on the Cu (100) surface at 298 k from quantum mechanics free energy calculations with explicit water. *Journal of the American Chemical Society*, 138(42):13802–13805, 2016.

[6] Meenesh R Singh, Ezra L Clark, and Alexis T Bell. Effects of electrolyte, catalyst, and membrane composition and operating conditions on the performance of solar-driven electrochemical reduction of carbon dioxide. *Physical Chemistry Chemical Physics*, 17(29):18924–18936, 2015.

[7] Ulf Riebesell, Victoria J Fabry, Lina Hansson, and Jean-Pierre Gattuso. *Guide to best practices for ocean acidification research and data reporting*. Office for Official Publications of the European Communities, 2011.

[8] Ezra L Clark, Joaquin Resasco, Alan Landers, John Lin, Linh-Thao Chung, Amber Walton, Christopher Hahn, Thomas F Jaramillo, and Alexis T Bell. Standards and

protocols for data acquisition and reporting for studies of the electrochemical reduction of carbon dioxide. *Acs Catalysis*, 8(7):6560–6570, 2018.

[9] Md Golam Kibria, Jonathan P Edwards, Christine M Gabardo, Cao-Thang Dinh, Ali Seifitokaldani, David Sinton, and Edward H Sargent. Electrochemical $CO_2$ reduction into chemical feedstocks: from mechanistic electrocatalysis models to system design. *Advanced Materials*, 31(31):1807166, 2019.

[10] Tim Möller, Wen Ju, Alexander Bagger, Xingli Wang, Fang Luo, Trung Ngo Thanh, Ana Sofia Varela, Jan Rossmeisl, and Peter Strasser. Efficient $CO_2$ to CO electrolysis on solid ni–n–c catalysts at industrial current densities. *Energy & Environmental Science*, 12(2):640–647, 2019.

[11] F Pelayo García de Arquer, Cao-Thang Dinh, Adnan Ozden, Joshua Wicks, Christopher McCallum, Ahmad R Kirmani, Dae-Hyun Nam, Christine Gabardo, Ali Seifitokaldani, Xue Wang, et al. $CO_2$ electrolysis to multicarbon products at activities greater than 1 a $cm^{-2}$. *Science*, 367(6478):661–666, 2020.

[12] Matthew Jouny, Wesley Luc, and Feng Jiao. General techno-economic analysis of $CO_2$ electrolysis systems. *Industrial & Engineering Chemistry Research*, 57(6):2165–2177, 2018.

[13] Zengcai Liu, Hongzhou Yang, Robert Kutz, and Richard I Masel. $CO_2$ electrolysis to CO and $O_2$ at high selectivity, stability and efficiency using sustainion membranes. *Journal of The Electrochemical Society*, 165(15):J3371, 2018.

[14] Phil De Luna, Christopher Hahn, Drew Higgins, Shaffiq A Jaffer, Thomas F Jaramillo, and Edward H Sargent. What would it take for renewably powered electrosynthesis to displace petrochemical processes? *Science*, 364(6438):eaav3506, 2019.

[15] Ifan EL Stephens, Karen Chan, Alexander Bagger, Shannon W Boettcher, Julien Bonin, Etienne Boutin, Aya Buckley, Raffaella Buonsanti, Etosha Cave, Xiaoxia Chang, et al.

2022 roadmap on low temperature electrochemical $CO_2$ reduction. *Journal of Physics: Energy*, 2022.

[16] Joshua M Spurgeon and Bijandra Kumar. A comparative technoeconomic analysis of pathways for commercial electrochemical $CO_2$ reduction to liquid products. *Energy & Environmental Science*, 11(6):1536–1551, 2018.

[17] Haeun Shin, Kentaro U Hansen, and Feng Jiao. Techno-economic assessment of low-temperature carbon dioxide electrolysis. *Nature Sustainability*, 4(10):911–919, 2021.

[18] M Neef and K Doll. CO adsorption on the Cu (111) surface: A density functional study. *Surface science*, 600(5):1085–1092, 2006.

[19] Stefan Vollmer, Gregor Witte, and Christof Wöll. Determination of site specific adsorption energies of CO on copper. *Catalysis letters*, 77(1):97–101, 2001.

[20] R Raval, SF Parker, ME Pemble, P Hollins, J Pritchard, and MA Chesters. Ft-rairs, eels and leed studies of the adsorption of carbon monoxide on Cu (111). *Surface Science*, 203(3):353–377, 1988.

[21] Yuvraj Y Birdja, Elena Pérez-Gallent, Marta C Figueiredo, Adrien J Göttle, Federico Calle-Vallejo, and Marc Koper. Advances and challenges in understanding the electrocatalytic conversion of carbon dioxide to fuels. *Nature Energy*, 4(9):732–745, 2019.

[22] Yoshio Hori, Katsuhei Kikuchi, and Shin Suzuki. Production of CO and $CH_4$ in electrochemical reduction of $CO_2$ at metal electrodes in aqueous hydrogencarbonate solution. *Chemistry Letters*, 14(11):1695–1698, 1985.

[23] Ruud Kortlever, Jing Shen, Klaas Jan P Schouten, Federico Calle-Vallejo, and Marc TM Koper. Catalysts and reaction pathways for the electrochemical reduction of carbon dioxide. *The journal of physical chemistry letters*, 6(20):4073–4082, 2015.

[24] Jeremy T Feaster, Chuan Shi, Etosha R Cave, Toru Hatsukade, David N Abram, Kendra P Kuhl, Christopher Hahn, Jens K Nørskov, and Thomas F Jaramillo. Understanding selectivity for the electrochemical reduction of carbon dioxide to formic acid and carbon monoxide on metal electrodes. *Acs Catalysis*, 7(7):4822–4827, 2017.

[25] Yoshio Hori, Ryutaro Takahashi, Yuzuru Yoshinami, and Akira Murata. Electrochemical reduction of CO at a copper electrode. *The Journal of Physical Chemistry B*, 101(36):7075–7081, 1997.

[26] JJ Kim, DP Summers, and KW Frese Jr. Reduction of $CO_2$ and CO to methane on Cu foil electrodes. *Journal of electroanalytical chemistry and interfacial electrochemistry*, 245(1-2):223–244, 1988.

[27] Qing Zhao and Emily A Carter. Revisiting competing paths in electrochemical $CO_2$ reduction on copper via embedded correlated wavefunction theory. *Journal of Chemical Theory and Computation*, 16(10):6528–6538, 2020.

[28] Xinyan Liu, Jianping Xiao, Hongjie Peng, Xin Hong, Karen Chan, and Jens K Nørskov. Understanding trends in electrochemical carbon dioxide reduction rates. *Nature communications*, 8(1):1–7, 2017.

[29] Tao Cheng, Hai Xiao, and William A Goddard III. Full atomistic reaction mechanism with kinetics for CO reduction on Cu (100) from ab initio molecular dynamics free-energy calculations at 298 k. *Proceedings of the National Academy of Sciences*, 114(8):1795–1800, 2017.

[30] Joseph H Montoya, Chuan Shi, Karen Chan, and Jens K Nørskov. Theoretical insights into a CO dimerization mechanism in $CO_2$ electroreduction. *The journal of physical chemistry letters*, 6(11):2032–2037, 2015.

[31] Younghye Kim, Sojung Park, Seung-Jae Shin, Woong Choi, Byoung Koun Min, Hyungjun Kim, Wooyul Kim, and Yun Jeong Hwang. Time-resolved observation of

C–C coupling intermediates on Cu electrodes for selective electrochemical $CO_2$ reduction. *Energy & Environmental Science*, 13(11):4301–4311, 2020.

[32] Wenchao Ma, Shunji Xie, Tongtong Liu, Qiyuan Fan, Jinyu Ye, Fanfei Sun, Zheng Jiang, Qinghong Zhang, Jun Cheng, and Ye Wang. Electrocatalytic reduction of $CO_2$ to ethylene and ethanol through hydrogen-assisted c–c coupling over fluorine-modified copper. *Nature Catalysis*, 3(6):478–487, 2020.

[33] Jason D Goodpaster, Alexis T Bell, and Martin Head-Gordon. Identification of possible pathways for C–C bond formation during electrochemical reduction of $CO_2$: new theoretical insights from an improved electrochemical model. *The journal of physical chemistry letters*, 7(8):1471–1477, 2016.

[34] Qing Zhao, John Mark P Martirez, and Emily A Carter. Charting C-C coupling pathways in electrochemical $CO_2$ reduction on Cu(111) using embedded correlated wavefunction theory. 2022.

[35] Rulle Reske, Hemma Mistry, Farzad Behafarid, Beatriz Roldan Cuenya, and Peter Strasser. Particle size effects in the catalytic electroreduction of $CO_2$ on Cu nanoparticles. *Journal of the American Chemical Society*, 136(19):6978–6986, 2014.

[36] Klaas Jan P Schouten, Elena Perez Gallent, and Marc TM Koper. Structure sensitivity of the electrochemical reduction of carbon monoxide on copper single crystals. *Acs Catalysis*, 3(6):1292–1295, 2013.

[37] Yuhang Wang, Ziyun Wang, Cao-Thang Dinh, Jun Li, Adnan Ozden, Md Golam Kibria, Ali Seifitokaldani, Chih-Shan Tan, Christine M Gabardo, Mingchuan Luo, et al. Catalyst synthesis under $CO_2$ electroreduction favours faceting and promotes renewable fuels electrosynthesis. *Nature Catalysis*, 3(2):98–106, 2020.

[38] Wesley Luc, Xianbiao Fu, Jianjian Shi, Jing-Jing Lv, Matthew Jouny, Byung Hee Ko, Yaobin Xu, Qing Tu, Xiaobing Hu, Jinsong Wu, et al. Two-dimensional copper

nanosheets for electrochemical reduction of carbon monoxide to acetate. *Nature Catalysis*, 2(5):423–430, 2019.

[39] Chungseok Choi, Soonho Kwon, Tao Cheng, Mingjie Xu, Peter Tieu, Changsoo Lee, Jin Cai, Hyuck Mo Lee, Xiaoqing Pan, Xiangfeng Duan, et al. Highly active and stable stepped Cu surface for enhanced electrochemical $CO_2$ reduction to $C_2H_4$. *Nature Catalysis*, 3(10):804–812, 2020.

[40] Tao Cheng, Hai Xiao, and William A Goddard. Nature of the active sites for CO reduction on copper nanoparticles; suggestions for optimizing performance. *Journal of the American Chemical Society*, 139(34):11642–11645, 2017.

[41] Ezra L Clark, Christopher Hahn, Thomas F Jaramillo, and Alexis T Bell. Electrochemical $CO_2$ reduction over compressively strained CuAg surface alloys with enhanced multi-carbon oxygenate selectivity. *Journal of the American Chemical Society*, 139(44):15848–15857, 2017.

[42] Chungseok Choi, Tao Cheng, Michelle Flores Espinosa, Huilong Fei, Xiangfeng Duan, William A Goddard III, and Yu Huang. A highly active star decahedron Cu nanocatalyst for hydrocarbon production at low overpotentials. *Advanced Materials*, 31(6):1805405, 2019.

[43] Rulle Reske, Matteo Duca, Mehtap Oezaslan, Klaas Jan P Schouten, Marc TM Koper, and Peter Strasser. Controlling catalytic selectivities during $CO_2$ electroreduction on thin Cu metal overlayers. *The Journal of Physical Chemistry Letters*, 4(15):2410–2413, 2013.

[44] Rosa M Arán-Ais, Fabian Scholten, Sebastian Kunze, Rubén Rizo, and Beatriz Roldan Cuenya. The role of in situ generated morphological motifs and Cu (i) species in $C_{2+}$ product selectivity during $CO_2$ pulsed electroreduction. *Nature Energy*, 5(4):317–325, 2020.

[45] Yansong Zhou, Fanglin Che, Min Liu, Chengqin Zou, Zhiqin Liang, Phil De Luna, Haifeng Yuan, Jun Li, Zhiqiang Wang, Haipeng Xie, et al. Dopant-induced electron localization drives $CO_2$ reduction to $C_2$ hydrocarbons. *Nature chemistry*, 10(9):974–980, 2018.

[46] Carlos G Morales-Guio, Etosha R Cave, Stephanie A Nitopi, Jeremy T Feaster, Lei Wang, Kendra P Kuhl, Ariel Jackson, Natalie C Johnson, David N Abram, Toru Hatsukade, et al. Improved $CO_2$ reduction activity towards $C_{2+}$ alcohols on a tandem gold on copper electrocatalyst. *Nature Catalysis*, 1(10):764–771, 2018.

[47] Sichao Ma, Masaaki Sadakiyo, Minako Heima, Raymond Luo, Richard T Haasch, Jake I Gold, Miho Yamauchi, and Paul JA Kenis. Electroreduction of carbon dioxide to hydrocarbons using bimetallic Cu–Pd catalysts with different mixing patterns. *Journal of the American Chemical Society*, 139(1):47–50, 2017.

[48] Y Hori, I Takahashi, O Koga, and N Hoshi. Electrochemical reduction of carbon dioxide at various series of copper single crystal electrodes. *Journal of Molecular Catalysis A: Chemical*, 199(1-2):39–47, 2003.

[49] Y Hori, H Wakebe, T Tsukamoto, and O Koga. Adsorption of CO accompanied with simultaneous charge transfer on copper single crystal electrodes related with electrochemical reduction of $CO_2$ to hydrocarbons. *Surface science*, 335:258–263, 1995.

[50] Federico Calle-Vallejo and Marc TM Koper. Theoretical considerations on the electroreduction of CO to $C_2$ species on Cu (100) electrodes. *Angewandte Chemie*, 125(28):7423–7426, 2013.

[51] Fabian Scholten, Khanh-Ly C Nguyen, Jared P Bruce, Markus Heyde, and Beatriz Roldan Cuenya. Identifying structure–selectivity correlations in the electrochemical reduction of $CO_2$: A comparison of well-ordered atomically clean and chemi-

cally etched copper single-crystal surfaces. *Angewandte Chemie International Edition*, 60(35):19169–19175, 2021.

[52] Oluwasegun J Wahab, Minkyung Kang, Enrico Daviddi, Marc Walker, and Patrick R Unwin. Screening surface structure–electrochemical activity relationships of copper electrodes under $CO_2$ electroreduction conditions. *ACS Catalysis*, 12:6578–6588, 2022.

[53] Bingxing Zhang, Jianling Zhang, Manli Hua, Qiang Wan, Zhuizhui Su, Xiuniang Tan, Lifei Liu, Fanyu Zhang, Gang Chen, Dongxing Tan, et al. Highly electrocatalytic ethylene production from $CO_2$ on nanodefective Cu nanosheets. *Journal of the American Chemical Society*, 142(31):13606–13613, 2020.

[54] Falong Jia, Xinxing Yu, and Lizhi Zhang. Enhanced selectivity for the electrochemical reduction of $CO_2$ to alcohols in aqueous solution with nanostructured Cu–Au alloy as catalyst. *Journal of Power Sources*, 252:85–89, 2014.

# CHAPTER 2

# Highly Selective Electrocatalytic Reduction of $CO_2$ into Methane on Nanotwinned Cu

## 2.1 Introduction

The electrochemical reduction of carbon dioxide ($CO_2$) offers a promising means for storing intermittent renewable energy in chemical fuels, promoting the usage of carbon-neutral energy in transportation and chemical sectors.[1–4] To date, copper (Cu) remains the most effective electrocatalyst for the $CO_2$ reduction reaction ($CO_2$RR) for producing hydrocarbons and oxygenates.[5] A variety of molecular products containing one to three C atoms ($C_1$ to $C_3$) have been reported on Cu-catalyzed $CO_2$RR,[5–7] which shows great economic potential for producing chemical fuels using $CO_2$.[8] Among these hydrocarbon products, methane ($CH_4$), the simplest of them, is of particular interest due to its good compatibility with existing natural gas infrastructure.[9] However, current Cu-based catalysts exhibit insufficient $CH_4$ selectivity, resulting in a high economic penalty in post-reaction separation, contributing to the current limited deployment of electrochemical $CO_2$RR.[10]

It has been widely reported that the $CO_2$RR pathways are highly dependent on the catalyst surface structure.[11] For example, a close-packed Cu(111) surface is more selective toward $CH_4$ compared to a more open Cu(100) surface.[12–14] In addition, defects such as steps, twin boundaries, and grain boundaries exposed on the surface have been found to influence $CO_2$RR selectivity.[15–17] Despite considerable efforts, the underlying mechanism of defect-modulated $CO_2$RR not yet well under-stood, which has hindered defect engineering of

Cu-based catalysts to achieve, e.g., high $CO_2$RR $CH_4$ selectivity. Herein, we report a highly-(111)-oriented Cu foil electrocatalyst with dense twin boundaries (tw-Cu) with an exceptional $CH_4$ selectivity of 86.1 ± 5.3% at –1.2 ± 0.02 V vs. the reversible hydrogen electrode (RHE). Quantum mechanical simulations show that the incorporation of twin boundaries on Cu(111) facets greatly reduces the reaction barrier of the rate-limiting CO hydrogenation step for $CH_4$ formation compared to the planar Cu(111) surface, explaining the high $CH_4$ selectivity in experiments.

## 2.2 Materials and Methods

### Chemicals

Ethanol ($C_2H_5OH$) (200 proof) and potassium bicarbonate ($KHCO_3$) were purchased from Sigma-Aldrich. An ultrapure purification system (Milli-Q advantage A10) produced the deionized water (DI) (18.2 MΩ cm) used to make the solutions. Pc-Cu was purchased from Sigma-Aldrich with 99.999% purity. The Nafion 115 membranes were purchased from the Fuel Cell Store. All reagents were used as received without further purification.

### Synthesis of Tw-Cu

In this study, we adopted rotary electroplating to fabricate tw-Cu foils. The electrolyte contains copper sulfate ($CuSO_4$), hydrochloric acid (HCl), sulfuric acid ($H_2SO_4$) and additives for nanotwin growth provided by Chemleaders, Inc. Figure 2.1 shows the schematic diagram for the rotary electroplating system, in which the inert anode is titanium (Ti) coated with iridium dioxide ($IrO_2$) and the cylinder cathode is made from Ti. During the electroplating process, the cathode rotation speed was 800 rpm controlled by a modulated speed rotator. The current density was 11 ASD ($A/dm^2$) and the thickness of tw-Cu foils was about 45 $\mu$m. Due to advantageously poor adhesion between the Ti and the tw-Cu foils, the electroplated

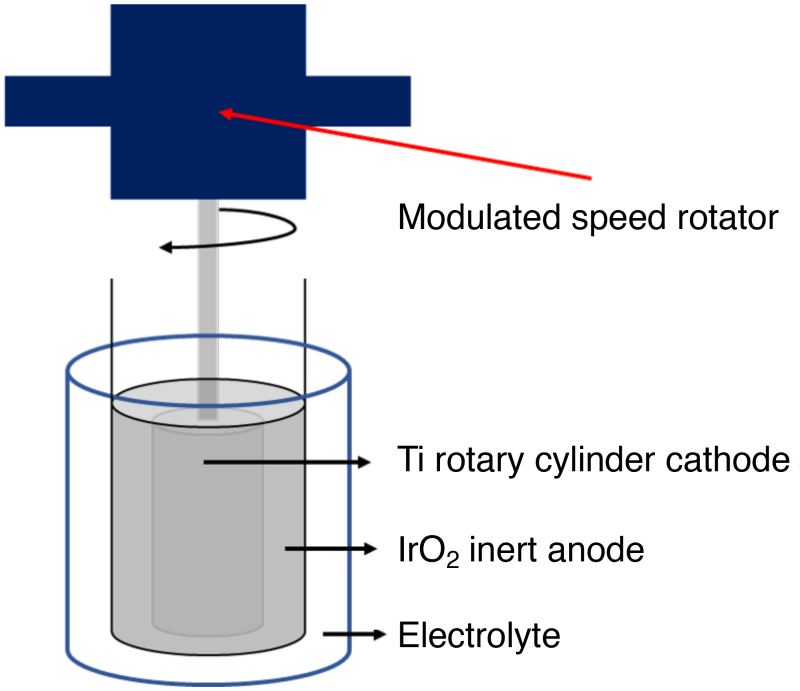


**Figure 2.1:** Schematic diagram for the synthesis of the tw-Cu rotary electroplating system. The anode was titanium (Ti) coated with iridium dioxide ($IrO_2$) and the cylinder cathode was made of Ti. During the electroplating process, the cathode rotation speed was 800 rpm controlled by a modulated speed rotator. Tw-Cu was electroplated under a current density of 11 A/dm$^2$ (ASD).

tw-Cu foils can be peeled off easily after deposition.

### Structure Characterization

Transmission electron microscopy (TEM) samples were prepared by a Nova 600 SEM/FIB system. TEM images of tw-Cu were taken using the FEI Titan scanning transmission electron microscope at an acceleration voltage of 300 kV. Atomic force microscopy (AFM) images were measured using a Bruker Dimension FastScan Scanning Probe Microscope (SPM) under ScanAsyst mode. Scanning electron microscopy (SEM) images were taken by a ZEISS Supra

40VP SEM. The crystal structure of the Cu foil was analyzed with a Panalytical X'Pert Pro X-ray Powder Diffractometer (XRD) using a Cu K$\alpha$ radiation source and conducting a symmetric scan. Electron backscatter diffraction (EBSD) was measured with a TESCAN GAIA-3 XMH integrated FIB-FESEM.

**Electrochemical Measurement**

All electrochemical experiments were conducted in a H-cell composed of two compartments and separated by a proton-exchange membrane. The cell was sonicated with 2% nitric acid and boiled with DI water three times before each test. The tw-Cu and pc-Cu foil was cut to 0.3 $cm^2$ and electrochemically polished in 85% phosphoric acid using samples as the anode and a Cu foil as the cathode under 2 V vs. Ag/AgCl for 200 s, then rinsed with DI water before each test. Cu foil was fixed by an electronic clip to form the working electrode. The counter electrode was a Pt wire from Pine Instruments. A Ag/AgCl (4M KCl) electrode purchased from Pine Instruments was used as the reference electrode. 0.1 M $KHCO_3$ electrolyte was prepared as electrolyte. A stir bar was introduced to the cathode chamber to mix the electrolyte thoroughly. A glass gas dispersion purging tube was inserted in the cathode chamber. $CO_2$ (Air gas, 99.99%) was purged at a rate of 11 sccm for 25 minutes before and during all electrocatalytic measurements. Electrochemical measurements were performed using a Princeton potentiostat (VersaSTAT 4). All current density was normalized by the geometric area. A constant voltage was applied for 20 to 30 minutes before the effluent was injected into a gas chromatograph (GC). Electrochemical data were recorded vs. the reference electrode and converted to the RHE scale after iR correction.

**Product Analysis**

Gas products were analyzed by a GC instrument (Shimadzu GC-2010-Plus) equipped with a Barrier Ionization Discharge (BID) detector and a Restek ShinCarbon ST Micropacked

column (2m 1mm ID). Helium ISP (Air-gas, 99.9999%) was applied as the carrier gas. The H-cell was connected to the GC with an outlet gas line. The effluent was injected through a six-port valve with a sampling loop of 1.5 ml effluent gas. The column oven was maintained at 30 °C for 8 minutes followed by a temperature ramp at 8 °C $min^{-1}$ to 250 °C, which was maintained for 5 min. The external standard method was used for quantitative calculations. A calibration curve was made analyzing a series of standard gas mixtures (Air Gas), with the concentration of the standard gas as the vertical axis and the respective peak area as the horizontal axis. After the calibration curve was created, the concentration of sample could be calculated from the calibration curve based on the peak area detected under the same condition. The FE was calculated from

$$FE_i = \frac{n_e \cdot F \cdot C_i \cdot r_G \cdot P_o}{R \cdot T_o \cdot I_{sat}} \times 100\% \tag{2.1}$$

where:

$n_e$ = number of electrons transferred;

$F$ = Faraday constant (96485 $Cmol^{-1}$);

$i$ = species, either $H_2$, CO, $CH_4$ or $C_2H_4$;

$C_i$ = concentration of the gas read from GC-BID;

$r_G$ = gas flow rate acquired from a ProFlow 6000 electronic flow meter (Restek) at the exit of the electrochemical cell (ml $min^{-1}$ at room temperature and ambient pressure);

$P_0$ = atmospheric pressure ($101325Pa$);

R = ideal gas constant ($8.314J \cdot mol^{-1} \cdot K^{-1}$);

$T_0$ = room temperature ($298.15K$);

$I_{sat}$ = current after saturation;

Liquid products were analyzed by Quantitative NMR spectroscopy (Bruker AV-300). Specifically, 0.1ml $D_2O$ was added to 0.9 ml of the cathode electrolyte, and 10 l of dimethyl sulfoxide (17.75 $\mu$M) was also mixed in as an internal standard. The one-dimensional 1H

spectrum was measured with a prewater saturation method.

### Computational Details

We performed spin-polarized periodic Kohn-Sham DFT calculations with the all-electron, frozen-core, projector augmented-wave (PAW)[18] method, Perdew-Burke-Ernzerhof (PBE) ex-change-correlation functional,[19] and Grimmes D3 dispersion correction[20,21] with Becke-Johnson damping[22] using the Vienna Ab initio Simulation Package (VASP)[23,24] version 5.4.4. We self-consistently simulated the valence 1s of H, 2s and 2p of C and O, and 4s and 3d of Cu. We employed a four-layer $4 \times 6$ supercell containing 96 Cu atoms along with at least 15 Å of vacuum to model the tw-Cu(111) surface (Figure 2.8a). We relaxed the atomic positions in the two topmost Cu layers and fixed the atoms in the two bottommost Cu layers at their bulk atomic positions. We applied dipole-field energy and potential corrections[25] along the z-direction to cancel the artificial electrostatic interaction between the slabs. We used a kinetic-energy cutoff of 660 eV for the planewave (PW) basis set, along with a -point-centered Monkhorst-Pack26 k-point mesh of $4 \times 4 \times 1$ to sample the Brillouin zone. We used Fermi surface smearing with a width of 0.09 eV within the Methfessel-Paxton scheme[26] for Brillouin zone integration to aid self-consistent-field convergence. We relaxed all atoms until the absolute total force on each atom was smaller than 0.03 eV/Å in geometry optimizations. We optimized the MEPs using the climbing image nudged elastic band (CI-NEB)[27] method.

## 2.3 Results and Discussion

### Surface Structure Study of Tw-Cu and Pc-Cu Catalyst

We first synthesized the tw-Cu catalysts using a previously reported approach,[28,29] through rotary electroplating in a copper sulfate ($CuSO_4$), hydrochloric acid (HCl), and sulfuric acid ($H_2SO_4$) mixed electrolyte with titanium (Ti) used as the cathode and Ti-coated with

iridium dioxide ($IrO_2$) as the anode (see Figure 2.1 for details). The resulting 45-$\mu$m-thick electro-plated tw-Cu foil was then peeled off for subsequent structural characterization and electrochemical $CO_2$RR studies.

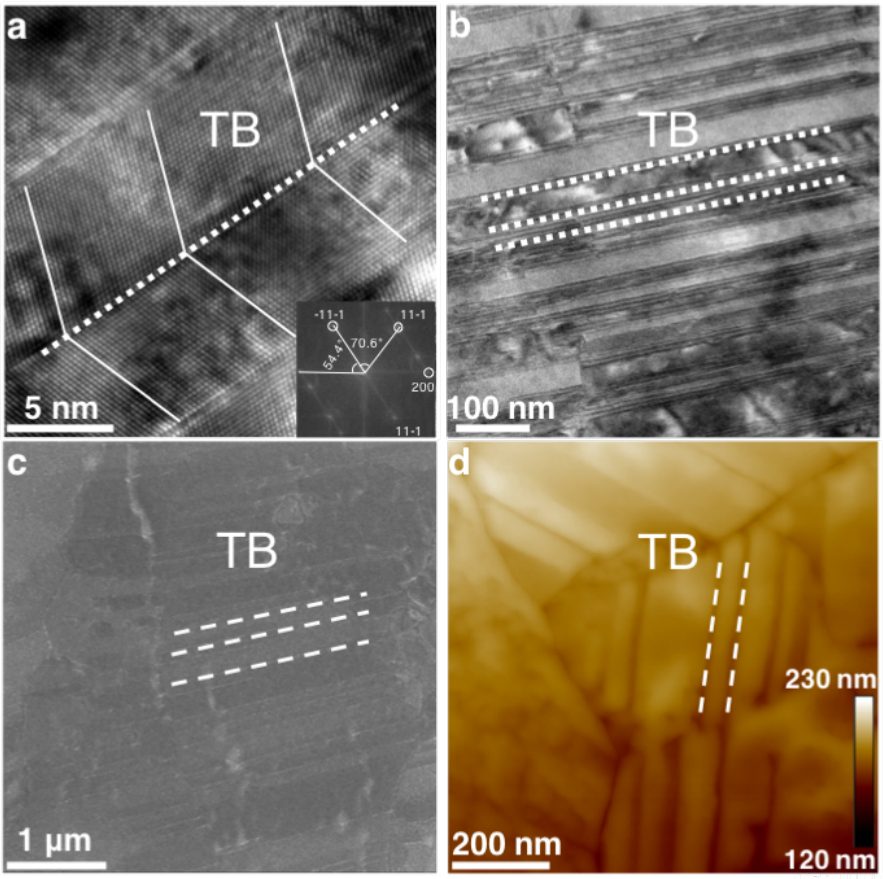


**Figure 2.2:** Structural characterization of tw-Cu and pc-Cu catalysts. (a) High-resolution TEM (HRTEM) image of the cross-section of tw-Cu with its twin-boundary (TB) assembly. Inset: FFT of the corresponding Cu TEM, which indicates the <110> axial direction and expression of the 111 planes. (b) Low-magnification TEM image of tw-Cu. The white dashed lines mark the typical TB. (c) SEM image of tw-Cu. The white dashed lines mark the TB. (d) AFM image of tw-Cu, which shows a surface roughness (Ra) of 2.7 nm.

The cross-section of tw-Cu was characterized by transmission electron microscopy (TEM), which shows well-defined twin boundary structures (Figure 2.2 a-b). The stacking sequence is

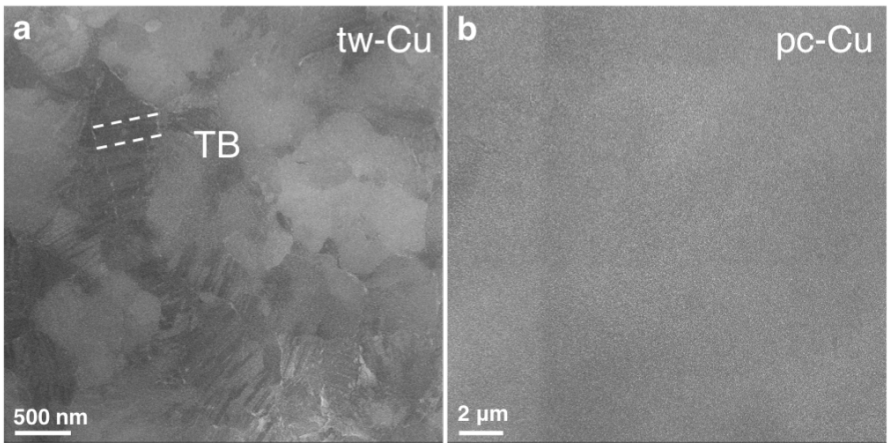


**Figure 2.3:** SEM image of (a) tw-Cu. The white dashed lines mark the twin-boundary (TB) assembly. (b) pc-Cu exhibits a relatively featureless surface.

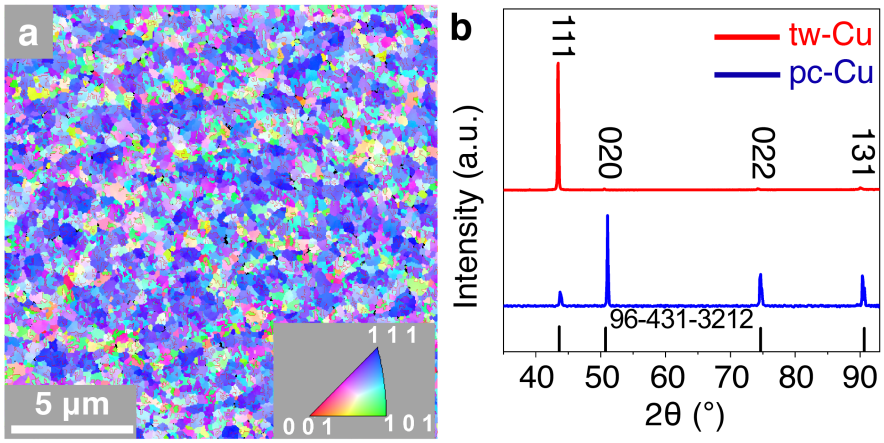


**Figure 2.4:** (a) Plane-view EBSD orientation maps showing the texture of the surface of tw-Cu. The inset indicates the crystallographic vectors used to color orientations in the maps, suggesting a strong (111) texture. (b) XRD of tw-Cu and pc-Cu, showing highly (111)-oriented tw-Cu compared to pc-Cu. The black line represents the reference sample with a PDF number of 96-431-3212.

inverted as ABC/A/CBA.[30] The structure of the tw-Cu was analyzed further by fast Fourier transform (FFT). The inset of Figure 2.2a shows the FFT with <110> axial direction and expression of the {111} planes. The tw-Cu is comprised of nanotwins with an average width

of 7 nm, quantified from Figure 2.2b. Scanning electron microscopy (SEM) and atomic force microscopy (AFM) further confirmed the rich twin boundaries on the surface (Figure 2.2c-d, Figure 2.3). The twin-boundary density of tw-Cu was determined to be 0.5 $\mu m/\mu m^2$ by electron backscatter diffraction (EBSD) (Figure 2.4a), which was much higher than (0.07 $\mu m/\mu m^2$) that of the commercial polycrystalline Cu foil (pc-Cu, 99.999% Cu foil, Sigma-Aldrich). The tw-Cu possessed a highly preferred (111)-oriented texture on the surface (Figure 2.4a), consistent with X-ray diffraction (XRD) spectra. (Figure 2.4b).

**Electrochemical $CO_2$RR Study**

The $CO_2$RR performance of tw-Cu and pc-Cu were measured in a gas-tight, H-shaped, two-compartment electrochemical cell (H-cell) separated by a proton-exchange membrane with $CO_2$-saturated 0.1 M $KHCO_3$ (pH = 6.8) at room temperature and at atmospheric pressure. Tw-Cu and pc-Cu first were polished electrochemically in 85% $H_3PO_4$ solution, and then were washed with deionized (DI) water and immediately transferred to the H-cell prior to every $CO_2$RR test. The $CO_2$RR performance was analyzed at potentials ranging from -0.98 to -1.3 V vs. RHE. The performances of tw-Cu and pc-Cu are summarized in Figure 2.5. The dominant $CO_2$RR products were gaseous $CH_4$, ethylene ($C_2H_4$), carbon monoxide (CO), and hydrogen ($H_2$). As the Faradaic efficiency (FE) of liquid products was less than 1%, we focused our analysis on gas-phase products. Notably, tw-Cu showed initial production of $CH_4$ from 0.99 V vs. RHE, which reached the highest FE of 86.1% at -1.2 V vs. RHE, doubling the observed FE of $CH_4$ on pc-Cu (43.4%) at the same potential (-1.2 V vs. RHE). Accordingly, tw-Cu showed larger absolute $CH_4$ partial current densities ($j_{CH_4}$) compared to pc-Cu. The $j_{CH_4}$ of tw-Cu reached -21.7 $mA/cm^2$ at -1.3 V vs. RHE, much larger magnitude than that of pc-Cu $j_{CH_4}$ (-16.3 $mA/cm^2$). Hereafter, comparisons between cathodic (partial) current densities, which by convention are negative, will refer to their magnitude only. The superior selectivity for $CH_4$ on tw-Cu was accompanied by suppression of $H_2$ and $C_2H_4$ generation. The $H_2$ selectivity observed on tw-Cu is 10% less than that on pc-Cu from

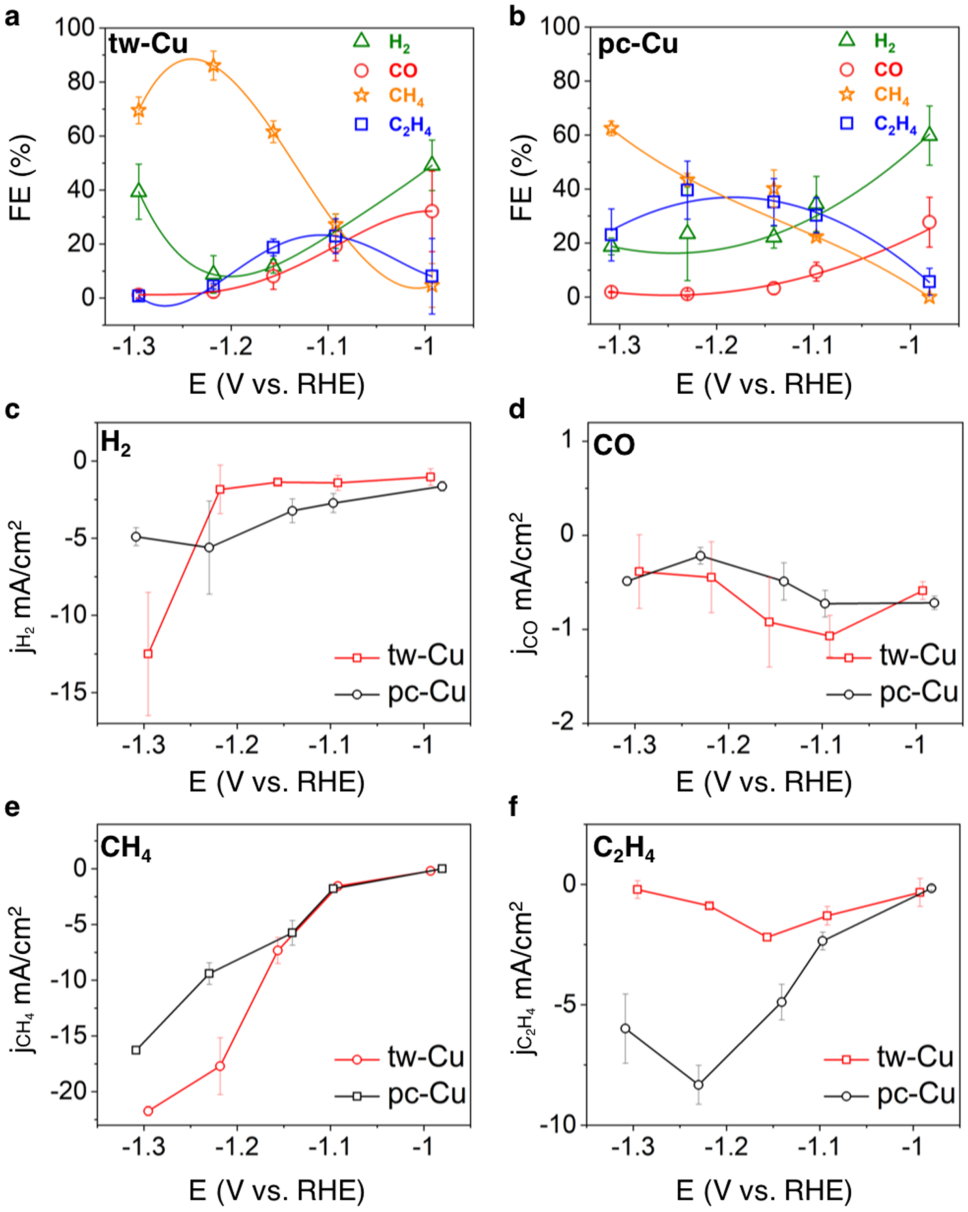


**Figure 2.5:** Electrochemical $CO_2$RR Performance. FEs of (a) tw-Cu and (b) pc-Cu. $H_2$, CO, $CH_4$, and $C_2H_4$ are denoted respectively as green, red, orange, and blue data points. Partial current densities of (c) $H_2$, (d) CO, (e) $CH_4$, and (f) $C_2H_4$. Red lines represent tw-Cu and black lines represent pc-Cu. Each error bar was calculated from three independent measurements. All potentials were iR-corrected.

**Table 2.1:** Comparison of $CO_2RR$ in peak $CH_4$ production for different Cu-based catalysts in H-cells.

| Catalyst | $FE_{CH_4}$ (%) | Applied potentials (V vs. RHE) | Electrolyte | Reference |
|---|---|---|---|---|
| **tw-Cu** | **86** | **-1.22** | **0.1 M $KHCO_3$** | **This work** |
| pc-Cu | 43 | -1.23 | 0.1 M $KHCO_3$ | |
| single crystal Cu (111) | 46 | -1.15 | 0.1 M $KHCO_3$ | [31] |
| single crystal Cu (110) | 50 | -1.15 | 0.1 M $KHCO_3$ | [32] |
| five-fold twinned Cu NWs loaded on carbon black | 55 | -1.25 | 0.1 M $KHCO_3$ | [33] |
| copper (II) phthalocyanine | 66 | -1.06 | 0.5 M $KHCO_3$ | [34] |
| nanotwinned copper | 62 | -1.6 | 0.2 M $KHCO_3$ | [35] |
| CuBi nanoalloys | 70.6 | -1.2 | 0.5 M $KHCO_3$ | [36] |
| CuNWs | 55% | -1.25 | 0.1M $KHCO_3$ | [33] |
| Single atom Cu on $CeO_2$ | 58% | -1.8 | 0.1M $KHCO_3$ | [37] |
| Cu electrode | 62% | -1.2 | 0.1M $KHCO_3$ | [38] |
| CRD-Cu3Pd | 40.6% | -1.2 | 0.1M $KHCO_3$ | [39] |
| $Cu/CeO_2$-x | 54% | -1.2 | 0.1M $KHCO_3$ | [40] |
| $Cu_2O$@CuHHTP | 73% | -1.4 | 0.1M $KHCO_3$ | [41] |
| $La_2CuO_4$ | 56.3% | -1.4 | 0.1M $KHCO_3$ | [42] |

-1 to -1.2 V vs. RHE. The partial current density of $H_2$ ($j_{H_2}$) on tw-Cu remained low at -1.8 mA/cm$^2$ at -1.2 V vs. RHE while the $j_{H_2}$ on pc-Cu significantly increased from -1.6 mA/cm$^2$ (-1.0 V vs. RHE) to -5.6 mA/cm$^2$ (-1.2 V vs. RHE), which suggests lower intrinsic activity of the hydrogen evolution reaction (HER) on tw-Cu. Meanwhile, tw-Cu exhibited lower $C_2H_4$ selectivity than pc-Cu in the potential range of -1.1 to -1.3 V vs. RHE. At -1.2 V vs. RHE, the FE of $C_2H_4$ reached 39.6% on pc-Cu, which is ten times higher than that of tw-Cu at the same potential. Similarly, the partial current density of $C_2H_4$ ($j_{C_2H_4}$) on pc-Cu reached -8.3 mA/cm$^2$ at -1.2 V vs. RHE, which is 9.22 times higher than on tw-Cu (-0.9 mA/cm$^2$). Taken together, tw-Cu showed a remarkably high $FE_{CH_4}$ in an H-cell not just when compared to pc-Cu, but also when compared to many state-of-the-art Cu-based catalysts reported in the literature, which includes five-fold twinned Cu nanowires (NWs),[33]

Copper(II) phthalocyanine,[34] and Cu-Bi nanoalloys[36] (Table 2.1).

To study further the competition between the HER and the $CO_2$RR on tw-Cu and pc-Cu, we performed linear sweep voltammetry (LSV) measurements in $N_2$-saturated (not $CO_2$RR, only HER) and $CO_2$-saturated electrolyte, respectively (Figure 2.6). For tw-Cu, the total current density (-36.2 mA/cm$^2$) increased in magnitude by 28.4 mA/cm$^2$ at 1.2 V vs. RHE in $CO_2$-saturated electrolyte compared with $N_2$-saturated electrolyte (Figure 2.6). On the other hand, the magnitude of the current density for pc-Cu increased by only 8.9 mA/cm$^2$ at the same potential (Figure 2.6). The larger cathodic current density enhancement on tw-Cu in $CO_2$-saturated electrolyte thus im-plies a higher $CO_2$RR efficiency. Under $N_2$-saturated conditions, however, pc-Cu exhibited a larger current density of -9.8 mA/cm$^2$ at -1.2 V vs. RHE compared to tw-Cu (-7.6 mA/cm$^2$), indicating a higher HER activity on pc-Cu.

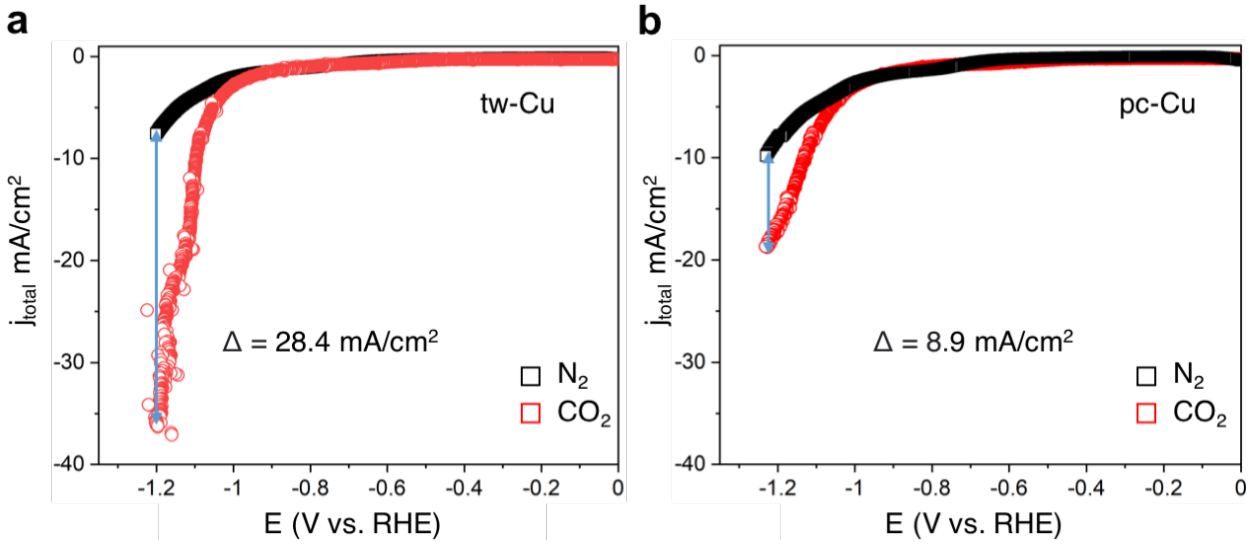


**Figure 2.6:** Linear sweep voltammetry curves obtained on (a) tw-Cu and (b) pc-Cu in $N_2$-saturated and $CO_2$-saturated electrolytes. For tw-Cu, there is a clear current density enhancement in the $CO_2$-saturated solution in comparison with the $N_2$-saturated solution. The current density difference at 1.2 V vs. RHE is 28.4 mA/cm$^2$. For pc-Cu, the current density difference at 1.2 V vs. RHE is about 8.9 mA/cm$^2$. The larger current density difference suggests a more efficient $CO_2$RR on tw-Cu.

**Quantum Mechanical Studies of Activity and Selectivity**

To gain further insights into the highly improved selectivity toward $CH_4$ production on tw-Cu, we first performed van-der-Waals-corrected periodic density functional theory calculations (DFT-PBE-D3, see Materials and Methods) to determine the reaction barriers of pertinent reactions in $CO_2$RR. Our previous high-level quantum simulations demonstrated that the rate-limiting step toward $CH_4$ on Cu(111) likely involves reduction of adsorbed CO (∗CO) roughly equally to hydroxymethylidyne (∗COH) and formyl (∗CHO) at -0.9 V vs. RHE.[43,44] In both hydrogenation reactions, a proton-coupled electron transfer (PCET) mechanism is preferred over surface hydride transfer.[43,44] Furthermore, two adsorbed hydrogenated CO species (∗COH and/or ∗CHO) are necessary reaction intermediates for C-C coupling toward multi-carbon products on the same facet, and ∗COH-CHO and ∗COH-∗COH are the most kinetically favorable coupling products.[45] We therefore calculated the activation barriers for these same $C_1$ and $C_{2+}$ pathways on a Cu(111) slab with twin boundary assemblies (tw-Cu(111)) (Figure 2.8a). The product structures and critical structures along the minimum energy pathways (MEPs) appear respectively in Figure 2.7 and 2.8a.

To simulate the rate-determining $C_1$ path (i.e., CO hydrogenation via PCET) on tw-Cu(111), we introduced an Eigen cation ($H_9O_4^+$) as a proton source to represent the explicit solvent. We predict at the DFT-PBE-D3 level that the reduction of ∗CO to form ∗CHO occurs with an activation (reaction) free energy of 0.55 (0.34) eV (Figure 2.8b). The competing ∗CO reduction to form ∗COH is a transition-state-free process with an activation and reaction free energy at the DFT-PBE-D3 level of 0.21 eV (Figure 2.8b). When compared with the DFT-PBE-D3 activation barriers of 0.85 eV for ∗CHO formation and 0.44 eV for ∗COH formation on planar Cu(111),[43] tw-Cu(111) exhibits lower activation barriers for both ∗CO reduction steps. Given that the first hydrogenation step is likely rate-determining in $CO_2$RR, this may explain the observed higher $CO_2$RR reaction rate and the enhanced $CH_4$ production on tw-Cu.

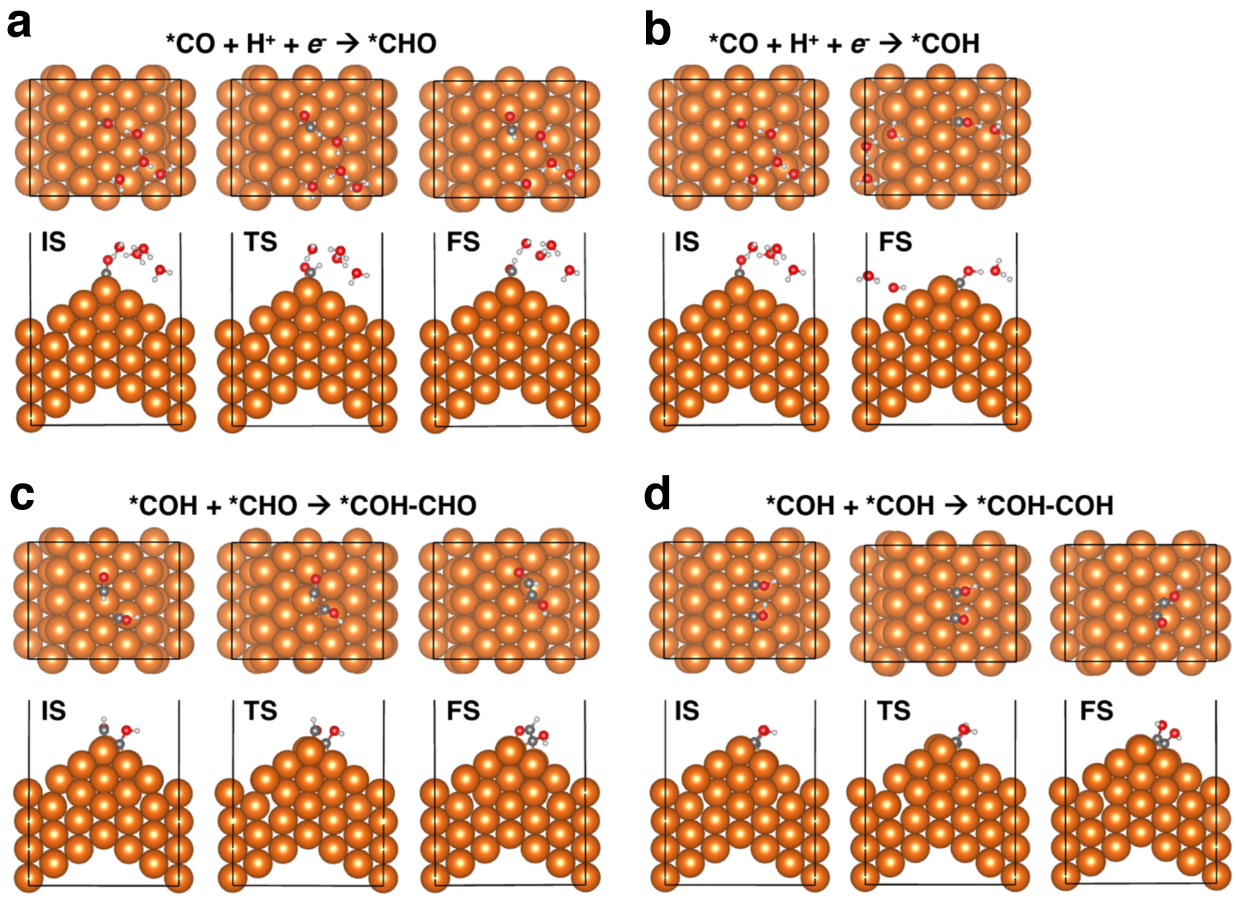


**Figure 2.7:** Critical (initial-state (IS), transition-state (TS), and final-state (FS)) structures (top and side views in upper and lower panels, respectively) along the minimum energy paths optimized within DFT-PBE-D3 for: CO reduction via PCET to form (a) ∗CHO and (b) ∗COH, and (c) ∗COH-CHO and (d) ∗COH-∗COH C-C coupling steps on tw-Cu(111). Atoms are colored as follows: Cu in orange, C in dark gray, O in red, and H in light gray.

We next calculated the barriers for C-C coupling to understand the selectivity toward $C_1$ ($CH_4$) vs. $C_2$ ($C_2H_4$) products on tw-Cu(111). C-C coupling routes are non-electroactive and thus no $H_9O_4^+$ was included in the simulations. The predicted barrier at the DFT-PBE-D3 level for forming ∗COH-CHO is 0.47 eV, which is higher than the 0.34 eV on planar Cu(111)[45] (Figure 2.8b). The DFT-PBE-D3 barrier for the other C-C coupling step forming ∗COH-∗COH decreases only slightly to 0.20 eV on tw-Cu(111) compared to 0.24 eV

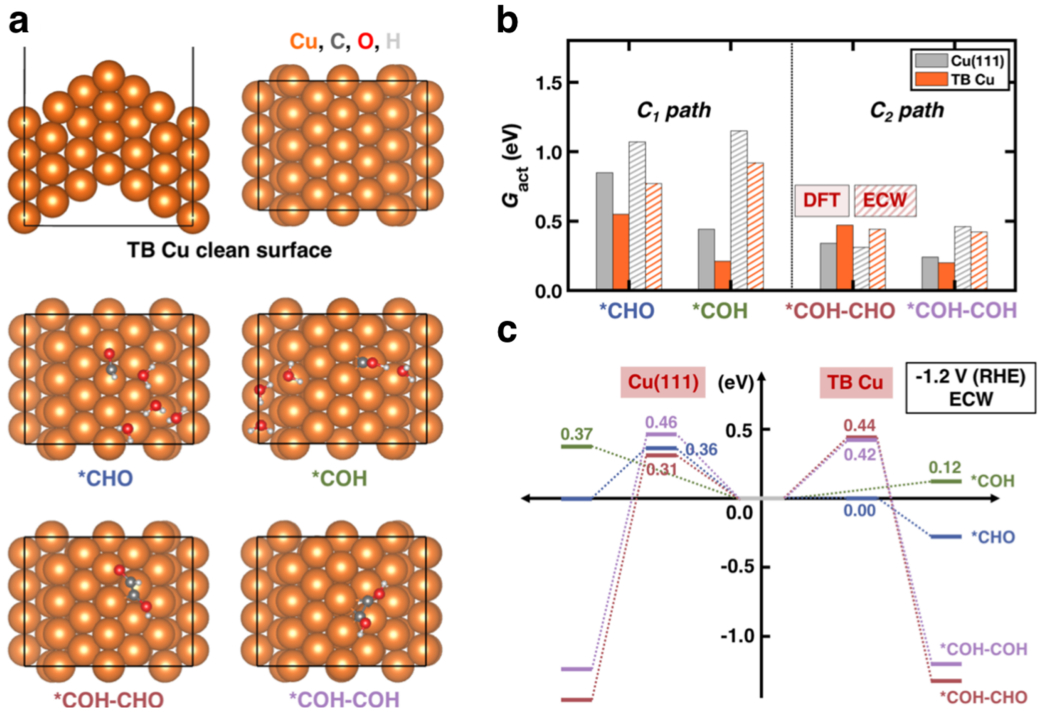


**Figure 2.8:** Quantum simulations of the rate-limiting steps of $C_1$ and $C_2$ pathways on tw-Cu(111). (a) (Top panels) Side (left) and top (right) views of the tw-Cu(111) surface periodic slab model and (middle and bottom panels) structures of products $*CHO+(H_2O)_4$, $*COH+(H_2O)_4$, *COH-CHO, and *COH-*COH (top views) as labeled. Cu in orange; C in dark gray; O in red; H in light gray. (b) Activation free energies $G_{act}$ for $C_1$ and $C_2$ pathways on tw-Cu(111) (orange bars) and planar Cu(111) (gray bars) predicted by DFT-PBE-D3 (DFT; solid bars) and emb-CASPT2 (ECW; hatched bars) at constant-charge conditions. Both DFT-PBE-D3-derived and emb-CASPT2-derived barriers on planar Cu(111) were taken from ref 43. The emb-CASPT2 results on tw-Cu(111) were estimated from energetic differences between emb-CASPT2 and DFT-PBE-D3 on planar Cu(111). (c) Energetics of the *COH (green), *CHO (blue), *COH-*COH (purple), and *COH-CHO (red) pathways on planar Cu(111) (left) and tw-Cu(111) (right) predicted by emb-CASPT2 (ECW) at an applied potential of -1.2 V vs. RHE.

**Table 2.2:** Constant-charge DFT-PBE-D3 and approximated emb-CASPT2 activation free energies ($G_{act}$) and reaction free energies ($\Delta G$) in eV for CO reduction via PCET to form ∗CHO and ∗COH and C-C coupling pathways to form ∗COH-CHO and ∗COH-∗COH on tw-Cu(111).

| | **DFT-PBE-D3** | | **emb-CASPT2** | |
|---|---|---|---|---|
| | $G_{act}$ (eV) | $\Delta G$ (eV) | $G_{act}$ (eV) | $\Delta G$ (eV) |
| **∗CHO** | 0.55 | 0.34 | 0.77 | 0.60 |
| **∗COH** | 0.21 | 0.21 | 0.92 | 0.92 |
| **∗COH-CHO** | 0.47 | -0.96 | 0.44 | -1.32 |
| **∗COH-COH** | 0.20 | -1.28 | 0.42 | -1.20 |

**Table 2.3:** Constant-charge DFT-PBE-D3 and emb-CASPT2 activation free energies ($G_{act}$) and reaction free energies ($\Delta G$) in eV for CO reduction to form ∗CHO and ∗COH and C-C coupling pathways to form ∗COH-CHO and ∗COH-∗COH on planar Cu(111), as well as free energy differences between two levels of theory. The energetics for CO reduction via PCET to form ∗CHO and ∗COH and for C-C coupling pathways to form ∗COH-CHO and ∗COH-∗COH on planar Cu(111) were taken respectively from Refs. 43 and 45.

| | **DFT-PBE-D3** | | **emb-CASPT2** | | | |
|---|---|---|---|---|---|---|
| | $G_{act}$ *(eV)* | $\Delta G$ (eV) | $G_{act}$ *(eV)* | $\Delta G$ (eV) | $\Delta G_{act}^{ECW-DFT}$ | $\Delta G^{ECW-DFT}$ |
| **∗CHO** | 0.85 | 0.53 | 1.07 | 0.79 | 0.22 | 0.26 |
| **∗COH** | 0.44 | 0.44 | 1.15 | 1.15 | 0.71 | 0.71 |
| **∗COH-CHO** | 0.34 | -1.10 | 0.31 | -1.46 | -0.03 | -0.36 |
| **∗COH-∗COH** | 0.24 | -1.32 | 0.46 | -1.24 | 0.22 | 0.08 |

on flat Cu(111)[45] (Figure 2.8b). Because tw-Cu(111) maintains similar or higher barriers for C-C coupling (a $C_2$ rate-limiting step), whereas above we show that hydrogenation of

**Table 2.4:** Adsorbate Bader charge changes between transition- and reactant-state structures ($\Delta q_{TS-R}$), and between product- and reactant-state structures ($\Delta q_{P-R}$) computed using embedded cluster models at the emb-PBE and emb-CASSCF level for CO reduction to form ∗CHO and ∗COH and C-C coupling pathways to form ∗COH-CHO and ∗COH-∗COH on planar Cu(111), as well as adsorbate Bader charge change differences between the two levels of theory. The structures and electron densities for CO reduction via PCET to form ∗CHO and ∗COH and for C-C coupling pathways to form ∗COH-CHO and ∗COH-∗COH on planar Cu(111) were taken respectively from Refs. 43 and 45.

| | **emb-PBE** | | **emb-CASSCF** | | | |
|---|---|---|---|---|---|---|
| | $\Delta q_{TS-R}$ | $\Delta q_{P-R}$ | $\Delta q_{TS-R}$ | $\Delta q_{P-R}$ | $\Delta\Delta q_{TS-R}^{ECW-DFT}$ | $\Delta\Delta q_{P-R}^{ECW-DFT}$ |
| **∗CHO** | 0.35 | -0.03 | 0.21 | -0.20 | -0.14 | -0.17 |
| **∗COH** | 0.31 | 0.31 | -0.05 | -0.05 | -0.36 | -0.36 |
| **∗COH-CHO** | 0.03 | 0.14 | 0.00 | 0.03 | -0.03 | -0.11 |
| **∗COH-COH** | 0.14 | 0.17 | 0.08 | -0.00 | -0.06 | -0.18 |

∗CO is promoted significantly by the twin boundaries, the $C_1$ path towards $CH_4$ may be disproportionately enhanced. However, because PCET is involved, rigorously analyzing the selectivity toward $CH_4$ vs. $C_2H_4$ requires a potential-dependent barrier analysis under working conditions (vide infra).

We showed previously that one needs to use embedded correlated wavefunction (ECW) theory[48–52] to predict accurately the activity and selectivity of $CO_2$RR on planar Cu(111)[43,44]. We therefore expect that the same level of theory is needed to describe correctly $CO_2$RR on tw-Cu(111). However, the high computational cost of, e.g., embedded complete active space second-order perturbation theory[53,54] (emb-CASPT2) impedes such investigations. We therefore used the energetic differences predicted between emb-CASPT2 and DFT-PBE-D3 on planar Cu(111) an ECW correction to approximate emb-CASPT2-predicted barriers on

**Table 2.5:** Adsorbate Bader charge changes between transition- and reactant-state ($\Delta q_{TS-R}$), and product- and reactant-state ($\Delta q_{P-R}$) structures computed using periodic slab models at the DFT-PBE-D3 level for CO reduction via PCET to form ∗CHO and ∗COH and C-C coupling pathways to form ∗COH-CHO and ∗COH-∗COH on planar Cu(111) and tw-Cu(111). Note that q on the two surfaces (planar and tw) agree to ∼0.10 e for the same type of reaction. The structures and electron densities for CO reduction via PCET to form ∗CHO and ∗COH and C-C coupling pathways to form ∗COH-CHO and ∗COH-∗COH on planar Cu(111) were taken respectively from Refs. 43 and 45.

| | **planar Cu(111)** | | **tw-Cu(111)** | |
|---|---|---|---|---|
| | $\Delta q_{TS-R}$ | $\Delta q_{P-R}$ | $\Delta q_{TS-R}$ | $\Delta q_{P-R}$ |
| **∗CHO** | 0.34 | -0.12 | 0.23 | -0.03 |
| **∗COH** | 0.31 | 0.31 | 0.28 | 0.28 |
| **∗COH-CHO** | 0.10 | 0.07 | 0.09 | 0.05 |
| **∗COH-∗COH** | 0.01 | 0.14 | 0.01 | 0.15 |

tw-Cu(111) (Table 2.2). In other words, we shifted the reaction and activation energies on tw-Cu(111) by the same ECW correction as their counterpart reaction on planar Cu(111). The nature of the difference in the predicted activation barriers between emb-CASPT2 and DFT-PBE-D3 in part originates from the difference in their descriptions of charge transfer during a reaction. We reached this conclusion by establishing a good linear correlation between (activation and reaction) free energy differences and charge change differences on adsorbates predicted at the two levels of theory on planar Cu(111) (Tables 2.3, 2.4, Figure 2.9). Because the same pathway on two different surfaces involves the same amount of charge transferred from the surface to the adsorbates and vice versa, we may directly use the corrections obtained from planar Cu(111) on tw-Cu(111) foregoing the need to perform expensive emb-CASPT2 calculations on tw-Cu(111) (Table 2.5). By applying this strategy, emb-CASPT2 would predict that the reduction of ∗CO to ∗CHO (∗COH) via PCET occurs

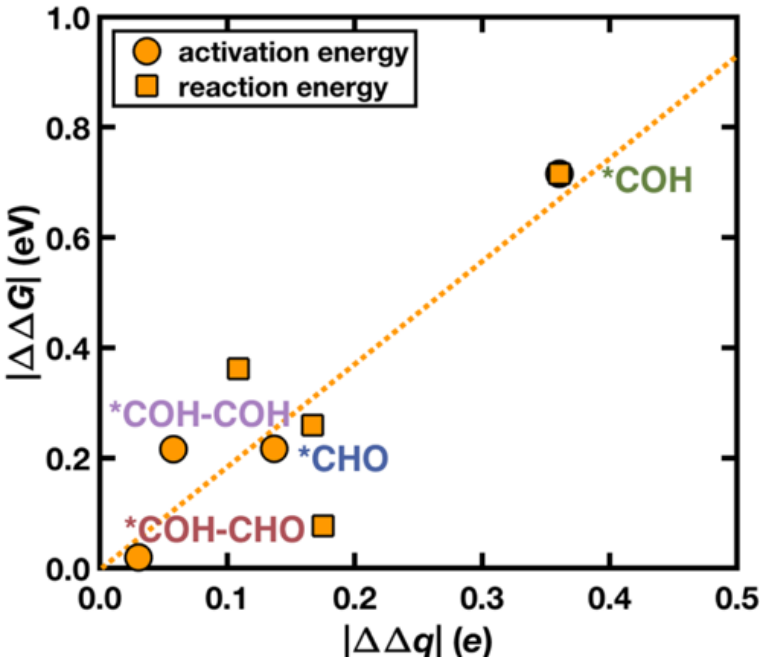


**Figure 2.9:** Plot of the absolute value of the predicted free energy difference of reaction (squares) and activation (circles) between emb-CASPT2 and DFT-PBE-D3 ($|\Delta\Delta G|$) vs. the absolute value of adsorbate electron charge change difference between emb-CASSCF and emb-DFT-PBE cluster models ($|\Delta\Delta q|$) for CO reduction to form ∗CHO and ∗COH via PCET and C-C coupling steps to form ∗COH-CHO and ∗COH-∗COH on planar Cu(111). We calculated the $|\Delta\Delta q|$ using Bader charge changes of adsorbates between transition (product) and reactant states. Only the results corresponding to the activation free energies (circles) are labelled.

with a barrier of 0.77 (0.92) eV on tw-Cu(111), lower than the barrier of 1.07 (1.15) eV on planar Cu(111)[43] (Figure 2.8b). In contrast, emb-CASPT2 would predict that the preferred C-C coupling route is the formation of ∗COH-∗COH on tw-Cu(111) with a barrier of 0.42 eV, higher than the activation barrier of 0.31 eV for the most preferred ∗COH-CHO pathway on planar Cu(111)[45] (Figure 2.8b). Therefore, using this beyond-DFT ECW theory that properly treats charge transfer, we again predict that use of tw-Cu(111) rather than planar Cu(111) reduces barriers for $C_1$ rate-limiting steps, while increasing barriers for C-C coupling

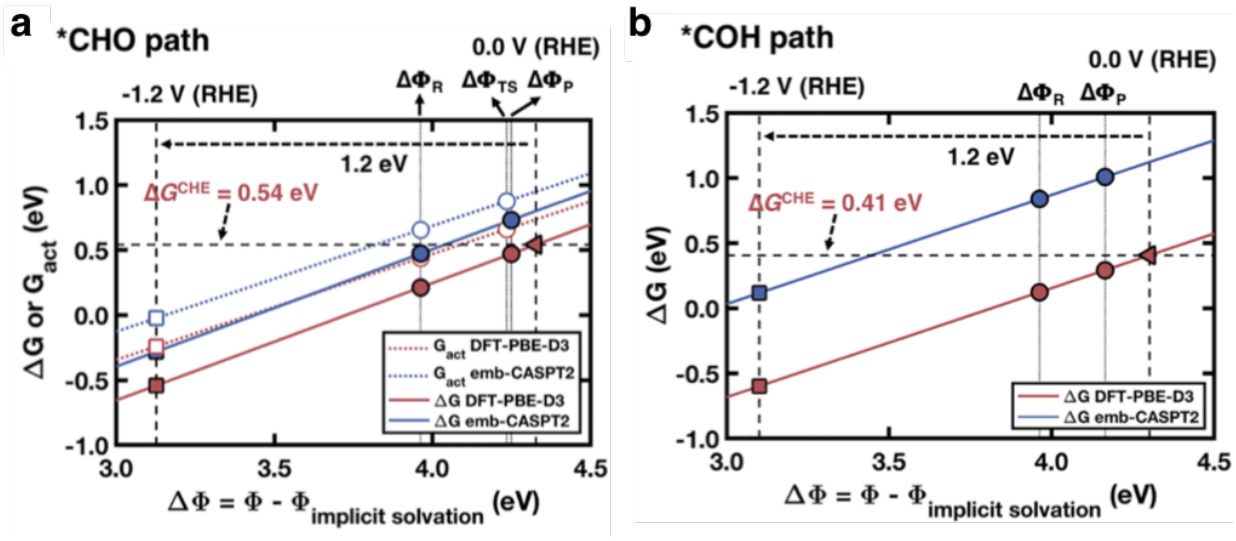


**Figure 2.10:** Potential dependence of the reaction ($\Delta$G) and activation ($G_{act}$) free energy for CO reduction to form (a) $*$CHO and (b) $*$COH via PCET on tw-Cu(111). Circles represent reaction (filled symbols) and activation (empty symbols) free energies extracted from the Chan-Nørskov capacitor model[46,47]. The horizontal black dashed lines indicate reaction free energies computed using a CHE model and DFT-PBE-D3 at an applied potential of 0.0 V vs. RHE. Triangles represent the intersections of these horizontal lines with their corresponding $\Delta\Phi_S$-dependent DFT-PBE-D3 reaction free energy lines. The vertical black dashed lines indicate $\Delta\Phi_S$ associated with applied potentials of 0.0 and -1.2 V vs. RHE as labelled. Squares represent data extrapolated to an applied potential of -1.2 V vs. RHE.

to form the most favored product ($*$COH-$*$COH on tw-Cu(111) vs. $*$COH-CHO on planar Cu(111)).

Finally, to fully rationalize selectivity toward $CH_4$ vs. $C_2H_4$ on tw-Cu(111), we contextualized the activation free energies presented above under real electrochemical conditions by transforming them from being a function of charge to a function of electrochemical potential (a thermodynamic Legendre transformation from constant charge to constant electrochemical potential), to determine potential-dependence of the barriers (Figure 2.10, Tables 2.6, 2.7).[43] We performed this analysis for electroactive CO PCET reduction steps. The emb-CASPT2

**Table 2.6:** Surface Bader charge (q, calculated from the tw-Cu(111) slab plus all of the adsorbates) and work function of the tw-Cu(111) slab with respect to the energy level of the bulk solvent in eV ($\Delta\Phi$), computed at the DFT-PBE-D3 level in the presence of implicit continuum solvation, and reaction ($\Delta G$) and activation ($G_{act}$) free energies at constant $\Delta\Phi$ in eV at the DFT-PBE-D3 and emb-CASPT2 levels of theory for CO reduction to form $*$CHO and $*$COH via PCET on tw-Cu(111).

| | | $q$ | $\Delta\Phi$ | **DFT** $G_{act}$ **or** $\Delta G$ | | **ECW** $G_{act}$ **or** $\Delta G$ | |
|---|---|---|---|---|---|---|---|
| | | | | $\Delta\Phi_R$ | $\Delta\Phi_P/\Delta\Phi_{TS}$ | $\Delta\Phi_R$ | $\Delta\Phi_P/\Delta\Phi_{TS}$ |
| $*$**CHO** | Reactant | -0.91 | 3.96 | - | - | - | - |
| | TS | -0.10 | 4.23 | 0.44 | 0.66 | 0.65 | 0.88 |
| | Product | -0.01 | 4.25 | 0.21 | 0.47 | 0.47 | 0.73 |
| $*$**COH** | Reactant | -0.91 | 3.96 | - | - | - | - |
| | TS | - | - | - | - | - | - |
| | Product | -0.07 | 4.16 | 0.12 | 0.29 | 0.84 | 1.01 |

activation barriers at an applied potential of -1.2 V vs. RHE (Figure 2.8c and Table 2.7) for $C_1$ rate-determining steps (0.00 eV for $*$CHO formation and 0.12 eV for $*$COH formation) are lower than that of the $C_2$ rate-determining steps (0.42 eV for $*$COH-$*$COH formation and 0.44 eV for $*$COH-CHO formation) on tw-Cu(111). These trends illustrate that tw-Cu(111) can enhance $CH_4$ production via substantially accelerated CO hydrogenation kinetics. By contrast, barriers for C-C coupling do not decrease on tw-Cu(111), effectively limiting $C_2H_4$ formation at this applied potential and explaining the high (low) FE for $CH_4$ ($C_2H_4$) observed in the experiment (Figure 2.5). Unlike tw-Cu(111), planar Cu(111) exhibits similar emb-CASPT2 barriers for $C_1$ (0.36 eV for $*$CHO formation and 0.37 eV for $*$COH formation) and $C_2$ (0.46 eV for $*$COH-$*$COH formation and 0.31 eV for $*$COH-CHO formation) rate-determining steps at the same applied potential (Figure 2.8c). This would explain the

**Table 2.7:** Activation ($G_{act}$) and reaction ($\Delta G$) free energies in eV for CO reduction to form ∗CHO and ∗COH via PCET at an applied potential of -1.2 V vs. RHE evaluated by emb-CASPT2 on tw-Cu(111) and planar Cu(111).The emb-CASPT2 energies, surface Bader charges, and work functions with respect to the energy level of the bulk solvent used to simulate potential-dependent activation and reaction free energies on planar Cu(111) were taken from Ref. 43. Unlike in Ref. 43, here, we report the energetics at more negative applied potentials of -1.2 V vs. RHE to compare the results between the planar Cu(111) and tw-Cu(111) directly with experiment (an applied potential of -0.9 V vs. RHE was used in the original work).

| | | **tw-Cu(111)** | | **planar Cu(111)** | |
|---|---|---|---|---|---|
| | | $G_{act}$ (eV) | $\Delta G$ (eV) | $G_{act}$ (eV) | $\Delta G$ (eV) |
| **U = -1.2 V vs. RHE** | ∗CHO | 0.00 | -0.28 | 0.36 | -0.02 |
| | ∗COH | 0.12 | 0.12 | 0.37 | 0.37 |

almost identical FEs, and thus a similar degree of preference for $CH_4$ and $C_2H_4$, observed at -1.2 V vs. RHE for pc-Cu (Figure 2.5).

## 2.4 Conclusion

To summarize, we report that a tw-Cu catalyst with a densely packed twin boundary on the surface exhibits a high $FE_{CH_4}$ (86.1 $\pm$ 5.3 %) in a H-cell. Coupled with structural and electrochemical surface characterizations of the tw-Cu catalyst, our computational analysis showed that the existence of twin boundaries in Cu(111) electrodes decreases the barriers for CO hydrogenation, while not doing so for C-C coupling, leading to a higher selectivity toward $CH_4$ over $C_2$ products. Our findings suggested an effective approach for tuning $CO_2$RR product selectivity by catalyst surface structure engineering.

## Bibliography


[1] Joseph H Montoya, Linsey C Seitz, Pongkarn Chakthranont, Aleksandra Vojvodic, Thomas F Jaramillo, and Jens K Nørskov. Materials for solar fuels and chemicals. *Nature materials*, 16(1):70–81, 2017.

[2] Daniel G Nocera. Personalized energy: The home as a solar power station and solar gas station. *ChemSusChem: Chemistry & Sustainability Energy & Materials*, 2(5):387–390, 2009.

[3] George A Olah, GK Surya Prakash, and Alain Goeppert. Anthropogenic chemical carbon cycle for a sustainable future. *Journal of the American Chemical Society*, 133(33):12881–12898, 2011.

[4] Li Li, Xiaodong Li, Yongfu Sun, and Yi Xie. Rational design of electrocatalytic carbon dioxide reduction for a zero-carbon network. *Chemical Society Reviews*, 2022.

[5] Yoshio Hori, Katsuhei Kikuchi, and Shin Suzuki. Production of CO and $CH_4$ in electrochemical reduction of $CO_2$ at metal electrodes in aqueous hydrogencarbonate solution. *Chemistry Letters*, 14(11):1695–1698, 1985.

[6] Stephanie Nitopi, Erlend Bertheussen, Soren B Scott, Xinyan Liu, Albert K Engstfeld, Sebastian Horch, Brian Seger, Ifan EL Stephens, Karen Chan, Christopher Hahn, et al. Progress and perspectives of electrochemical $CO_2$ reduction on copper in aqueous electrolyte. *Chemical reviews*, 119(12):7610–7672, 2019.

[7] Qi Lu and Feng Jiao. Electrochemical $CO_2$ reduction: Electrocatalyst, reaction mechanism, and process engineering. *Nano Energy*, 29:439–456, 2016.

[8] Md Golam Kibria, Jonathan P Edwards, Christine M Gabardo, Cao-Thang Dinh, Ali Seifitokaldani, David Sinton, and Edward H Sargent. Electrochemical $CO_2$ reduction

into chemical feedstocks: from mechanistic electrocatalysis models to system design. *Advanced Materials*, 31(31):1807166, 2019.

[9] Robert W Howarth, Anthony Ingraffea, and Terry Engelder. Should fracking stop? *Nature*, 477(7364):271–275, 2011.

[10] Matthew Jouny, Wesley Luc, and Feng Jiao. General techno-economic analysis of $CO_2$ electrolysis systems. *Industrial & Engineering Chemistry Research*, 57(6):2165–2177, 2018.

[11] Ruud Kortlever, Jing Shen, Klaas Jan P Schouten, Federico Calle-Vallejo, and Marc TM Koper. Catalysts and reaction pathways for the electrochemical reduction of carbon dioxide. *The journal of physical chemistry letters*, 6(20):4073–4082, 2015.

[12] Ichiro Takahashi, Osamu Koga, Nagahiro Hoshi, and Yoshio Hori. Electrochemical reduction of $CO_2$ at copper single crystal Cu (s)-[n (111)×(111)] and Cu (s)-[n (110)×(100)] electrodes. *Journal of Electroanalytical Chemistry*, 533(1-2):135–143, 2002.

[13] Yoshio Hori, Ichiro Takahashi, Osamu Koga, and Nagahiro Hoshi. Selective formation of $C_2$ compounds from electrochemical reduction of $CO_2$ at a series of copper single crystal electrodes. *The Journal of Physical Chemistry B*, 106(1):15–17, 2002.

[14] Klaas Jan P Schouten, Zisheng Qin, Elena Perez Gallent, and Marc TM Koper. Two pathways for the formation of ethylene in CO reduction on single-crystal copper electrodes. *Journal of the American Chemical Society*, 134(24):9864–9867, 2012.

[15] Ruperto G Mariano, Kim McKelvey, Henry S White, and Matthew W Kanan. Selective increase in $CO_2$ electroreduction activity at grain-boundary surface terminations. *Science*, 358(6367):1187–1192, 2017.

[16] Oluwasegun J Wahab, Minkyung Kang, Enrico Daviddi, Marc Walker, and Patrick R

Unwin. Screening surface structure–electrochemical activity relationships of copper electrodes under $CO_2$ electroreduction conditions. *ACS Catalysis*, 12:6578–6588, 2022.

[17] Chungseok Choi, Soonho Kwon, Tao Cheng, Mingjie Xu, Peter Tieu, Changsoo Lee, Jin Cai, Hyuck Mo Lee, Xiaoqing Pan, Xiangfeng Duan, et al. Highly active and stable stepped Cu surface for enhanced electrochemical $CO_2$ reduction to $C_2H_4$. *Nature Catalysis*, 3(10):804–812, 2020.

[18] Peter E Blöchl. Projector augmented-wave method. *Physical review B*, 50(24):17953, 1994.

[19] John P Perdew, Kieron Burke, and Matthias Ernzerhof. Generalized gradient approximation made simple. *Physical review letters*, 77(18):3865, 1996.

[20] Stefan Grimme, Jens Antony, Stephan Ehrlich, and Helge Krieg. A consistent and accurate ab initio parametrization of density functional dispersion correction (dft-d) for the 94 elements h-pu. *The Journal of chemical physics*, 132(15):154104, 2010.

[21] Stefan Grimme, Stephan Ehrlich, and Lars Goerigk. Effect of the damping function in dispersion corrected density functional theory. *Journal of computational chemistry*, 32(7):1456–1465, 2011.

[22] Axel D Becke and Erin R Johnson. A density-functional model of the dispersion interaction. *The Journal of chemical physics*, 123(15):154101, 2005.

[23] Georg Kresse and Jürgen Furthmüller. Efficient iterative schemes for ab initio total-energy calculations using a plane-wave basis set. *Physical review B*, 54(16):11169, 1996.

[24] Georg Kresse and Jürgen Furthmüller. Efficiency of ab-initio total energy calculations for metals and semiconductors using a plane-wave basis set. *Computational materials science*, 6(1):15–50, 1996.

[25] G Makov and MC Payne. Periodic boundary conditions in ab initio calculations. *Physical Review B*, 51(7):4014, 1995.

[26] MPAT Methfessel and AT Paxton. High-precision sampling for brillouin-zone integration in metals. *Physical Review B*, 40(6):3616, 1989.

[27] Graeme Henkelman, Blas P Uberuaga, and Hannes Jónsson. A climbing image nudged elastic band method for finding saddle points and minimum energy paths. *The Journal of chemical physics*, 113(22):9901–9904, 2000.

[28] Hsiang-Yao Hsiao, Chien-Min Liu, Han-wen Lin, Tao-Chi Liu, Chia-Ling Lu, Yi-Sa Huang, Chih Chen, and King-Ning Tu. Unidirectional growth of microbumps on (111)-oriented and nanotwinned copper. *Science*, 336(6084):1007–1010, 2012.

[29] Hsiang-Yuan Cheng, Dinh-Phuc Tran, KN Tu, and Chih Chen. Effect of deposition temperature on mechanical properties of nanotwinned Cu fabricated by rotary electroplating. *Materials Science and Engineering: A*, 811:141065, 2021.

[30] Zhang-Jie Wang, Qing-Jie Li, Yao Li, Long-Chao Huang, Lei Lu, Ming Dao, Ju Li, Evan Ma, Subra Suresh, and Zhi-Wei Shan. Sliding of coherent twin boundaries. *Nature communications*, 8(1):1–7, 2017.

[31] Y i Hori. Electrochemical $CO_2$ reduction on metal electrodes. *Modern aspects of electrochemistry*, pages 89–189, 2008.

[32] Y Hori, H Wakebe, T Tsukamoto, and O Koga. Adsorption of CO accompanied with simultaneous charge transfer on copper single crystal electrodes related with electrochemical reduction of $CO_2$ to hydrocarbons. *Surface science*, 335:258–263, 1995.

[33] Yifan Li, Fan Cui, Michael B Ross, Dohyung Kim, Yuchun Sun, and Peidong Yang. Structure-sensitive $CO_2$ electroreduction to hydrocarbons on ultrathin 5-fold twinned copper nanowires. *Nano letters*, 17(2):1312–1317, 2017.

[34] Zhe Weng, Yueshen Wu, Maoyu Wang, Jianbing Jiang, Ke Yang, Shengjuan Huo, Xiao-Feng Wang, Qing Ma, Gary W Brudvig, Victor S Batista, et al. Active sites of copper-complex catalytic materials for electrochemical carbon dioxide reduction. *Nature communications*, 9(1):1–9, 2018.

[35] Can Tang, Jianjian Shi, Xiaowan Bai, Anqi Hu, Ningning Xuan, Yawei Yue, Tong Ye, Bing Liu, Pengxiang Li, Peiyuan Zhuang, et al. $CO_2$ reduction on coppers twin boundary. *ACS Catalysis*, 10(3):2026–2032, 2020.

[36] Zhijiang Wang, Qi Yuan, Jingjing Shan, Zhaohua Jiang, Ping Xu, Yongfeng Hu, Jigang Zhou, Lina Wu, Zhuangzhuang Niu, Jianmin Sun, et al. Highly selective electrocatalytic reduction of $CO_2$ into methane on Cu–bi nanoalloys. *The Journal of Physical Chemistry Letters*, 11(17):7261–7266, 2020.

[37] Yifei Wang, Zheng Chen, Peng Han, Yonghua Du, Zhengxiang Gu, Xin Xu, and Gengfeng Zheng. Single-atomic Cu with multiple oxygen vacancies on ceria for electrocatalytic $CO_2$ reduction to $CH_4$. *ACS Catalysis*, 8(8):7113–7119, 2018.

[38] Dan Ren, Jinhuan Fong, and Boon Siang Yeo. The effects of currents and potentials on the selectivities of copper toward carbon dioxide electroreduction. *Nature communications*, 9(1):1–8, 2018.

[39] Wenjin Zhu, Lei Zhang, Piaoping Yang, Xiaoxia Chang, Hao Dong, Ang Li, Congling Hu, Zhiqi Huang, Zhi-Jian Zhao, and Jinlong Gong. Morphological and compositional design of Pd–Cu bimetallic nanocatalysts with controllable product selectivity toward $CO_2$ electroreduction. *Small*, 14(7):1703314, 2018.

[40] Seyedeh Behnaz Varandili, Jianfeng Huang, Emad Oveisi, Gian Luca De Gregorio, Mounir Mensi, Michal Strach, Jan Vavra, Chethana Gadiyar, Arghya Bhowmik, and Raffaella Buonsanti. Synthesis of Cu/ceo2-x nanocrystalline heterodimers with interfacial active sites to promote $CO_2$ electroreduction. *Acs Catalysis*, 9(6):5035–5046, 2019.

[41] Jun-Dong Yi, Ruikuan Xie, Zai-Lai Xie, Guo-Liang Chai, Tian-Fu Liu, Rui-Ping Chen, Yuan-Biao Huang, and Rong Cao. Highly selective $CO_2$ electroreduction to $CH_4$ by in situ generated Cu2o single-type sites on a conductive mof: Stabilizing key intermediates with hydrogen bonding. *Angewandte Chemie International Edition*, 59(52):23641–23648, 2020.

[42] Shenghua Chen, Yaqiong Su, Peilin Deng, Ruijuan Qi, Jiexin Zhu, Jinxi Chen, Zhitong Wang, Liang Zhou, Xingpeng Guo, and Bao Yu Xia. Highly selective carbon dioxide electroreduction on structure-evolved copper perovskite oxide toward methane production. *Acs Catalysis*, 10(8):4640–4646, 2020.

[43] Qing Zhao, John Mark P Martirez, and Emily A Carter. Revisiting understanding of electrochemical $CO_2$ reduction on Cu (111): competing proton-coupled electron transfer reaction mechanisms revealed by embedded correlated wavefunction theory. *Journal of the American Chemical Society*, 143(16):6152–6164, 2021.

[44] Qing Zhao and Emily A Carter. Revisiting competing paths in electrochemical $CO_2$ reduction on copper via embedded correlated wavefunction theory. *Journal of Chemical Theory and Computation*, 16(10):6528–6538, 2020.

[45] Qing Zhao, John Mark P Martirez, and Emily A Carter. Charting C–C coupling pathways in electrochemical $CO_2$ reduction on Cu (111) using embedded correlated wavefunction theory. *Proceedings of the National Academy of Sciences*, 119(44):e2202931119, 2022.

[46] Karen Chan and Jens K Nørskov. Electrochemical barriers made simple. *The journal of physical chemistry letters*, 6(14):2663–2668, 2015.

[47] Karen Chan and Jens K Nørskov. Potential dependence of electrochemical barriers from ab initio calculations. *The journal of physical chemistry letters*, 7(9):1686–1690, 2016.

[48] Patrick Huang and Emily A Carter. Advances in correlated electronic structure methods for solids, surfaces, and nanostructures. *Annu. Rev. Phys. Chem.*, 59:261–290, 2008.

[49] Chen Huang, Michele Pavone, and Emily A Carter. Quantum mechanical embedding theory based on a unique embedding potential. *The Journal of chemical physics*, 134(15):154110, 2011.

[50] Florian Libisch, Chen Huang, and Emily A Carter. Embedded correlated wavefunction schemes: Theory and applications. *Accounts of chemical research*, 47(9):2768–2775, 2014.

[51] Kuang Yu, Florian Libisch, and Emily A Carter. Implementation of density functional embedding theory within the projector-augmented-wave method and applications to semiconductor defect states. *The Journal of Chemical Physics*, 143(10):102806, 2015.

[52] Kuang Yu, Caroline M Krauter, Johannes M Dieterich, and Emily A Carter. *Density and potential functional embedding: Theory and practice*. John Wiley & Sons Hoboken, NJ, 2017.

[53] Kerstin Andersson, Per Aake Malmqvist, Bjoern O Roos, Andrzej J Sadlej, and Krzysztof Wolinski. Second-order perturbation theory with a casscf reference function. *Journal of Physical Chemistry*, 94(14):5483–5488, 1990.

[54] Paolo Celani and Hans-Joachim Werner. Multireference perturbation theory for large restricted and selected active space reference wave functions. *The Journal of Chemical Physics*, 112(13):5546–5557, 2000.

# CHAPTER 3

# Intimate Atomic Cu-Ag Interfaces for High $CO_2$RR Selectivity towards Methane at Low Over Potential

## 3.1 Introduction

Humanity is at the brink of fossil fuel exhaustion and faces challenges of global climate change. Carbon dioxide ($CO_2$) emission is a primary driver of global warming and the reducing pH levels of the ocean. Meanwhile fossil fuels are not renewable and will eventually deplete. Creating a closed-loop process to recycle $CO_2$ to value-added fuels is a promising option to mitigate global warming and grant inexhaustible energy sources.[1–4] Developing efficient electrochemical catalysts for $CO_2$ reduction reaction ($CO_2$RR) is a prerequisite for establishing a carbon recycle loop and renewable energy technologies.

In the past decade, electrochemical $CO_2$RR has remarked prominent achievements in both scientific apprehension and technological developments. Among many electrocatalysts, copper (Cu) is the only known electrochemical catalyst to convert $CO_2$ to alternative energy fuels and hydrocarbons (especially methane ($CH_4$)) with sufficient current density and selectivity.[5] However, a mixture of primary products, competition with hydrogen evolution reaction (HER), and required high overpotential for $CO_2$RR on monometallic Cu still pose challenges. Therefore, designing Cu-based catalysts with high selectivity at low overpotentials is of great interest.[6] The prior art of research has improved Cu catalyst's modulation of structure defects,[7–10] shapes,[11–13] size,[14] and chemical states[15–20] of Cu. For example, grain boundaries (GBs) exhibited $\sim$ 2.5 times higher $CO_2$RR activity with less competitive

reaction (HER).[21] Cheng et al. reported that Cu's surface steps, having a combination of one strong and one weak CO binding sites, enhancing $C_2$ productions with reducing the rate determining step ($*$OCCOH formation energy) to 0.52 eV.[22] Alloying Cu with a second metal is another attractive way to design catalysts.[23] However, Cu usually lost its extraordinary $CO_2$RR capability of producing hydrocarbon and oxygenates, having $C_2$ and $C_3$ carbons by forming an alloy with other elements.[24–27] Thus, interface Cu with neighboring unmixable second elements has been proposed to design Cu-based catalysts to retain the Cu's unique $CO_2$RR capability.[27,28] Because of this complexity, the research in CuM (M denote another metal element) alloy catalysts for electrochemical $CO_2$RR has not been sufficiently explored or compared with pure Cu. Silver (Ag) is a promising candidate to achieve such an unmixable Cu-M interface design because Ag and Cu are known for their thermodynamical immiscibility over all compositions at room temperature.[29–34] For example, Huang et al. reported that the interface between Cu catalysts and Ag catalysts was the crucial active site to enhance $CO_2$RR over pure Cu catalysts.[34] However, the interface between Cu and Ag has been limited due to the limited boundary obtained between Cu and Ag catalysts. Maximizing the Cu and Ag interface at the atomic level is highly desired but challenging.

Herein, we report a two-step approach to build the interface between Cu and Ag at the atomic level (Figure 3.1). Cu nanowires (CuNWs) were first synthesized and followed by galvanic replacement from Cu to Ag to achieve in situ formation of CuAg ensembles to obtain CuNWs with rich atomic Cu-Ag interfaces. The attractive Cu-Ag interface showed a dramatic change in $CO_2$RR selectivity from $C_2H_4$ to $CH_4$, which remarked a 63.3 $\pm$ 4.9% $FE_{CH_4}$ at -1.1 $\pm$ 0.01 V (RHE) (reversible hydrogen electrode, referenced to all potentials) and an impressive maximum $FE_{CH_4}$ of 72% at low potential of -1.2 V.

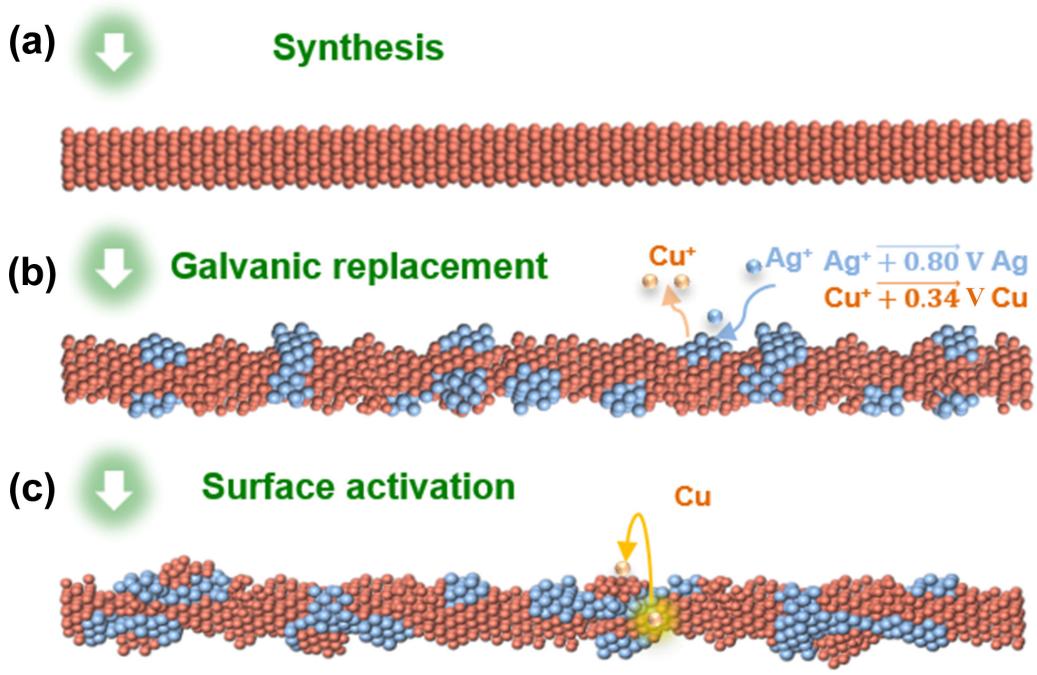


**Figure 3.1:** Schematic of preparing CuAgNWs. (a) The pure CuNWs is synthesized, (b) Galvanic replacement is conducted to partially replace Cu surface to Ag surface, (c) Atomic interface between Cu and Ag is further generated through in situ formation of CuAg ensembles during the electrochemical $CO_2$RR.

## 3.2 Materials and Methods

### Chemicals

Copper(II) chloride dihydrate ($CuCl_2 \cdot 2H_2O$, 99.999%), Silver acetate(99.99%), Imidazole (99%), D-(+)-Glucose (> 99.5%), Hexadecylamine (HDA) (> 98%), Ethanol (200 proof), were all purchased from Sigma-Aldrich. Ultra-pure purification system (Aqua Solutions) purified the deionized (DI) water (18.2 MΩ/cm) in aqueous solutions.

### Preparation of CuAg Nanowires (CuAgNWs) Catalyst

To synthesize CuAgNWs catalyst, we use a two-steps process. First, 22 mg $CuCl_2 \cdot 2H_2O$, 50 mg D-(+)-Glucose, 180 mg HDA were mixed in 10 ml DI water containing in 30 ml vial. The mixtures were sonication for 15 min. The mixture was transferred to an oil bath and was heated to 100 °C with stirring for 8 hr. The synthesized CuNWs was naturally cooled down to room temperature for 12 hr. Second, 9.72 mg Ag acetate and 6.7 mg imidazole were mixed in 8 ml DI water, 1 ml the mixture was added in the CuNWs solutions, and kept at 50 °C without stirring for 25 min or 60 min. The synthesized CuAgNWs were thoroughly washed with hexane/ethanol solvents and were collected by centrifuge at 9500 rpm.

### Materials Characterizations

After the synthesized NWs were washed, the NWs dispersed in hexane were dropped and dried onto carbon-coated copper TEM grids (Ted Pella, Redding, CA) under room temperature for TEM analysis. To get transmission electron microscopy (TEM) images, a FEI CM120 transmission electron microscope was operated at 120 kV. A 300 kV FEI Titan transmission electron microscope was conducted for high-resolution TEM images (HRTEM). JEM-ARM300F Grand ARM TEM with 300 kV was used for high resolution dark field images and Energy-dispersive X-ray spectroscopy (EDX). We measured the size of CuNWs by the longest width within the NWs. Powder X-ray diffraction (PXRD) patterns were taken from a Panalytical X'Pert Pro X-ray Powder Diffractometer with Cu-K radiation. The concentration of catalysts was analyzed by inductively coupled plasma atomic emission spectroscopy (TJA RADIAL IRIS 1000 ICP-AES).

### Electrochemical Measurements

To measure current densities, a three-electrode cell was used. We used a glassy-carbon rotating disk electrode (RDE) working electrode (diameter: 5 mm, area: 0.196 $cm^2$) purchased

from Pine Instruments. The current densities were measured by CV scanning at a rate of 50 mV/s in $CO_2$-saturated 0.1 M $KHCO_3$ electrolyte. To calculate Faradaic efficiency (FE), we used a gas-tight electrolysis H-cell (WizMac) separated with a cation exchange membrane (Sigma Aldrich). Consumed charges were collected to calculate from Princeton Applied Research VersaSTAT 4 workstation. Working, reference, and counter electrodes were 1 cm diameter glassy-carbon electrode, Ag/AgCl (4 M KCl) electrode, and Pt wire, respectively. $CO_2$ (Air gas, 99.99%) was bubbled to 0.1 M $KHCO_3$ electrolyte solution for 30 minutes and kept purging into the cathodic compartment at 15 sccm. All discussed potentials were converted to those against RHE after iR correction.

**Product Analysis**

Gas products were analyzed by gas chromatography equipped with a barrier ionization discharge detector (GC-BID) (Shimadzu Tracera GC-BID 2010 Plus) and a Restek Micropacked GC column. GC-BID was calibrated by five standard gases. Helium (Air gas, 99.9999%) was the carrier gas. An outlet gas line of gas-tight H-cell was directly routed to a p-type Hastelloy 6 port with a sampling loop (1.5 ml). 1.5 ml effluence gas was analyzed at every 45 ± 1 min. The FE was calculated as below:[35]

$$FE_j = \frac{nFv_jGp_o}{RTi_total} \times 100\% \tag{3.1}$$

where:

n = the number of electrons for a given product.

$v_j$(vol.%) = The volume concentration of gas products (CO, $H_2$, $CH_4$, and $C_2H_4$) in the effluence gas from the electrochemical cell (GC data).

G (ml/min at room temperature and ambient pressure) = Gas flow rate measured by a ProFlow 6000 electronic flow meter (Restek) at the exit of the electrochemical cell.

$i_{total}$(mA) = steady-state cell current.

$p_0 = 1.01 \times 10^5\ Pa$, $T = 298.15\ K$, $F = 96485\ C \cdot mol^{-1}$, $R = 8.314\ J \cdot mol^{-1} \cdot K^{-1}$.

Quantitative NMR (Bruker AV-600) was conducted to analyze the liquid product. Specifically, 0.3 mL of $D_2O$ was added to 0.65 mL of the reacted electrolyte, and 50 $\mu L$ of dimethyl sulfoxide (0.512 $\mu M/mL$) was mixed as an internal standard. The 1D 1H spectrum was measured with a pre-water saturation method.

## 3.3 Results and Discussion

We synthesized bimetallic CuAg nanowires (CuAgNWs) through a synthesis of CuNWs followed by galvanic replacement of Cu to Ag (Figure 3.1a, 3.1b). To be specific, 22 mg of $CuCl_2 \cdot 2H_2O$, 50 mg of glucose, and 180 mg of hexadecylamine (HDA) were mixed in 10 mL of deionized (DI) water (18.2 M/Ω) under sonication for 15 min, then heated at 100 °C for 8 hr in an oil bath. After the reaction solution cooled down to room temperature, 1.21 mg of $AgCH_3CO_2$ and 0.84 mg of imidazole were added to the CuNW solution, which was kept at 50 °C for 25 min or 60 min without stirring for galvanic replacements from Cu to Ag.

The relatively high standard reduction potential of Ag ($Ag++e^- \rightarrow Ag(s)$, 0.80 $E^o$ (V) (standard hydrogen electrode) compared to Cu ($Cu^{2+}+2e^- \rightarrow Cu(s)$, 0.34 $E^o$ (V) (standard hydrogen electrode))[36] drives replacements from Cu to Ag on the surface of CuNWs. The synthesized CuAgNWs were washed five times with hexane/ethanol mixture and were collected by centrifuge. The CuAgNWs were characterized by transmission electron microscopy (TEM), Cs-corrected high-angle annular dark-field imaging scanning transmission electron microscope (HAADF STEM), Energy-dispersive X-ray spectroscopy (EDX), and powder X-ray diffraction (PXRD). The average size of CuNWs (25 nm ± 7.7 nm) was obtained by averaging more than 100 NWs in width (Figure 3.2). Imidazole, a small molecular capping agent, was found pivotal in slowing down the fast Ag galvanic replacement reaction on the surface of CuNWs and keeping one dimensional structure of CuAgNWs without disintegrat-

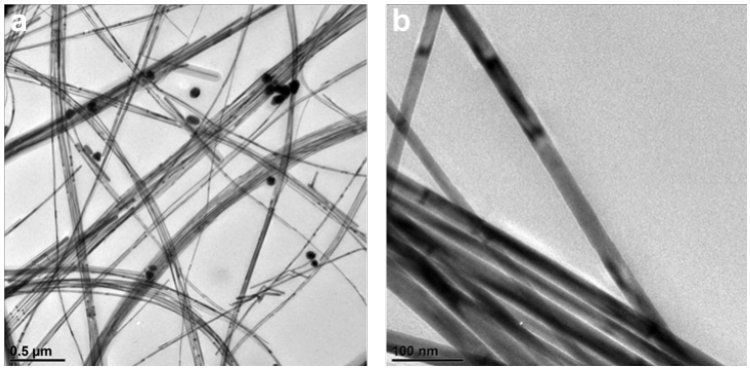


**Figure 3.2:** TEM characterizations of the CuNWs. (a, b) Low magnification TEM image of CuNWs. The d=25 ± 7.7 nm width was determined by averaging more than 100 NWs.

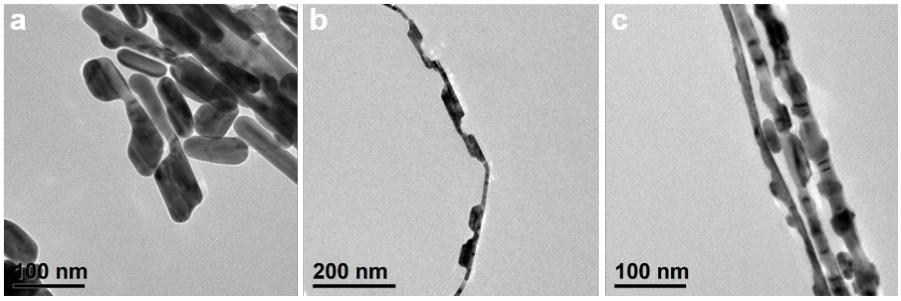


**Figure 3.3:** The galvanic replacement with different amounts of imidazole. (a) without imidazole, (b) with 0.8 mg imidazole, (c) with 2.5 mg imidazole.

ing into CuAg nanoparticles (NPs) (Figure 3.3). The pure CuNWs showed flat and clean surfaces, whereas the uneven surface was observed after the Ag galvanic replacement on the surface of CuNWs (Figure 3.4).

The PXRD peaks of CuAgNWs indicate no Bragg angle shift of Cu {111} and Ag {111} after the galvanic replacement of Ag for 25 min (Figure 3.5), which indicates an unmixable pure Cu and Ag phase system without forming the CuAg alloy. High intensity of Ag {111} plane in CuAgNWs with the galvanic replacement for 60 min illustrates more replacements from Cu to Ag element for longer galvanic reaction times.

To quantify the bulk and surface composition of CuAgNWs, we carried out inductively

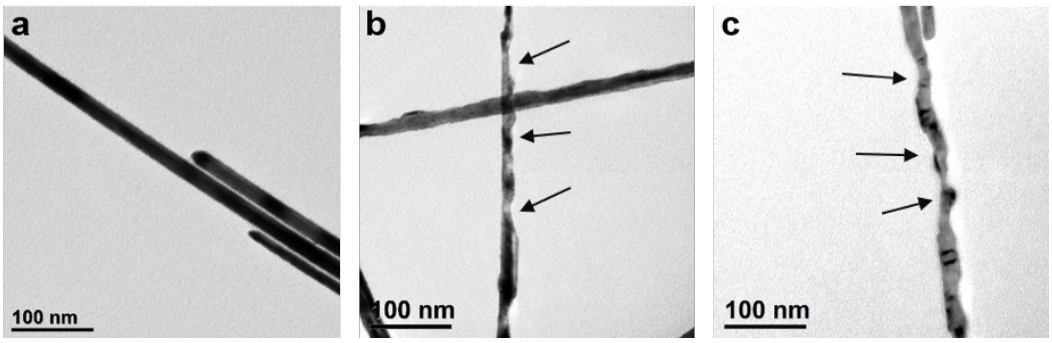


**Figure 3.4:** The galvanic replacement with 2.5 mg imidazole at different times. (a) no galvanic replacement, (b) galvanic replacement for 25 min, c) galvanic replacement for 60 min.

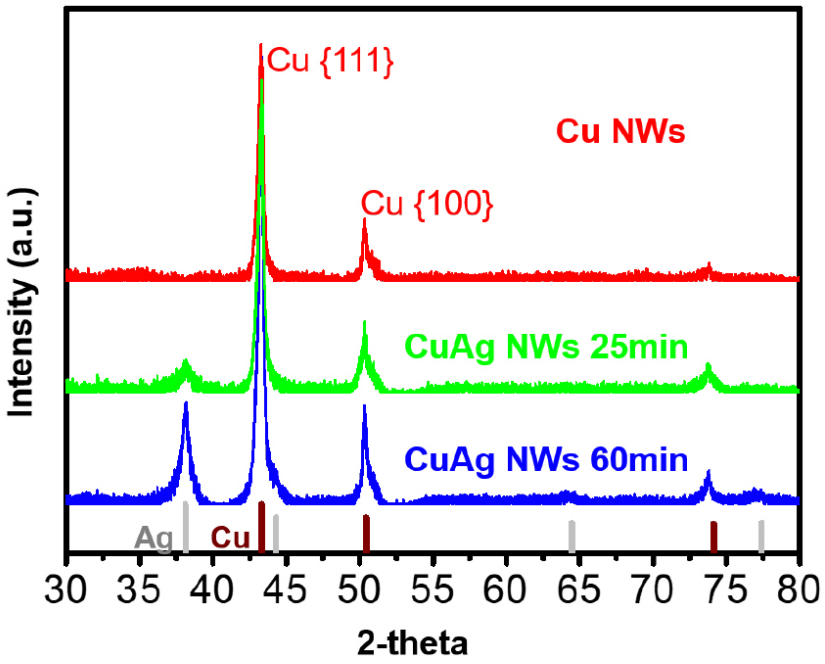


**Figure 3.5:** PXRD of CuNWs and bimetallic CuAgNWs after the galvanic replacement for 25 min and 60 min (red represent pure CuNWs, green represent CuAgNWs after 25 min galvanic replacement, and blue represent CuAgNWs after 60 min galvanic replacement.

**Table 3.1:** The atomic composition of CuAgNWs by ICP and XPS.

| Min. | Notation | ICP measurement | | XPS measurement | |
|---|---|---|---|---|---|
| | | Cu (at%) | Ag (at%) | Cu (at%) | Ag (at%) |
| **0 min** | Cu | 100 | 0 | 100 | 0 |
| **25 min** | Cu9Ag1 | 90.39 | 9.611 | 89.08 | 10.93 |
| **60 min** | Cu8.2Ag1.8 | 82.11 | 17.89 | 68.13 | 31.87 |

coupled plasma atomic emission spectroscopy (ICP-AES) and X-ray photoelectron spectroscopy (XPS). Table 3.1 shows a summary of ICP and XPS composition analyses. The bulk composition from ICP analysis showed 82% of Cu and 18% of Ag (Cu8.2Ag1.8NWs) in CuAgNWs with the galvanic replacement for 60 min; and 90% of Cu and 10% of Ag (Cu9Ag1NWs) with the galvanic replacement for 25 min. In the case of XPS, the calculated electron inelastic mean free path of Cu at 992.3 eV and Ag 365 eV are 1.67 nm and 0.727 nm, respectively,[37] which reveals a surface limited component analysis of XPS for Cu and Ag metal. XPS analysis of Cu8.2Ag1.8NWs (60 min) illustrates two times higher Ag concentration than the Ag component from ICP analysis, indicating thicker Ag concentration on the surface of Cu8.2Ag1.8NWs. In contrast, in CuAgNWs from 25 min galvanic replacements show comparable Ag concentration at bulk and surface of Cu9Ag1NWs, indicating that the galvanic replacement only occurred at the CuNW surface and Ag mainly stays near the surface.

Indeed Cs-corrected HAADF STEM images of CuNWs and EDX maps of the Cu9Ag1NWs confirmed that galvanic replacement of Cu to Ag on the surface (Figure 3.6). The EDX maps showed Ag mainly located on the surface of CuNWs, and formed separate Ag phase from Cu phases in Cu9Ag1NWs (Figure 3.6c-d). Cu K and Ag L EDX maps illustrate that a thin layer of Ag covers the surface of CuNWs (Figure 3.6e, Figure3.6h). In contrast, with longer (60 min) galvanic replacement, the Cu8.2Ag1.8NWs showed more uneven surfaces and much

thicker surface coverage of Ag compared to Cu9Ag1NWs (25 min galvanic reaction). (Figure 3.7).

We further found that electrochemical treatment of the as-prepared Cu9Ag1NWs can drive Cu to the surface of Cu9A1NWs and generate atomic Cu-Ag interfaces with more exposed Cu surface. The Cu9Ag1NW catalysts inks were prepared by mixing 4 mg of the CuAgNWs in 1 ml ethanol and 10 $\mu l$ of 5% Nafion. We dropped 10 $\mu l$ catalyst inks on the 1 cm diameter glassy carbon electrode. Subsequently, by using a high reduction bias (V = -1.05 V), we activated the CuAgNWs in $CO_2$-saturated 0.1 M $KHCO_3$ solution for 2 hr. After such treatment, Figure 3.8 showed the generated atomic Cu-Ag interfaces on the surface of Cu9Ag1NWs. EDX maps showed that Cu rose above the top of Ag-covered surface of as-prepared Cu9Ag1 NWs (Figure 3.8a, Figure 3.8d and Figure 3.9). The interfaces between Cu ensembles and Ag layers are quite prominent in Cs-corrected HAADF STEM of Cu component in Figure 3.8b,e and Ag component in Figure 3.8c, Figure 3.8f.

The migration of Cu atoms outward to the surface of the NWs can be understood in the differential binding strengths of Cu and Ag to $CO_2$RR intermediates or products. Back et al.[38] reported that Cu(211) has -0.77 eV of CO binding energy ($E_B$[CO]), -0.16 eV of H binding energy ($E_B$[H]), and -0.07 eV of OH binding ($E_B$[OH]), which are all stronger than Ag(211) (-0.15 eV of $E_B$[CO], 0.30 eV of $E_B$[H], and 0.56 eV of OH binding $E_B$[OH]). Zhong et al.[39] also reported that the Cu has stronger $E_B$[H] and $E_B$[CO] than Ag. The Cu under Ag surface could go to the top surface because of Cu's stronger binding energies with hydrogen, carbon monoxide, and hydroxide compared with Ag. To confirm the molecules' types for the generation of the unique Cu-Ag surface ensembles structures, we carried out the activation process changing purging gas of $CO_2$, CO, and $H_2$ at -1.05 V vs. RHE for 30 min, respectively.Figure 3.10 illustrates that the Cu component went to the top surface at all purging conditions. Interestingly, in the Cu8.2Ag1.8NWs, the Cu and Ag elements separated into Cu particles and Ag straw structures (Figure 3.11). This indicates a thick enough Ag surface layer might limit the movement of Cu towards the surface to rise above

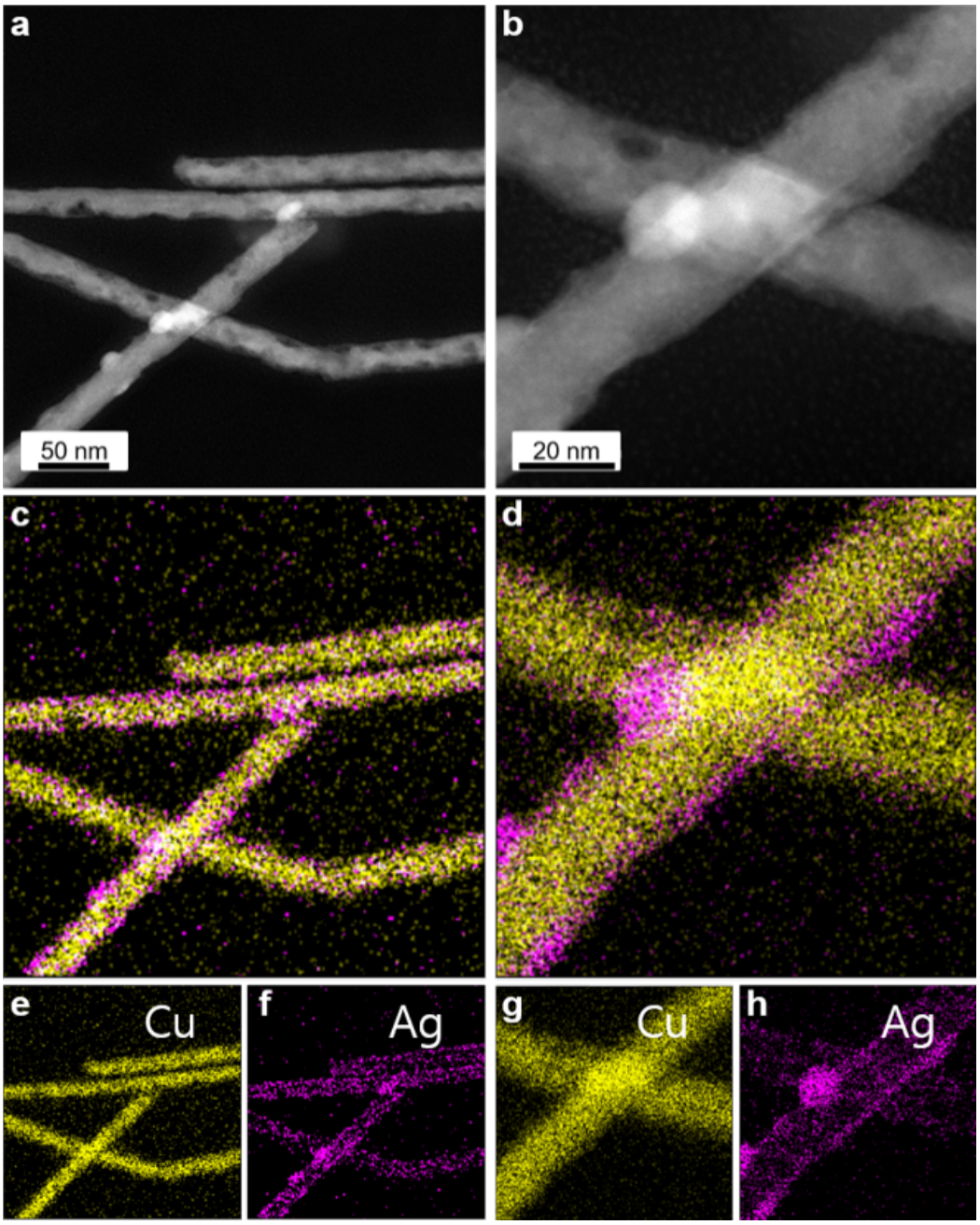


**Figure 3.6:** STEM and EDX mapping of Cu9Ag1NWs. (a,b) STEM images of Cu9Ag1NWs, (c-h) EDX of Cu9Ag1NWs. Yellow is Cu and purple is Ag.

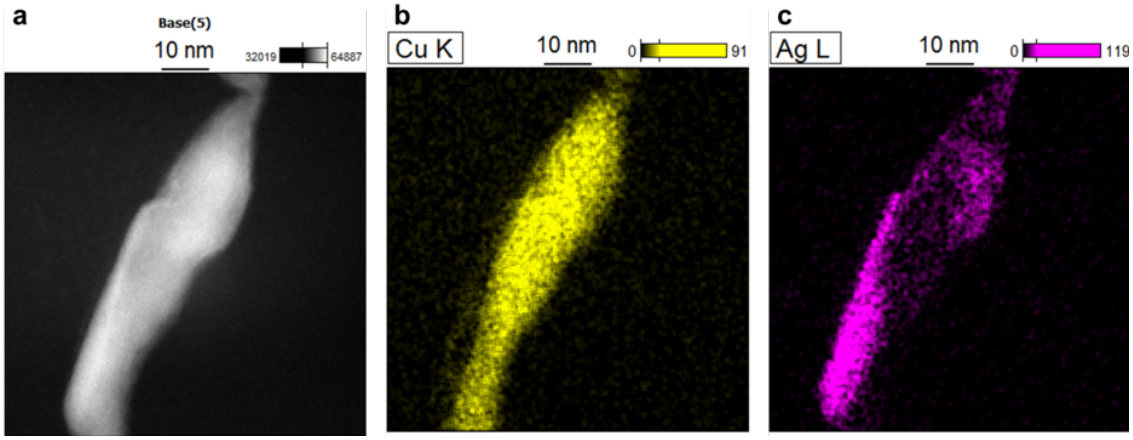


**Figure 3.7:** STEM and EDX mapping of Cu8.2Ag1.8 NWs. (a) STEM images of Cu8.1Ag1.8NWs, (b,c) EDX of Cu8.2Ag1.8NWs. Yellow is Cu and purple is Ag.

the Ag surface.

We conducted $CO_2$RR with $CO_2$-saturated 0.1 M $KHCO_3$ (pH 6.8) in a gas-tight H-cell at room temperature under atmospheric pressure. We analyzed effluent gas/liquid products at different applied potentials between -1.02 and -1.25 V vs. RHE. To compare the $CO_2$RR performance of pure Ag, we also synthesized AgNPs (Figure 3.12).

It is found that with increasing Ag content in the CuAgNWs, the electrochemically active surface area (ECSA) normalized current densities decreased (Figure 3.13). Because liquid products from $CO_2$RR of these catalysts were less than 10%, we focused the discussion of Faradaic efficiency (FE) on gas-phase products (Table **??**,Table 3.3). Figure 3.14 shows FEs of CuNWs (Figure 3.14a), Cu9Ag1NWs (Figure 3.14b), Cu8.2Ag1.8NWs (Figure 3.14c), and AgNPs (Figure 3.14d). The pure CuNWs exhibited high selectivity of 60.37 $\pm$ 4.46% of $FE_{C_2H_4}$ at -1.06 V (RHE), and 55.01 $\pm$ 7.58% of $FE_{CH_4}$ at -1.23 V vs. RHE (Figure 3.14a). However, Cu9Ag1NWs showed very different product selectivity. Cu9Ag1NWs suppress $C_2H_4$ productions to less than $\sim$ 21% at all measured potentials (Figure 3.14b). At the same time, the $CH_4$ production from Cu9Ag1NWs started to rise at $\sim$ -1.12 V vs. RHE with $FE_{CH_4}$ 63.29 $\pm$ 4.85%, which continued to rise to an impressive maximum $FE_{CH_4}$ 72% at low potential of

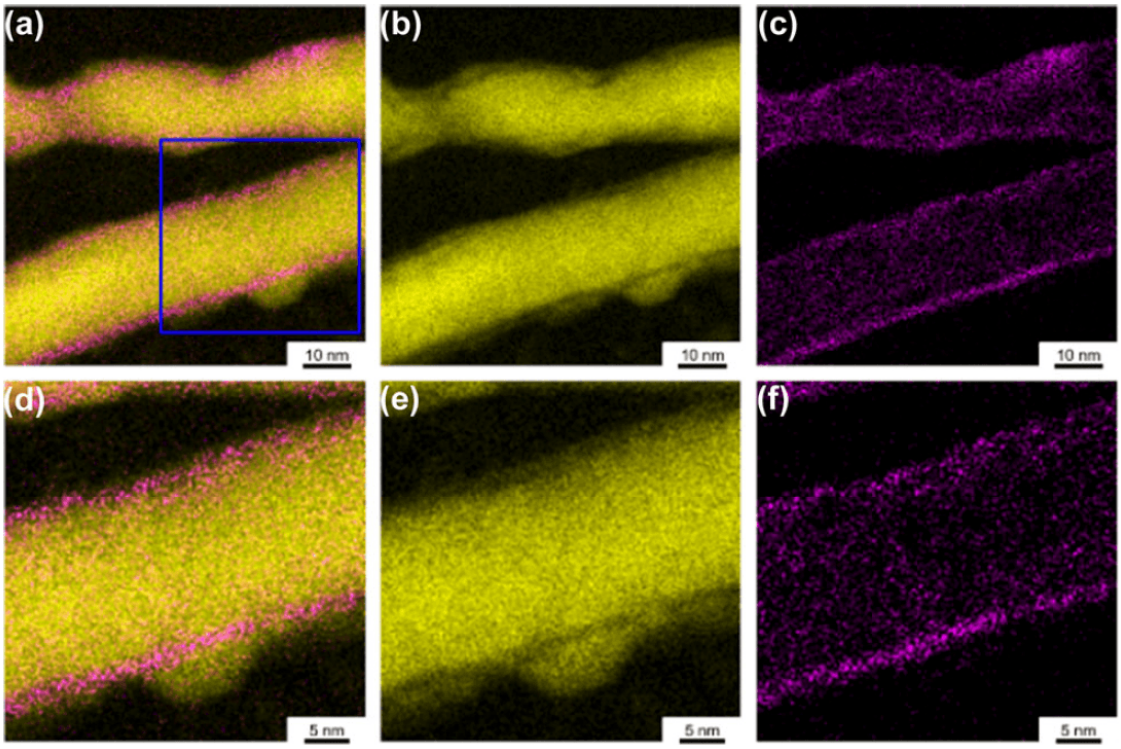


**Figure 3.8:** Electron microscopy analysis of Cu9Ag1NWs after $CO_2$RR at 1.05 V vs. RHE) for 2 h. (a) EDX mapping of Cu K and Ag L on Cu9Ag1NWs, (b) Cu component in the EDX image of Cu9Ag1NWs, (c) Ag component in the EDX image of Cu9Ag1NWs. (d) EDX mapping of a Cu ensemble with Ag on the surface of Cu9Ag1NWs (Zoom in the blue circle in (a), (e) Cu component in the EDX image of Cu and Ag ensemble on the surface of Cu9Ag1NWs, (f) Ag component in the EDX image of Cu and Ag ensemble on the surface of Cu9Ag1NWs. Yellow indicates Cu, and purple indicates Ag.

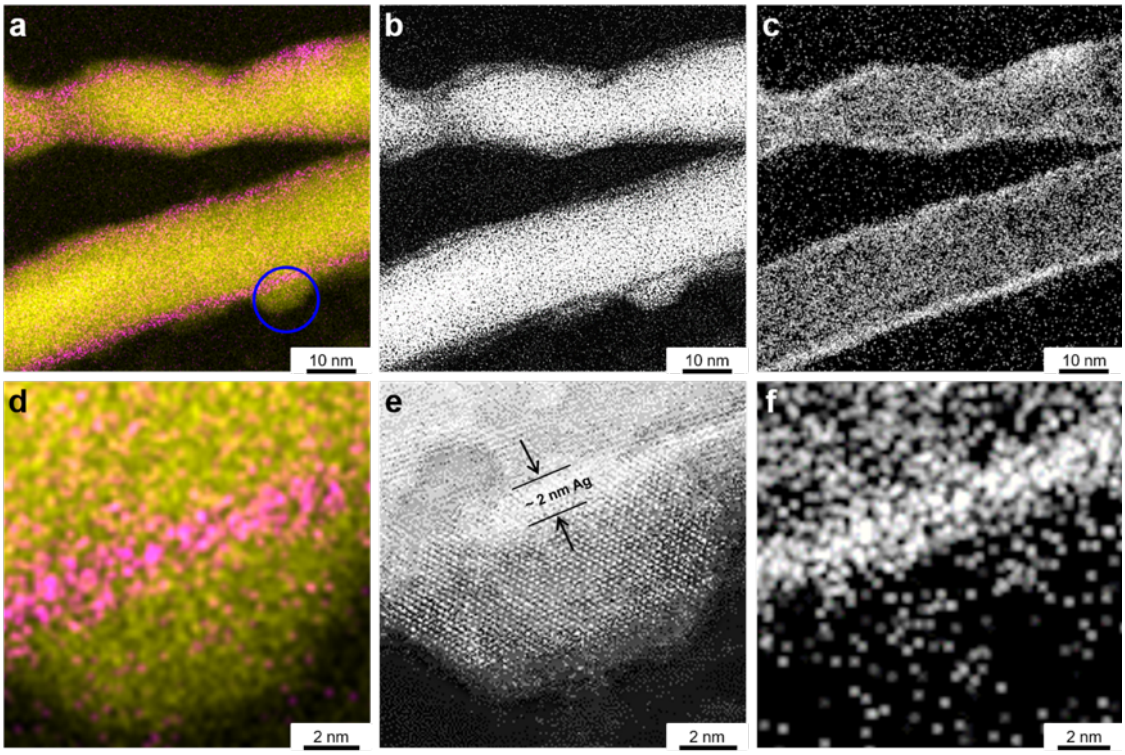


**Figure 3.9:** STEM and EDX mapping of Cu9Ag1NWs after $CO_2$RR at -1.05 (V vs.RHE) for 2 h. (a) EDX of Cu9Ag1NWs, (b) Cu component in the STEM images of Cu9Ag1NWs. (c) Ag component in the STEM images of Cu9Ag1NWs. (d) EDX of ensemble of Cu K and Ag L on the surface of Cu9Ag1NWs (Zoom in the blue circle in figure 3.9a). (e) Cu component in the STEM images of Cu and Ag ensemble on the surface of Cu9Ag1NWs. (f) Ag component in the STEM images of the Cu ensemble with Ag on the surface of Cu9Ag1NWs. Yellow is Cu and purple is Ag.

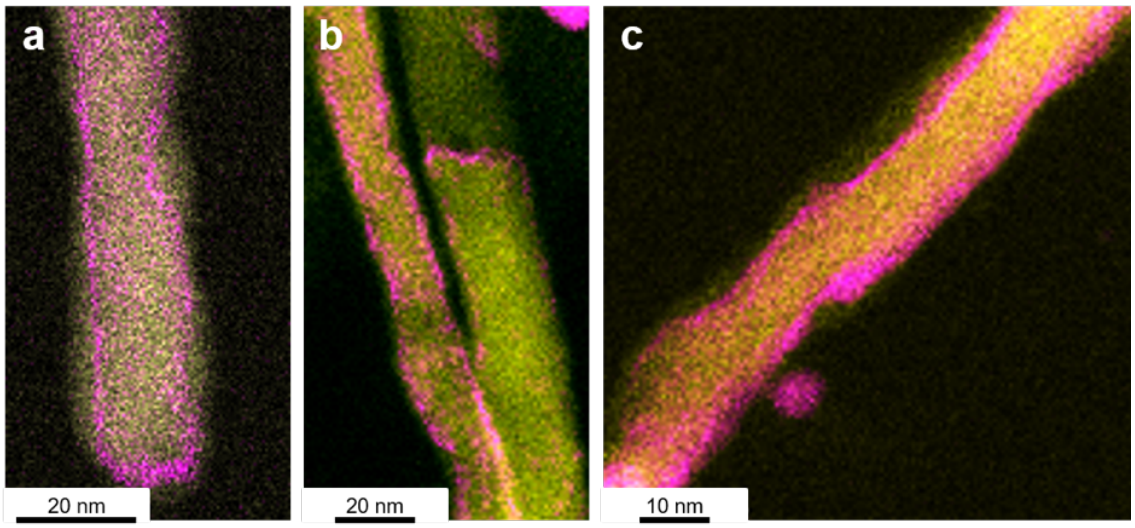


**Figure 3.10:** EDX mapping of Cu9Ag1NWs after activations with $H_2$, $CO_2$, and CO at -1.05 V vs. RHE for 30 min. (a) Purging with $H_2$, (b) Purging with $CO_2$, (c) Purging with CO. Yellow is Cu and purple is Ag.

-1.17 V vs. RHE, and maintained at 66.36 $\pm$4.18% of $FE_{CH_4}$ at -1.20 V vs. RHE (Figure 3.14b).

The reaction pathways of $CH_4$ and $C_2H_4$ share a common $*$COH intermediate, which deviates to $CH_4$ with $*$HCOH and $C_2H_4$ with $*$OC-COH ($*$active sites of catalysts)[40]. Thus, catalysts availability to adsorb H ($H_{ad}$) compared to adsorb CO ($CO_{ad}$) induces higher $CH_4$ selectivity over $C_2H_4$ selectivity. Chen et al. reported that hydrogen binding energy increases by $\sim$ 1 eV/V while the CO binding energy varies little with applied potentials[40]. Assuming dominant hydrogen coverage at more negative than -0.8 V vs. RHE,[40] at -1.12 V vs. RHE on the surface of Cu-AgNWs, the Cu portion would be covered by hydrogen (Cu-H$*$) while the surface of Ag is still dominant by CO (Ag-CO$*$). CO dominance on Ag surface is consistent with our observation of $FE_{CO}$ over 90% at $\sim$ -1.13 V vs. RHE on AgNPs (Figure 3.14d). On CuAgNWs, the diffusion of CO from Ag section to the Cu section is likely more efficient due to the short diffusion length. Thus, efficient feeding of CO to hydrogen-covered Cu surface could make it favorable to generate $*$COH, and the dominant hydrogen coverage on the Cu

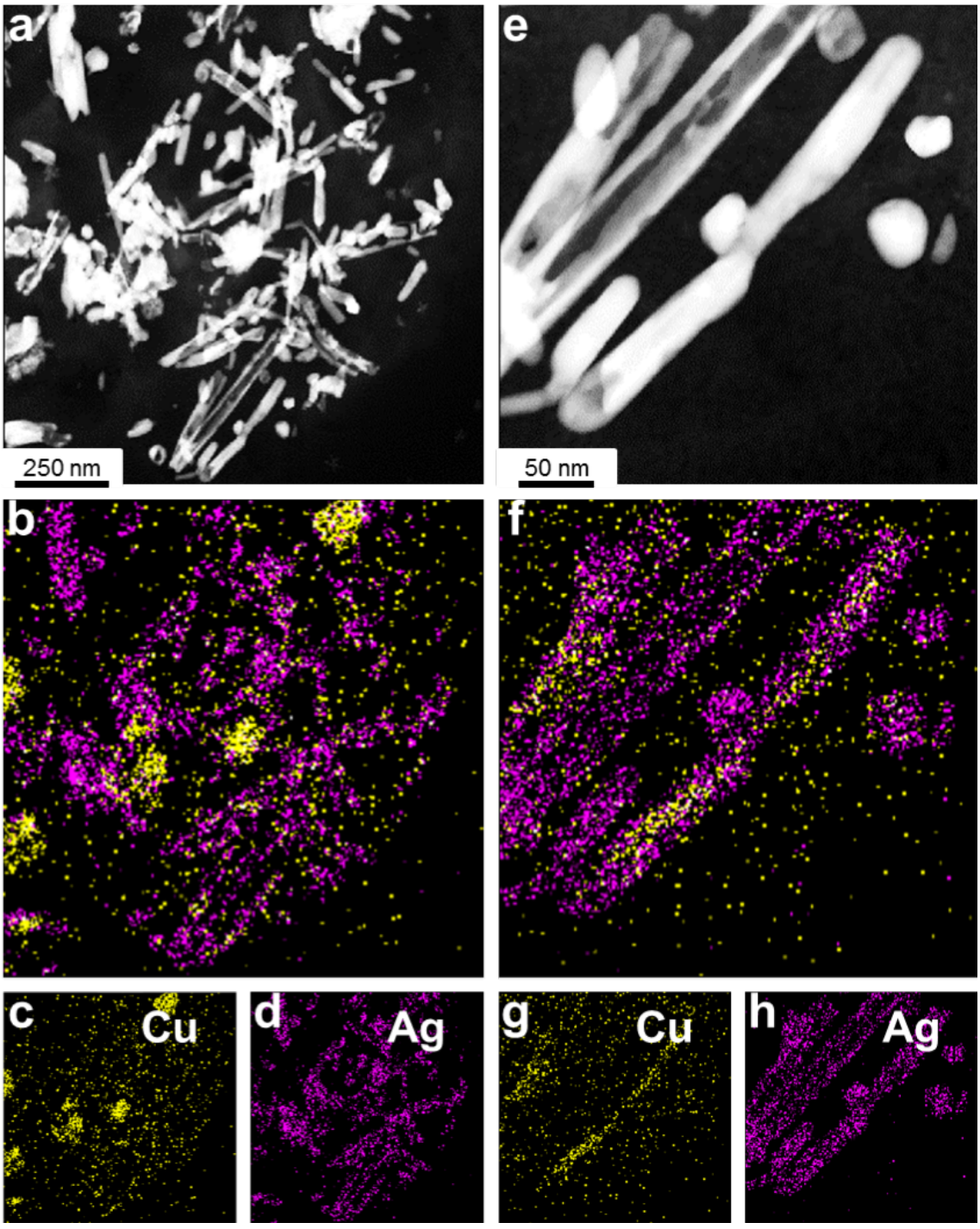


**Figure 3.11:** STEM and EDX mapping of Cu8.2Ag1.8NWs after $CO_2$RR at -1.05 V vs. RHE for 2 h. (a,e) STEM images of Cu8.2Ag1.8NWs, (b,f,c,d,g,h) EDX of Cu8.2Ag1.8 NWs. Yellow is Cu and purple is Ag.

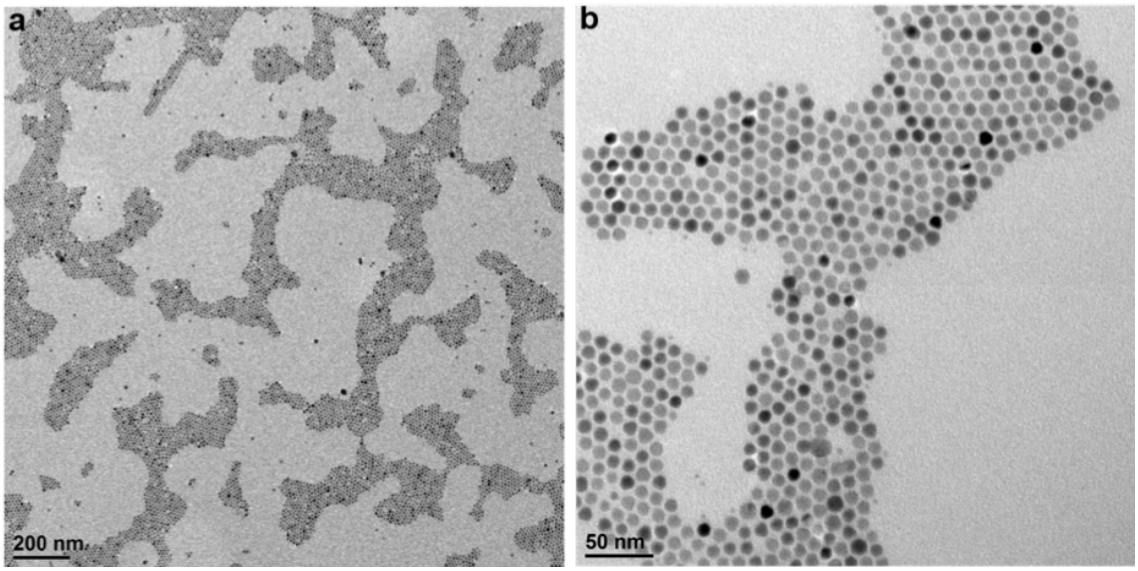


**Figure 3.12:** AgNPs. (a,b) Low magnification TEM image of AgNPs.

surface might drive ∗COH to ∗HCOH and finally $CH_4$.

To further investigate the importance of the different interfaces between Cu and Ag components for high $CH_4$ generation, we compared FEs of Cu9Ag1NWs and Cu8.2Ag1.8NWs. Both Cu9Ag1NWs and Cu8.2Ag1.8NWs showed higher selectivity of CO ( $>$ 60% $FE_{CO}$) at $\sim$ -1.05 V vs. RHE than pure CuNWs (Figure 3.14a-c), confirming contribution from the Ag component. However, the Cu8.2Ag1.8NWs still showed high CO selectivity (53.21 $\pm$ 20.00%) with low $CH_4$ production (10.55 $\pm$ 9.15%) at -1.13 $\pm$ 0.02% V vs. RHE (Table 3.2, 3.3), while Cu9Ag1NWs already demonstrated over 60% $FE_{CH_4}$. HRTEM and EDS showed larger separations between Cu and Ag components in Cu8.2Ag1.8NWs (Figure 3.11) than Cu9Ag1 (Figures 3.8).

**Table 3.2:** FE for Cu9Ag1 NWs

| Applied potentials V vs. RHE | $FE_{H_2}$ % | $FE_{CO}$ % | $FE_{CH_4}$ % | $FE_{C_2H_4}$ % | $FE_{CH_3CH_2OH}$ % | $FE_{CH_3COO^-}$ % | $FE_{HCOO^-}$ % | $FE_{Total}$ % |
|---|---|---|---|---|---|---|---|---|
| -1.05 ± 0.01 | 14.73 ± 3.56 | 55.08 ± 0.11 | 6.25 ± 0.88 | 17.34 ± 4.06 | 1.93 | 0.61 | 0.15 | 96.10 ± 8.39 |
| -1.12 ± 0.01 | 16.79 ± 4.98 | 3.16 ± 0.54 | 63.29 ± 4.85 | 21.51 ± 1.22 | 1.53 | 0.34 | 0.10 | 106.72 ± 4.17 |
| -1.20 ± 0.02 | 24.66 ± 8.11 | 2.30 ± 0.52 | 66.36 ± 4.18 | 8.89 ± 4.46 | 1.17 | 0.22 | 0.11 | 103.72 ± 5.01 |

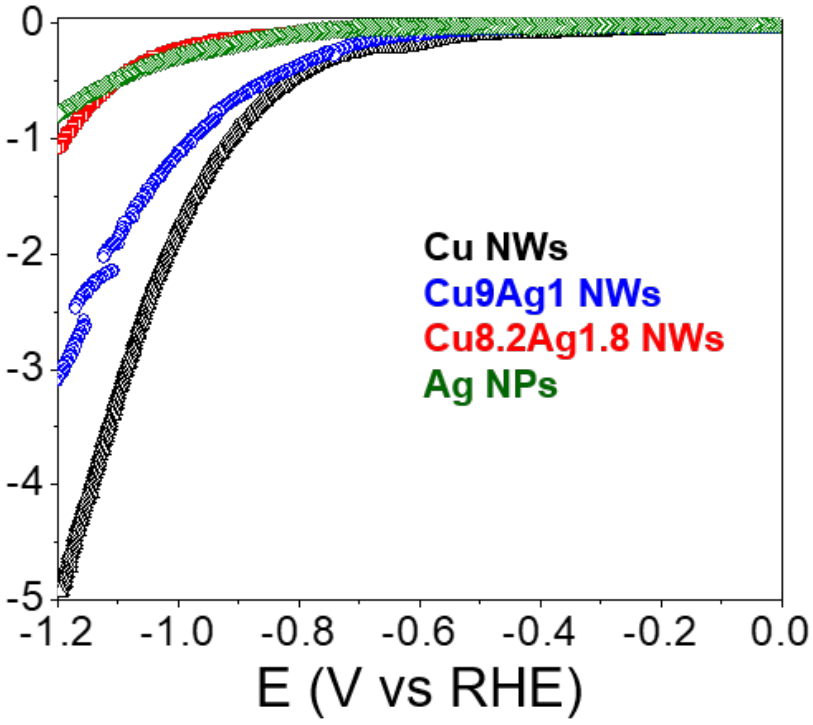


**Figure 3.13:** The electrochemically active surface area (ECSA) normalized current density. The ECSA was calculated by the double-layer capacitance of the electrodeelectrolyte interface in $CO_2$-saturated 0.1 M $KHCO_3$ solution at room temperature.

**Table 3.3:** FE for Cu8.2Ag1.8NWs

| Applied potentials V vs. RHE | $FE_{H_2}$ % | $FE_{CO}$ % | $FE_{CH_4}$ % | $FE_{C_2H_4}$ % | $FE_{CH_3CH_2OH}$ % | $FE_{CH_3COO^-}$ % | $FE_{HCOO^-}$ % | $FE_{Total}$ % |
|---|---|---|---|---|---|---|---|---|
| -1.04 | 16.36 | 82.03 | 0.05 | 2.1 | 5.09 | 1.87 | 0.61 | 108.14 |
| -1.13 ± 0.02 | 12.80 ± 2.63 | 53.21 ± 20.00 | 10.55 ± 9.15 | 19.50 ± 7.42 | 3.07 | 1.15 | 1.34 | 101.62 ± 2.12 |
| -1.23 ± 0.01 | 28.07 ± 16.16 | 25.58 ± 1.55 | 33.75 ± 7.27 | 11.21 ± 4.44 | 2.43 | 0.47 | 2.09 | 103.61 ± 10.92 |

This indicates that an intimate atomic level Cu-Ag interface between the Cu and Ag components is necessary to promote the synergistic effect of CO-Ag$*$ and H-Cu$*$ in order to promote high $CH_4$ selectivity. To the best of our knowledge, the Cu9Ag1NWs provide high $FE_{CH_4}$ at the lowest applied potential 72% of $FE_{CH_4}$ at -1.17 V vs. RHE in H-cell

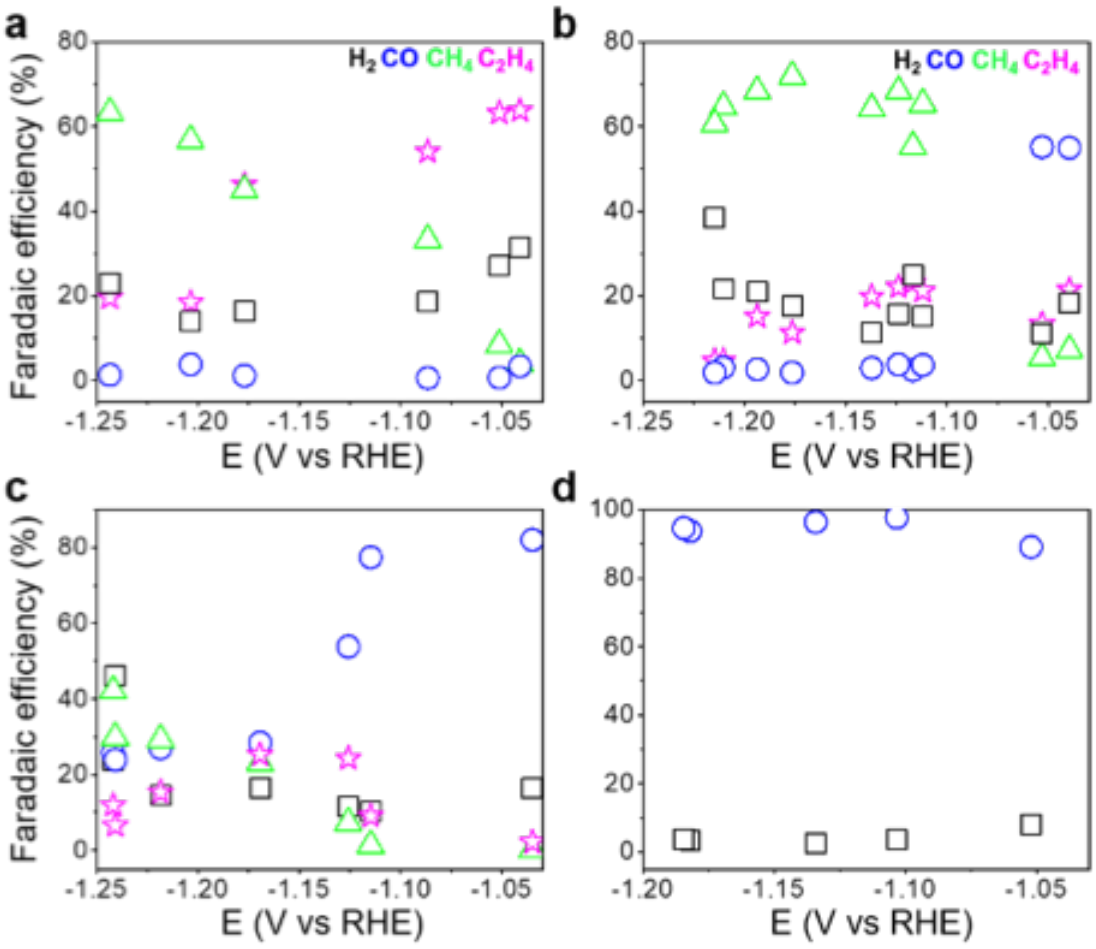


**Figure 3.14:** Electrochemical $CO_2$RR performance in 0.1 M $KHCO_3$ at room temperature and atmosphere pressure. (a) FEs of CuNWs, (b) FEs of Cu9Ag1NWs, (c) FEs of Cu8.2Ag1.8NWs, (d) FEs of AgNPs

with standard glassy carbon electrode at room temperature and atmospheric pressure (0.1 M $KHCO_3$) compared to all other materials reported in the literature to date (Table 2.1).

## 3.4 Conclusion

We successfully generated atomic Cu-Ag ensembles via ex-situ galvanic replacement from Cu to Ag, followed by an in-situ electrochemical activation approach. The atomic Cu-Ag ensemble interface showed a change of $CO_2$RR selectivity from $C_2H_4$ to $CH_4$, which remarked the highest $FE_{CH_4}$ at the lowest applied potential 72% of $FECH_4$ at -1.17 V vs. RHE in H-cell. These findings suggest an effective way to generatie unmixable atomic ensemble Cu-Ag interfaces to enhance $CH_4$ selectivity with lowerb overpotential under operando conditions. This approach can be expanded to other unmixable metal atoms to engineer the atomic ensemble interface to for desired catalytic properties.

## Bibliography


[1] Marcel Schreier, Florent Héroguel, Ludmilla Steier, Shahzada Ahmad, Jeremy S Luterbacher, Matthew T Mayer, Jingshan Luo, and Michael Grätzel. Solar conversion of $CO_2$ to CO using earth-abundant electrocatalysts prepared by atomic layer modification of Co. *Nature Energy*, 2(7):1–9, 2017.

[2] Song Lin, Christian S Diercks, Yue-Biao Zhang, Nikolay Kornienko, Eva M Nichols, Yingbo Zhao, Aubrey R Paris, Dohyung Kim, Peidong Yang, Omar M Yaghi, et al. Covalent organic frameworks comprising cobalt porphyrins for catalytic $CO_2$ reduction in water. *Science*, 349(6253):1208–1213, 2015.

[3] Shan Gao, Yue Lin, Xingchen Jiao, Yongfu Sun, Qiquan Luo, Wenhua Zhang, Dianqi Li, Jinlong Yang, and Yi Xie. Partially oxidized atomic cobalt layers for carbon dioxide electroreduction to liquid fuel. *Nature*, 529(7584):68–71, 2016.

[4] Cao-Thang Dinh, Thomas Burdyny, Md Golam Kibria, Ali Seifitokaldani, Christine M Gabardo, F Pelayo García de Arquer, Amirreza Kiani, Jonathan P Edwards, Phil De Luna, Oleksandr S Bushuyev, et al. $CO_2$ electroreduction to ethylene via hydroxide-mediated copper catalysis at an abrupt interface. *Science*, 360(6390):783–787, 2018.

[5] Yoshio Hori, Katsuhei Kikuchi, and Shin Suzuki. Production of CO and $CH_4$ in electrochemical reduction of $CO_2$ at metal electrodes in aqueous hydrogencarbonate solution. *Chemistry Letters*, 14(11):1695–1698, 1985.

[6] Tao Cheng, Hai Xiao, and William A Goddard III. Reaction mechanisms for the electrochemical reduction of $CO_2$ to CO and formate on the Cu (100) surface at 298 k from quantum mechanics free energy calculations with explicit water. *Journal of the American Chemical Society*, 138(42):13802–13805, 2016.

[7] Arnau Verdaguer-Casadevall, Christina W Li, Tobias P Johansson, Soren B Scott, Joseph T McKeown, Mukul Kumar, Ifan EL Stephens, Matthew W Kanan, and

Ib Chorkendorff. Probing the active surface sites for CO reduction on oxide-derived copper electrocatalysts. *Journal of the American Chemical Society*, 137(31):9808–9811, 2015.

[8] Xiaofeng Feng, Kaili Jiang, Shoushan Fan, and Matthew W Kanan. Grain-boundary-dependent $CO_2$ electroreduction activity. *Journal of the American Chemical Society*, 137(14):4606–4609, 2015.

[9] Christina W Li, Jim Ciston, and Matthew W Kanan. Electroreduction of carbon monoxide to liquid fuel on oxide-derived nanocrystalline copper. *Nature*, 508(7497):504–507, 2014.

[10] Christina W Li and Matthew W Kanan. $CO_2$ reduction at low overpotential on Cu electrodes resulting from the reduction of thick Cu2o films. *Journal of the American Chemical Society*, 134(17):7231–7234, 2012.

[11] Ming Ma, Kristina Djanashvili, and Wilson A Smith. Controllable hydrocarbon formation from the electrochemical reduction of $CO_2$ over Cu nanowire arrays. *Angewandte chemie international edition*, 55(23):6680–6684, 2016.

[12] Anna Loiudice, Peter Lobaccaro, Esmail A Kamali, Timothy Thao, Brandon H Huang, Joel W Ager, and Raffaella Buonsanti. Tailoring copper nanocrystals towards c2 products in electrochemical $CO_2$ reduction. *Angewandte Chemie International Edition*, 55(19):5789–5792, 2016.

[13] David Raciti, Kenneth J Livi, and Chao Wang. Highly dense Cu nanowires for low-overpotential $CO_2$ reduction. *Nano letters*, 15(10):6829–6835, 2015.

[14] Rulle Reske, Hemma Mistry, Farzad Behafarid, Beatriz Roldan Cuenya, and Peter Strasser. Particle size effects in the catalytic electroreduction of $CO_2$ on Cu nanoparticles. *Journal of the American Chemical Society*, 136(19):6978–6986, 2014.

[15] Hemma Mistry, Ana Sofia Varela, Cecile S Bonifacio, Ioannis Zegkinoglou, Ilya Sinev, Yong-Wook Choi, Kim Kisslinger, Eric A Stach, Judith C Yang, Peter Strasser, et al. Highly selective plasma-activated copper catalysts for carbon dioxide reduction to ethylene. *Nature communications*, 7(1):1–9, 2016.

[16] Yanwei Lum and Joel W Ager. Stability of residual oxides in oxide-derived copper catalysts for electrochemical $CO_2$ reduction investigated with 18o labeling. *Angewandte Chemie International Edition*, 57(2):551–554, 2018.

[17] Yanwei Lum, Binbin Yue, Peter Lobaccaro, Alexis T Bell, and Joel W Ager. Optimizing c–c coupling on oxide-derived copper catalysts for electrochemical $CO_2$ reduction. *The Journal of Physical Chemistry C*, 121(26):14191–14203, 2017.

[18] Dunfeng Gao, Yi Zhang, Zhiwen Zhou, Fan Cai, Xinfei Zhao, Wugen Huang, Yangsheng Li, Junfa Zhu, Ping Liu, Fan Yang, et al. Enhancing $CO_2$ electroreduction with the metal–oxide interface. *Journal of the American Chemical Society*, 139(16):5652–5655, 2017.

[19] Marco Favaro, Hai Xiao, Tao Cheng, William A Goddard III, Junko Yano, and Ethan J Crumlin. Subsurface oxide plays a critical role in $CO_2$ activation by Cu (111) surfaces to form chemisorbed $CO_2$, the first step in reduction of $CO_2$. *Proceedings of the National Academy of Sciences*, 114(26):6706–6711, 2017.

[20] Hai Xiao, William A Goddard III, Tao Cheng, and Yuanyue Liu. Cu metal embedded in oxidized matrix catalyst to promote $CO_2$ activation and co dimerization for electrochemical reduction of $CO_2$. *Proceedings of the National Academy of Sciences*, 114(26):6685–6688, 2017.

[21] Ruperto G Mariano, Kim McKelvey, Henry S White, and Matthew W Kanan. Selective increase in $CO_2$ electroreduction activity at grain-boundary surface terminations. *Science*, 358(6367):1187–1192, 2017.

[22] Tao Cheng, Hai Xiao, and William A Goddard. Nature of the active sites for CO reduction on copper nanoparticles; suggestions for optimizing performance. *Journal of the American Chemical Society*, 139(34):11642–11645, 2017.

[23] HA Hansen, C Shi, AC Lausche, AA Peterson, and JK Nørskov. Bifunctional alloys for the electroreduction of $CO_2$ and CO. *Physical Chemistry Chemical Physics*, 18(13):9194–9201, 2016.

[24] Christopher Hahn, David N Abram, Heine A Hansen, Toru Hatsukade, Ariel Jackson, Natalie C Johnson, Thomas R Hellstern, Kendra P Kuhl, Etosha R Cave, Jeremy T Feaster, et al. Synthesis of thin film auPd alloys and their investigation for electrocatalytic $CO_2$ reduction. *Journal of Materials Chemistry A*, 3(40):20185–20194, 2015.

[25] Dan Ren, Bridget Su-Hui Ang, and Boon Siang Yeo. Tuning the selectivity of carbon dioxide electroreduction toward ethanol on oxide-derived Cu $\times$ Zn catalysts. *Acs Catalysis*, 6(12):8239–8247, 2016.

[26] Daniel A Torelli, Sonja A Francis, J Chance Crompton, Alnald Javier, Jonathan R Thompson, Bruce S Brunschwig, Manuel P Soriaga, and Nathan S Lewis. Nickel–gallium-catalyzed electrochemical reduction of $CO_2$ to highly reduced products at low overpotentials. *ACS catalysis*, 6(3):2100–2104, 2016.

[27] Sichao Ma, Masaaki Sadakiyo, Minako Heima, Raymond Luo, Richard T Haasch, Jake I Gold, Miho Yamauchi, and Paul JA Kenis. Electroreduction of carbon dioxide to hydrocarbons using bimetallic Cu–Pd catalysts with different mixing patterns. *Journal of the American Chemical Society*, 139(1):47–50, 2017.

[28] Ezra L Clark, Christopher Hahn, Thomas F Jaramillo, and Alexis T Bell. Electrochemical $CO_2$ reduction over compressively strained CuAg surface alloys with enhanced multi-carbon oxygenate selectivity. *Journal of the American Chemical Society*, 139(44):15848–15857, 2017.

[29] Toru Hatsukade, Kendra P Kuhl, Etosha R Cave, David N Abram, and Thomas F Jaramillo. Insights into the electrocatalytic reduction of $CO_2$ on metallic silver surfaces. *Physical Chemistry Chemical Physics*, 16(27):13814–13819, 2014.

[30] JM Sanchez, JP Stark, and VL Moruzzi. First-principles calculation of the Ag -Cu phase diagram. *Physical Review B*, 44(11):5411, 1991.

[31] Thao TH Hoang, Sumit Verma, Sichao Ma, Tim T Fister, Janis Timoshenko, Anatoly I Frenkel, Paul JA Kenis, and Andrew A Gewirth. Nanoporous copper–silver alloys by additive-controlled electrodeposition for the selective electroreduction of $CO_2$ to ethylene and ethanol. *Journal of the American Chemical Society*, 140(17):5791–5797, 2018.

[32] Seunghwa Lee, Gibeom Park, and Jaeyoung Lee. Importance of Ag –Cu biphasic boundaries for selective electrochemical reduction of $CO_2$ to ethanol. *Acs Catalysis*, 7(12):8594–8604, 2017.

[33] Ying Wang, Degao Wang, Christopher J Dares, Seth L Marquard, Matthew V Sheridan, and Thomas J Meyer. $CO_2$ reduction to acetate in mixtures of ultrasmall $(Cu)_n$,$(Ag)_m$ bimetallic nanoparticles. *Proceedings of the National Academy of Sciences*, 115(2):278–283, 2018.

[34] Jianfeng Huang, Mounir Mensi, Emad Oveisi, Valeria Mantella, and Raffaella Buonsanti. Structural sensitivities in bimetallic catalysts for electrochemical $CO_2$ reduction revealed by Ag –Cu nanodimers. *Journal of the American Chemical Society*, 141(6):2490–2499, 2019.

[35] Wenlei Zhu, Ronald Michalsky, Onder Metin, Haifeng Lv, Shaojun Guo, Christopher J Wright, Xiaolian Sun, Andrew A Peterson, and Shouheng Sun. Monodisperse Au nanoparticles for selective electrocatalytic reduction of $CO_2$ to CO. *Journal of the American Chemical Society*, 135(45):16833–16836, 2013.

[36] Daniel L Reger, Scott R Goode, and David W Ball. *Chemistry: principles and practice*. Cengage Learning, 2009.

[37] H Shinotsuka, S Tanuma, CJ Powell, and DR Penn. Calculations of electron inelastic mean free paths. x. data for 41 elemental solids over the 50 ev to 200 kev range with the relativistic full penn algorithm. *Surface and Interface Analysis*, 47(9):871–888, 2015.

[38] Seoin Back, Heejin Kim, and Yousung Jung. Selective heterogeneous $CO_2$ electroreduction to methanol. *Acs Catalysis*, 5(2):965–971, 2015.

[39] Miao Zhong, Kevin Tran, Yimeng Min, Chuanhao Wang, Ziyun Wang, Cao-Thang Dinh, Phil De Luna, Zongqian Yu, Armin Sedighian Rasouli, Peter Brodersen, et al. Accelerated discovery of $CO_2$ electrocatalysts using active machine learning. *Nature*, 581(7807):178–183, 2020.

[40] Tao Cheng, Hai Xiao, and William A Goddard III. Full atomistic reaction mechanism with kinetics for CO reduction on Cu (100) from ab initio molecular dynamics free-energy calculations at 298 k. *Proceedings of the National Academy of Sciences*, 114(8):1795–1800, 2017.

# CHAPTER 4

# Electrochemical $CO_2$RR to Hydrocarbons on Cu plates with Ag and Pd Decoration

## 4.1 Introduction

As climate change is intensified by carbon dioxide ($CO_2$) emissions threatening the human living environment, it is urgent to develop an effective and sustained solution to reduce emissions of $CO_2$. Electrochemical $CO_2$ reduction ($CO_2$RR) driven by clean electricity is a potential technology that stores inconsistent renewable energy like solar, wind, and hydropower into stable and convenient utilized chemicals while consuming $CO_2$ simultaneously. To date, copper (Cu) is the only known metal that can produce hydrocarbons and oxygenates effectively.[1] One of the key challenges of industrializing this technology is to improve product selectivity toward the desired product that either possesses high energy density or is easier to transport and compatible with energy infrastructure. Hydrocarbon products with multicarbon such as ethylene, are highly attractive because of their versatility in the chemical and energy industries.[2]

Tuning selectivity of electrochemical $CO_2$RR is hindered by the limited understanding of the complex reaction networks. Multiple C-C formation mechanisms were reported for Cu-based catalysts so far, which all process through $*$CO: the dimerization of $*$CO forming OC$**$CO is supported by theoretical simulation[3] and in situ spectroscopy experiment[4]; the coupling of $*$CHO to form $*$OCHCHO$*$;[5] and coupling between $*$CHO and $*$CO to form O$*$CCHO.[6] Key factors determine whether the C-C coupling is kinetically favorable,

including the local ∗CO concentration near the $C_2$ catalysis site, the ∗CO binding energy on the catalyst, and the protonation of ∗CO to ∗CHO for the ∗OCHCHO∗ and O∗CCHO pathway.

A lot of effort has been put into increasing the local ∗CO concentration and adjusting ∗CO binding energy to promote the C–C coupling process. Incorporating Cu with a secondary element has proven effectively tune the $CO_2$RR toward $C_2$ products.[7–14] According to the Sabatier principle, the corresponding intermediate should be bound neither too strongly nor too weakly for each elementary catalysis step.[15] In other words, the binding energy for activation or release should be optimized. Metal exhibiting weak ∗CO binding energy like Ag and Au has a higher turnover frequency (TOF) of converting $CO_2$ to CO. Metal exhibiting strong ∗CO binding like Pd will be poisoned while further reduction is terminated. Optimizing binding energy for processes involving multiple steps and intermediates is restricted by the scaling relationship, as discussed in Chapter 1. Incorporating Cu with foreign elements supplies diverse catalysis sites, which can be optimized for each step separately (synergistic effect), thus freeing researchers from constriction from the linear scaling relationship.

Among all those elements, Ag and Pd, located near Cu while on the opposite side on the scaling relations diagram shown in Figure 4.1[16], have been reported effectively enhance $CO_2$RR performance when incorporated with Cu. Various main products, including carbon monoxide (CO), methane ($CH_4$), ethylene ($C_2H_4$), and ethanol ($C_2H_5OH$), were reported and summarized in table 4.1. It indicates that the selectivity of the bimetallic catalysts is not just determined by the type of the element, but also by the composition and assembly pattern. The details of how foreign elements contribute to $CO_2$RR are still a puzzle. The contribution of foreign atoms to the Cu catalysts' performance of $CO_2$RR can be a mix of geometric and electronic effects. The ratio of activation sites for ∗CO production and the C-C coupling process, the distance between these selective activation sites, lattice strain introduced by dissolving foreign atoms, and the elements' mixing patterns should be considered in the catalyst design. Despite the unclear mechanism, We found that both Ag and Pd promote

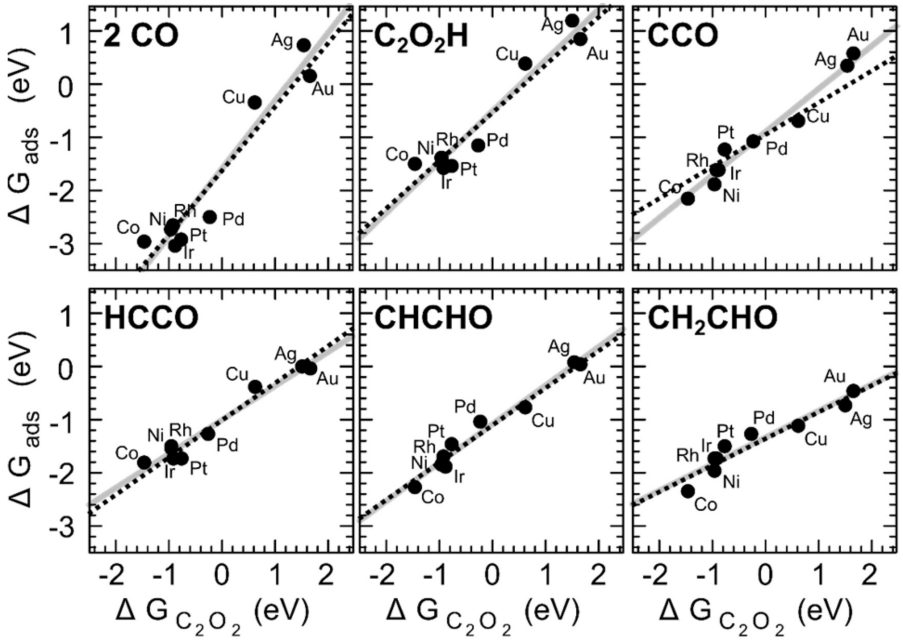


**Figure 4.1:** Adsorption energies $\Delta G_{ads}$ of $CO_2RR$ intermediates as a function of $\Delta G_{C_2O_2}$. Solid lines are the least-squares estimated scaling relations. dotted lines represent slopes estimated using bond counts. Figure adapted from ref[16]

the hydrocarbon production, especially for $C_2H_4$. $C_2H_4$ is an important value-added product that can be used as the building block for various plastics, including polyethylene, polyvinyl chloride, polystyrene and polymers.[17]

**Table 4.1:** Summary of $CO_2RR$ on CuAg and CuPd Catalysts

| Catalysts | Ag or Pd ratio | Potentials (V vs. RHE) | Maximum FE (%) | Electrolyte | Cell | Reference |
|---|---|---|---|---|---|---|
| CuAgNWs | 10 % Ag | -1.17 | 72 % $CH_4$ | 0.1 M $KHCO_3$ | H-cell | [7] |
| AgCu Nanodimers | 47.6 % Ag | -1.1 | 40% $C_2H_4$ | 0.1 M $KHCO_3$ | H-cell | [8] |
| Cosputtering Cu and Ag on PTFE | 14 % Ag | -0.84 | 37% ethanol | 1 M $KHCO_3$ | flow cell | [9] |
| CuAg alloy films | 6 % Ag | -0.7 | 60% $C_2H_4$ | 1 M KOH | flow cell | [10] |
| Ag core Cu shell | 80 % Ag | -1.06 | 32% $C_2H_4$ | 0.1 M $KHCO_3$ | H-cell | [11] |
| $Cu_3Pd$ (20 nm) | 25% Pd | -1.2 | 40% $CH_4$ | 0.1 M $KHCO_3$ | H cell | [12] |
| CuPd (50 nm) | 50% Pd | -0.7 | 48% $C_2H_4$ | 1 M KOH | Flow cell | [13] |
| $Pd_7Cu_3$ | 70% Pd | -0.8 | 80% CO | 0.1 M $KHCO_3$ | H cell | [14] |

For this reason, we grow Ag or Pd with various compositions on Cu plates (CuAg plates and CuPd plates, respectively) with dominant (111) facet exposure as a platform to study their $CO_2$RR activity and selectivity as a function of elemental composition. Moreover, majority of these research focus on bimetallic catalyst while very few research reports ternary metal system. We thought since Ag and Pd were assumed function in discrete stages of $C_2$ production, co-incorporate Ag and Pd might icing the cake. With proper alignment, it is promising to break the scaling relationship geometrically and control the mixed reaction pathway to the $C_2$ direction, with Ag serving as the $*$CO supplier. At the same time, Pd stabilizes $*$CO and supplies proton to increase the local concentration of $*$CO and $*$CHO.

Here we first grow Ag or Pd on Cu plates through galvanic replacement. We studied the $CO_2$RR on CuAg and CuPd plates with three compositions (atomic ratio of Ag or Pd to Cu ) variables. Followed by a rational design of a trimetallic CuPdAg catalyst which effectively improved the Faradaic efficiency (FE) of $C_2H_4$ ($FE_{C_2H_4}$) by 28.7% at -1.1V vs. the reversible hydrogen electrode (RHE) compared to Cu plates.

## 4.2 Materials and Methods

### Chemicals

Copper (II) chloride dihydrate ($CuCl_2 \cdot 2H_2O$, 99.999%), Palladium(II) chloride ($PdCl_2$, 99%), Hexadecylamine (HDA) ($> 98\%$), D-(+)-Glucose ($\geq 99.5\%$), Ethanol ($C_2H_5OH$) (200 proof) and potassium bicarbonate ($KHCO_3$), Cu nanoparticles (Cu nps, 25 nm particle size) were all purchased from Sigma-Aldrich. Silver Nitrate ($AgNO_3$, 99.9%) and Hexanes (98%) were purchased from Fisher Chemical. An ultrapure purification system (Milli-Q advantage A10) produced the deionized water (DI) (18.2 MΩ cm) used to make the solutions. The cation membranes were purchased from the Fuel Cell Store. All reagents were used as received without further purification.

### Synthesis of CuAg, CuPd, and CuPdAg Catalysts

The Cu plates were synthesized through a chemical reduction of $CuCl_2 \cdot 2H_2O$ by glucose in the presence of HDA. 315 mg $CuCl_2 \cdot 2H_2O$, 750 mg glucose, 2 g HDA, 7.5 ml 0.03M NaI solution and 142.5 ml DI water were added into a glass bottle (200 ml) and sonicated for 30 min for thoroughly mixing. The vial was then heated from room temperature to 100 °C in oil bath and kept at 100 °C for 8 hours. The resulting Cu plates product was collected by centrifuge at 9500 rmp and washed five times by DI water, ethanol and hexane.

CuAg plates were synthesized through a galvanic replacement reaction between $AgNO_3$ and Cu plates. 0.4 mg, 1.1 mg, and 9.4 mg $AgNO_3$ were added into the 20 mg Cu plates dispersed in DI water and sonicated for 30 minutes. CuPd plates were synthesized through a galvanic replacement reaction between $PdCl_2$ and Cu plates. 0.5 mg, 1.1 mg, and 9.3 mg $PdCl_2$ were added into the 20 mg Cu plates dispersed in DI water and sonicated for 30 minutes. The resulting CuAg and CuPd plates were then washed five times with DI water and ethanol and collected by centrifuge. CuPdAg plates were synthesized by mixing 1.9 mg 1mg/ml $PdCl_2$ and 20 mg Cu plates in DI water, sonicated for 30minutes, washed once by DI water. Then 1.9 mg $AgNO_3$ was added into the CuPd suspension sonicated for 30 minutes, and washed with DI water.

### Materials Characterization

TEM images were taken with an FEI Titan scanning transmission electron microscope (S/TEM) equipped with an energy dispersive spectrometer (EDX) detector operated at 300kV. Elemental quantification was conducted by measuring the x-ray emission from the Cu K and the Ag L levels upon excitation by an electron beam (300 kV). The thickness of Cu nanoplates was measured using Bruker Dimension FastScan Scanning Probe Microscope (SPM) under ScanAsyst mode. The crystal structure of the Cu, CuAg, CuPd and CuPdAg plates was analyzed with a Panalytical X'Pert Pro X-ray Powder Diffractometer (XRD)

using Cu K$\alpha$ radiation source conducting symmetric measurements. X-ray photoelectron spectroscopy (XPS) tests were conducted to quantify the near-surface composition of the Cu, Ag, and Pd. All spectra were acquired using monochromatized Al K$\alpha$ radiation (15 kV, 15 mA) with a Kratos AXIS Ultra DLD spectrometer. Near-surface elemental quantification was conducted by integrating the Cu 2p, Ag 3d, and Pd 3d spectral features using a Shirley background and normalizing their integrated areas by an internally calibrated relative sensitivity factor. The relative bulk concentration of Cu, Ag, and Pd was analyzed using Inductively Coupled Plasma Optical Emission Spectrometry (ICP-OES). A calibration curve was first obtained by measuring standard Cu, Ag and Pd solutions. Then catalysts were dissolved in 70% $HNO_3$ for 5 hours. The solution was then dried at 60 °C and dissolved in 2% $HNO_3$. The concentration of $Cu^{2+}$, $Ag^{+}$, and $Pd^{2+}$ were obtained by comparing with the calibration curve.

**Electrochemical Measurements**

For each Catalyst, dried particles (4 mg) were mixed with 1 ml of ethanol and ultrasonicated for 10 minutes. 10 $\mu$l of Nafion (5 wt%) was added, and ultrasonication continued for an extra 30 min. The catalyst ink (10 $\mu$l) was dropped onto an L-shaped glass-carbon electrode (diameter, 6mm; area, 0.283 $cm^2$) using a 20 $\mu$l pipette and dried under ambient air.

All electrochemical experiments were conducted in an H-cell composed of two compartments and separated by a cation-exchange membrane. The cell was sonicated with 2% nitric acid and boiled with DI water three times before each test. The counter electrode was a Pt wire from Pine Instruments. An Ag/AgCl (4M KCl) electrode purchased from Pine Instruments was used as the reference electrode. 0.1 M $KHCO_3$ was prepared as the electrolyte. The cathode is stirred by a stir bar to mix the electrolyte thoroughly. $CO_2$ (Air gas, 99.99%) was purged at a rate of 11 sccm to the cathode chamber for 25 minutes to saturate before electrochemical measurements. Electrochemical measurements were performed using a Princeton potentiostat (VersaSTAT 4). All current density was normalized by the ECSA

area measured by double-layer capacitance. Cyclic voltammetries were carried in a four-neck bottle with $CO_2$ saturated 0.1M $KHCO_3$ at scan rates of 20, 40, 60, 80, 100, 120, 140, and 160 mV/s. The double-layer capacitance was determined by calculating the slope of the current density vs. scan rate as follows:

$$C_{DL} = \frac{i_c}{v} \tag{4.1}$$

A relative surface roughness factor SRF is defined by:

$$SRF_{Cu_{\mathrm{i}}} = \frac{C_{DLCu_{\mathrm{i}}}}{C_{DLglasscarbon}} \tag{4.2}$$

$Cu_{\mathrm{i}}$: Catalysts including Cu nps, Cu plates, $Cu_{99.2}Ag_{0.8}$, $Cu_{93.9}Ag_{6.1}$, $Cu_{80.3}Ag_{19.7}$, $Cu_{99.5}Pd_{0.5}$, $Cu_{97.6}Pd_{2.4}$, $Cu_{90.1}Pd_{9.9}$ and $Cu_{92.6}Pd_{3.2}Ag_{4.2}$.

$C_{DLCu_{\mathrm{i}}}$: Double-layer capacitance of catalysts;

$C_{DLglasscarbon}$: Double-layer capacitance of glass-carbon electrode;

The specific current density of catalysts are denoted as follows:

$$j_{Cui} = \frac{j_{geo}}{SRF_{Cui}} \tag{4.3}$$

The results of the double-layer capacitance measurement are summarized in table 4.2.

A constant voltage was applied for 20 to 30 minutes before the effluent was injected into a gas chromatograph (GC). Consumed charges were collected to calculate from Princeton Applied Research VersaSTAT 4 workstation. All $CO_2$ reduction electrochemical data were recorded vs. the reference electrode and converted to the RHE scale after iR correction.

Gas products were analyzed by a gas chromatography instrument (Shimadzu GC-2010-Plus) equipped with a BID detector and a Restek ShinCarbon ST Micropacked column (2m 1mmID). The effluent from the electrochemical cell was injected into GC through a 6-port valve. The concentrations of gas samples were calculated from the calibration curve made from external standards. The FE was calculated from

$$FE_i = \frac{n_e \cdot F \cdot C_i \cdot r_G \cdot P_o}{R \cdot T_o \cdot I_{sat}} \times 100\% \tag{4.4}$$

**Table 4.2:** Summary of electrochemical double layer capacitance measurement on glass carbon, Cu nps, Cu plates, $Cu_{99.2}Ag_{0.8}$, $Cu_{93.9}Ag_{6.1}$, $Cu_{80.3}Ag_{19.7}$, $Cu_{99.5}Pd_{0.5}$, $Cu_{97.6}Pd_{2.4}$, $Cu_{90.1}Pd_{9.9}$, and $Cu_{92.6}Pd_{3.2}Ag_{4.2}$.

| | **glass carbon** | **Cu nps** | **Cu plates** | **$Cu_{99.2}Ag_{0.8}$** | **$Cu_{93.9}Ag_{6.1}$** |
|---|---|---|---|---|---|
| $C_{Dl}$ mF/cm$^2$ | 0.084 | 0.560 | 0.262 | 0.372 | 0.297 |
| SRF | 1.000 | 6.667 | 3.119 | 4.429 | 3.536 |
| $R^2$ | 0.996 | 1.000 | 0.990 | 0.995 | 1.000 |
| | **$Cu_{80.3}Ag_{19.7}$** | **$Cu_{99.5}Pd_{0.5}$** | **$Cu_{97.6}Pd_{2.4}$** | **$Cu_{90.1}Pd_{9.9}$** | **$Cu_{92.6}Pd_{3.2}Ag_{4.2}$** |
| $C_{Dl}$ mF/cm$^2$ | 0.367 | 0.287 | 0.339 | 0.471 | 0.839 |
| SRF | 0.998 | 3.417 | 4.036 | 5.607 | 9.988 |
| $R^2$ | 0.998 | 0.999 | 0.996 | 0.999 | 1.000 |

where:

$n_e$ = number of electrons transferred;

$F$ = Faraday constant (96485 $C \cdot mol^{-1}$);

$i$ = species, either $H_2$, CO, $CH_4$ or $C_2H_4$;

$C_i$ = concentration of the gas read from GC-BID;

$r_G$ = gas flow rate acquired from a ProFlow 6000 electronic flow meter (Restek) at the exit of the electrochemical cell (ml min$^{-1}$ at room temperature and ambient pressure);

$P_0$ = atmospheric pressure ($101325Pa$);

R = ideal gas constant ($8.314J \cdot mol^{-1} \cdot K^{-1}$);

$T_0$ = room temperature ($298.15K$);

$I_{sat}$ = current after saturation;

Liquid products were analyzed by Quantitative NMR spectroscopy (Bruker AV-300). Specifically, 0.1ml $D_2O$ was added to 0.9 ml of the cathode electrolyte, and 10 l of dimethyl

sulfoxide (17.75 $\mu$M) was mixed in as an internal standard. The one-dimensional 1H spectrum was measured with a prewater saturation method.

## 4.3 Results and Discussion

The growth of Cu plates is related to the reaction kinetics. The 2D morphology is normally not thermodynamically favored during the growth of Cu nanocrystals due to the high surface-to-volume ratio.[18] In this work, the 2D growth of Cu is controlled kinetically by capping agent $I^-$. Halide ions were proved capable of adjusting metal morphology during crystal growth.[19] Mirkin et al.[20] demonstrated that $I^-$ ions can bind strongly and selectively to the Au (111) crystal facet and promote the formation of (111)-oriented Au nanoprisms. Tae-Wook Kim et al.[21] reported that when iodide is present in the solution, it preferentially adsorbed on the (111) facet of the Cu and formed an adlayer. The adsorption of $I^-$ leads to anisotropic plate-like growth of the fcc nanocrystal. The transmission electron microscope (TEM) image in figure 4.2b shows that the as-synthesized Cu plates are triangular and truncated triangular structures with edge lengths ranging in the micrometer scale. The Cu plates topography measured by atomic force microscopy (AFM) reveals that the thickness of the Cu plates is $\sim$ 40 nm. The X-ray diffraction (XRD) patterns in Figure 11d show prominent peaks at 43.3° and 74.2°, corresponding to the diffractions from the {111} and {220} of face-centered-cubic Cu (JCPDS #03-1018).

To study the effect of composition on catalyst activity and selectivity, we prepared CuPd plates with three Cu: Pd atomic ratios and CuAg plates with three Cu: Ag atomic ratios. CuAg and CuPd plates were synthesized by galvanic replacement reaction between Cu atoms and $Ag^+$ or $Pd^{2+}$ ions. Ag or Pd to Cu ratio is tuned by adjusting the amount of $AgNO_3$, or $PdCl_2$ added to the Cu plates. CuAg plates were synthesized by adding 0.4 mg, 1.1 mg, and 9.4 mg $AgNO_3$ solution into 20 mg clean Cu plates dispersed in DI water and sonicated

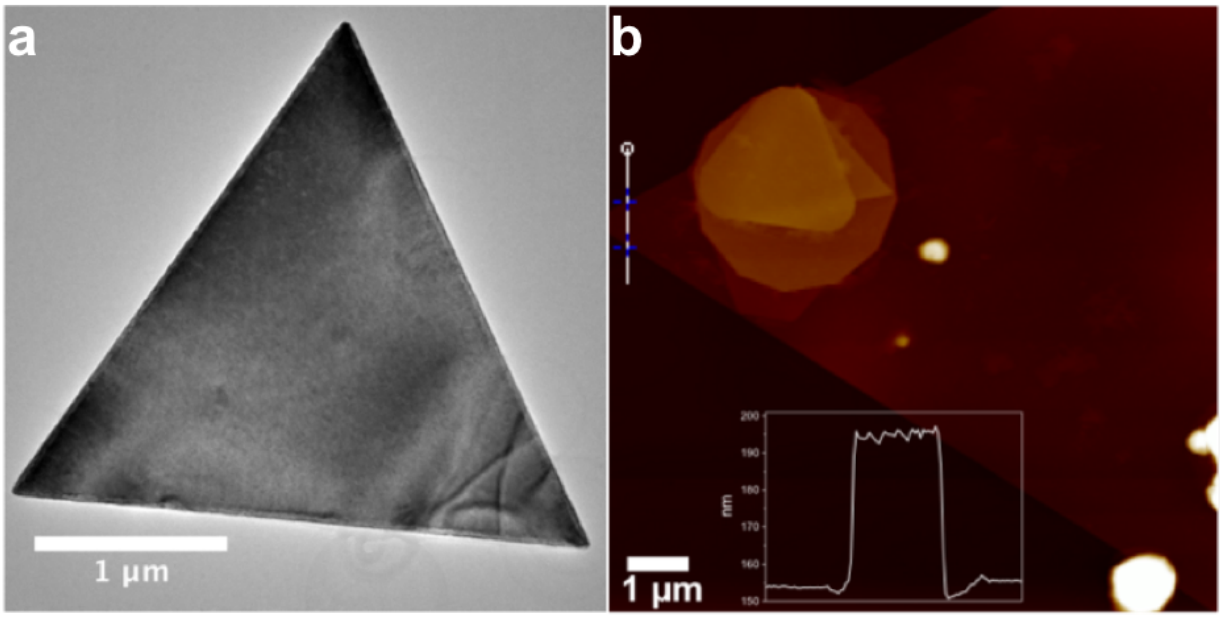


**Figure 4.2:** Characterization of Cu plates, (a) TEM image of triangular Cu plates. (b) The AFM image shows the thickness of a single Cu plate.

for 30 minutes. The corresponding reaction equations are shown below:

$$Cu_{(s)} + 2Ag^{+}_{(aq)} \rightarrow \ Cu^{2+}_{(aq)} + 2Ag_{(s)} \tag{4.5}$$

CuPd plates were synthesized by adding 0.5 mg, 1.1 mg, and 9.3 mg $PdCl_2$ solution into 20 mg clean Cu plates dispersed in DI water and sonicated for 30 minutes. The corresponding reaction equations are shown below:

$$Cu_{(s)} + Pd^{2+}_{(aq)} \rightarrow \ Cu^{2+}_{(aq)} + Pd_{(s)} \tag{4.6}$$

The bulk and surface compositions between Ag, Pd and Cu were quantified by inductively coupled plasma atomic emission spectroscopy (ICP-AES) and X-ray photoelectron spectroscopy (XPS). The result is summarized in table 4.3.

In the case of XPS (Figure 4.3), the calculated electron inelastic mean free paths of Cu at 992.3 eV, Ag 365 eV, and Pd 330.3 eV are 1.67 nm, 0.727 nm, and 0.625 nm, respectively,[22]

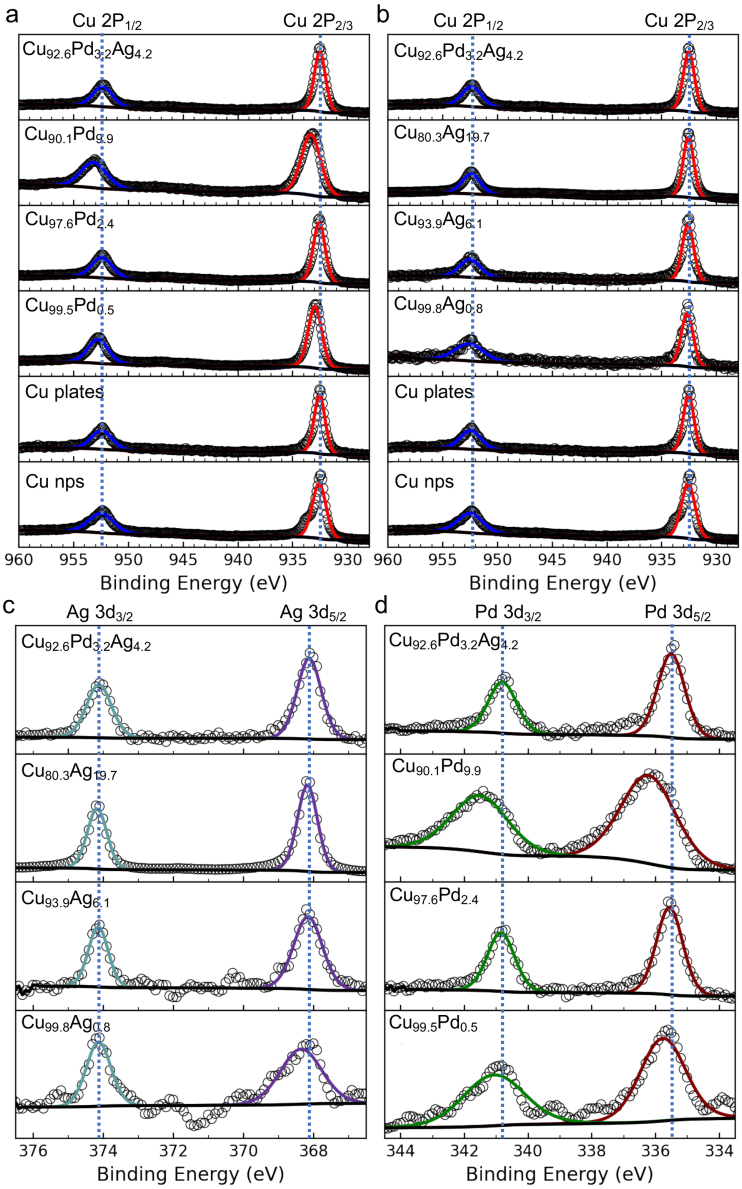


**Figure 4.3:** High-resolution XPS spectra of (a) Cu 2p region for Cu nps, Cu plates, $Cu_{99.5}Pd_{0.5}$, $Cu_{97.6}$Pd2.4, $Cu_{90.1}Pd_{9.9}$ and $Cu_{92.6}Pd_{3.2}Ag_{4.2}$. (b) Cu 2p region for Cu nps, Cu plates, $Cu_{99.2}Ag_{0.8}$, $Cu_{93.9}Ag_{6.1}$, $Cu_{80.3}Ag_{19.7}$ and $Cu_{92.6}Pd_{3.2}Ag_{4.2}$ plates. (c) Ag 3d region for $Cu_{99.2}Ag_{0.8}$, $Cu_{93.9}Ag_{6.1}$, $Cu_{80.3}Ag_{19.7}$ and $Cu_{92.6}Pd_{3.2}Ag_{4.2}$ plates. (d) Pd 3d region for $Cu_{99.5}Pd_{0.5}$, $Cu_{97.6}$Pd2.4, $Cu_{90.1}Pd_{9.9}$ and $Cu_{92.6}Pd_{3.2}Ag_{4.2}$ plates. All the spectra are background corrected.

**Table 4.3:** The atomic compositions of CuAg, CuPd and CuPdAg plates measured by ICP and XPS.

| | ICP | | | XPS | | |
|---|---|---|---|---|---|---|
| **Sample Name** | **Cu at%** | **Ag at%** | **Pd at%** | **Cu** at% | **Ag at%** | **Pd at%** |
| Cu nps | 100 | / | / | 100 | / | / |
| Cu plates | 100 | / | / | 100 | / | / |
| $Cu_{99.1}Ag_{0.8}$ | 97.99 | 2.01 | / | 99.12 | 0.8 | / |
| $Cu_{93.9}Ag_{6.1}$ | 91.89 | 8.11 | / | 93.88 | 6.12 | / |
| $Cu_{80.3}Ag_{19.7}$ | 81.04 | 18.96 | / | 80.28 | 19.72 | / |
| $Cu_{99.5}Pd_{0.5}$ | 98.14 | / | 1.86 | 99.47 | / | 0.53 |
| $Cu_{97.6}Pd_{2.4}$ | 96.45 | / | 3.55 | 97.62 | / | 2.38 |
| $Cu_{90.1}Pd_{9.9}$ | 84.35 | 0.00 | 15.65 | 90.09 | 0.00 | 9.91 |
| $Cu_{92.6}Pd_{3.2}Ag_{4.2}$ | 93.14 | 3.57 | 3.29 | 92.64 | 4.16 | 3.20 |

which reveals a surface limited component analysis of XPS for Cu, Ag and Pd element. The surface composition from XPS analysis showed 99.1% of Cu and 0.8% of Ag ($Cu_{99.1}Ag_{0.8}$) with 0.4 mg $AgNO_3$ precursor; 93.9% of Cu and 6.1% of Ag ($Cu_{93.9}Ag_{6.1}$) with 1.1 mg $AgNO_3$ precursor; and 80.28% of Cu and 19.72% of Ag ($Cu_{80.3}Ag_{19.7}$) with 9.4 mg $AgNO_3$ precursor. For CuPd plates, XPS analysis showed 99.47% of Cu and 0.53% of Pd ($Cu_{99.5}Pd_{0.5}$) with 0.5 mg $PdCl_2$ precursor; 97.62% of Cu and 2.38% of Pd ($Cu_{97.6}Pd_{2.4}$) with 1.1 mg $PdCl_2$ precursor; 90.09% of Cu and 9.91% of Pd ($Cu_{90.1}Pd_{9.9}$) with 9.3 mg $PdCl_2$ precursor; The concentrations measured by ICP are overall smaller than those of XPS indicate a tandem structure of CuAg and CuPd plates. For the CuPdAg plates, the surface concentration measured by XPS showed 92.64% Cu, 4.16% Ag, and 3.20% of Pd ($Cu_{92.6}Pd_{3.2}Ag_{4.2}$).

High-angle annular dark-field imaging (HAADF) and Energy-dispersive X-ray spectroscopy (EDX) were applied to study the distribution of Ag and Pd particles (Figure 4.4). The pure Cu plates showed sharp and clean surfaces (Figure 4.2b). The Cu plates morphology was

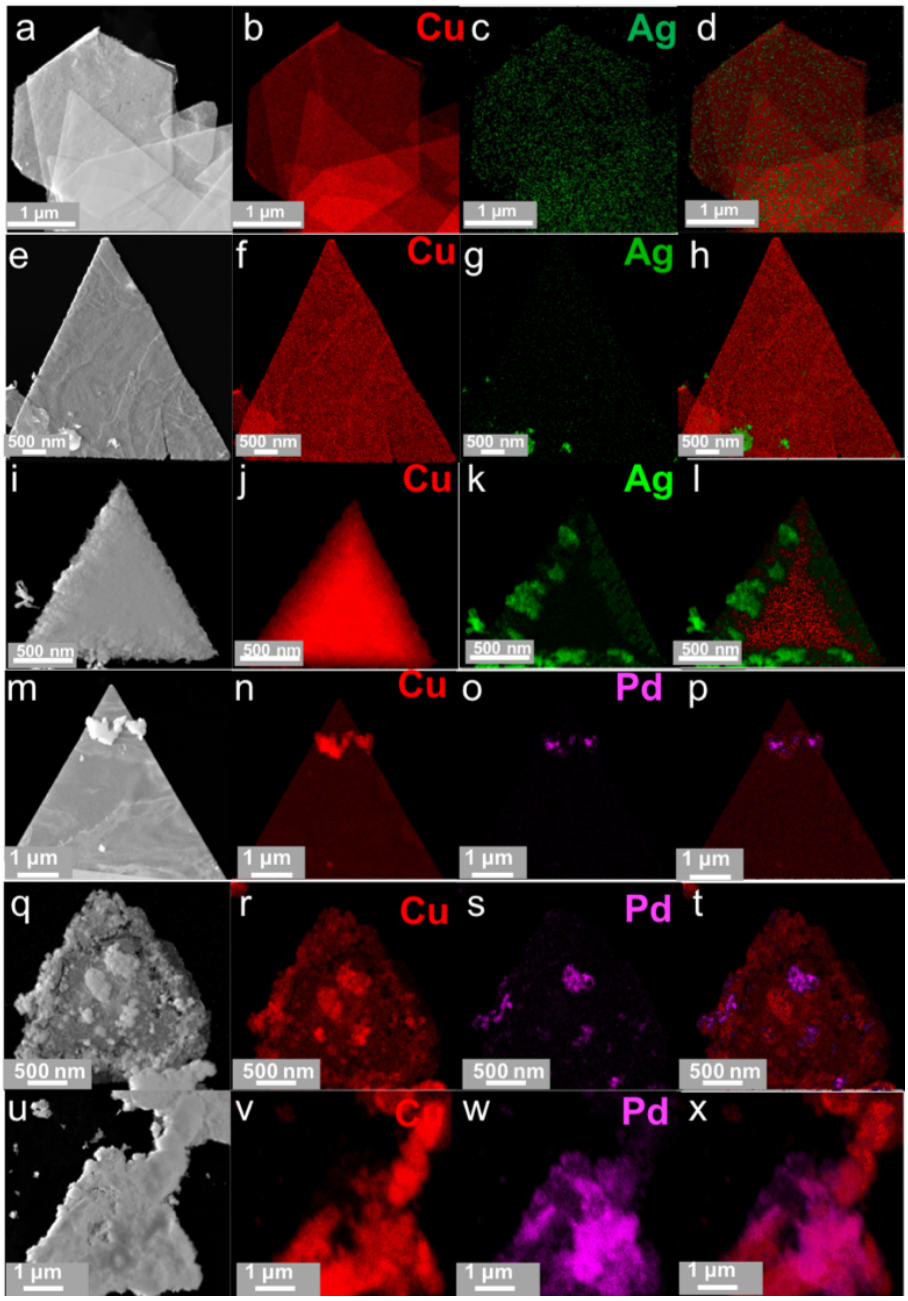


**Figure 4.4:** Electron microscopy analysis of CuAg and CuPd plates. (a,e,i,m,q,u) High-angle annular dark-field imaging (HAADF) images;(b,f,j,n,r,v) Cu component in the EDX image; (c,g,k,o,s,w) Ag component in the EDX image; (d,h,l,p,t,x) EDX mapping of Cu, Pd, and Ag L of $Cu_{99.2}Ag_{0.8}$, $Cu_{93.9}Ag_{6.1}$, $Cu_{80.3}Ag_{19.7}$, $Cu_{99.5}Pd_{0.5}$, $Cu_{97.6}Pd_{2.4}$, $Cu_{90.1}Pd_{9.9}$, respectively. Red indicates Cu, green indicates Ag, and purple indicates Pd.

preserved well with 0.8% Ag and 0.5% Pd added, whereas the uneven edge was observed with increased Ag and Pd atomic concentrations (Figure 4.4 i-l, u-x). The EDX elemental mapping images show that the growth of Pd and Ag are preferred on the edge of Cu plates (Figure 4.4). There is clear phase separation between Ag, Pd, and Cu elements on the EDX maps.

The X-ray diffraction (XRD) pattern of Cu plates in Figure 4.5a show a preferential peak at 43.3°, corresponding to the diffraction from the {111} of face-centered-cubic Cu (96-431-3212). The preferential {111} diffraction peak indicates {111} basal plane exposure of Cu plates.In addition, Cu nps shows a polycrystal diffraction pattern with prominent peaks at 43.3°, 50.5°, and 74.1°, 90.0° assigned to the diffraction from the {111}, {200}, {220}, and {311} Cu planes (96-901-3015). The XRD peaks of CuAg, CuPd, and CuPdAg plates indicate no Bragg angle shift of Cu {111} after the galvanic replacement (Figure 4.5b), which indicates no strain forming in Cu lattice after growing Ag and Pd. Ag {111} diffraction peak at 38.2° is only observed in $Cu_{80.3}Ag_{19.7}$ (Figure 4.5a), and Pd {111} diffraction peak is only observed in $Cu_{90.1}Pd_{9.9}$ illustrates more replacements of Ag and Pd, respectively. As the presence of Ag in CuAg plates and Pd in CuPd plates are confirmed by the ICP, XPS, and EDX test, the volume ratio of Ag in $Cu_{99.2}Ag_{0.8}$, $Cu_{93.9}Ag_{6.1}$, and Pd in $Cu_{97.6}Pd_{2.4}$ and $Cu_{90.1}Pd_{9.9}$ might fall below the detection limit of XRD (5–10%)[23]. We observe peaks of $Cu_2O$ {111} at 36.5° ascribed to the partial oxidation of Cu in the air during sample preparation.

We conducted the $CO_2$RR electrochemical test of catalysts in an H-cell, analyzing the gases and liquid products at constant potentials range between 0.9 and 1.2 V vs. RHE in $CO_2$-saturated 0.1 M $KHCO_3$ (pH = 6.8) at room temperature and under atmospheric pressure. The performance of the bimetallic and trimetallic plates was compared with Cu plates and those of commercial Cu nps (Figure 4.6). Hereafter, comparisons between cathodic (partial) current densities will refer to their magnitude only. The main $CO_2$RR products are gas-phase products, including CO, $CH_4$, $C_2H_4$, and hydrogen ($H_2$), the following discussion

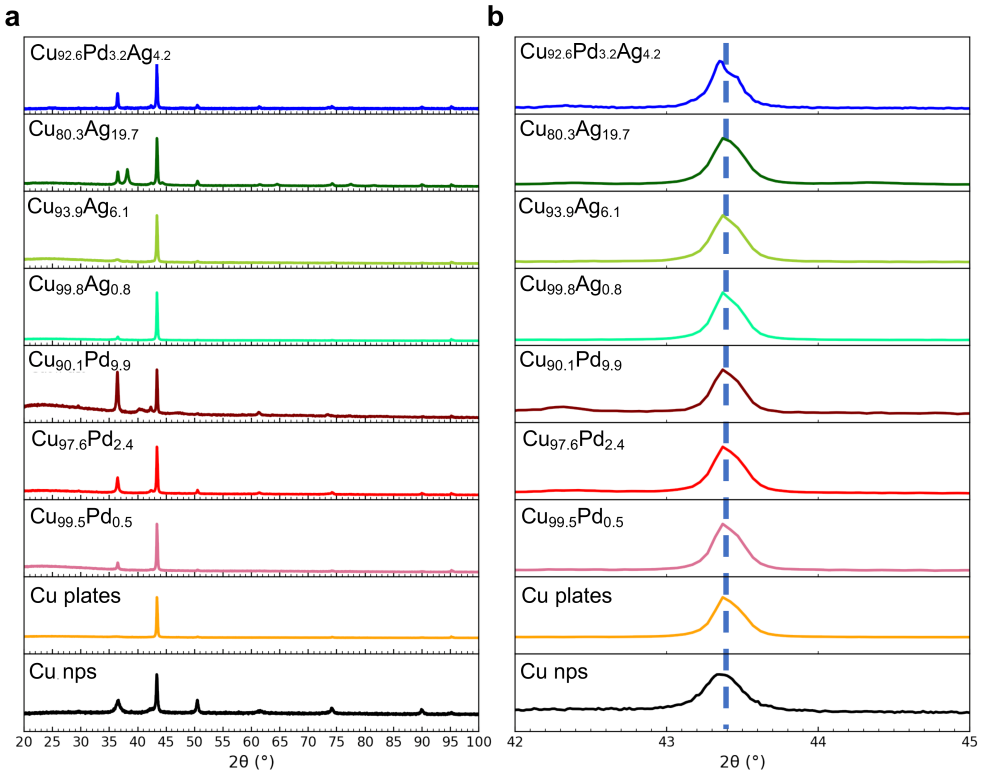


**Figure 4.5:** (a) X-ray diffraction (XRD) of Cu nps, Cu plate, $Cu_{99.2}Ag_{0.8}$, $Cu_{93.9}Ag_{6.1}$, $Cu_{80.3}Ag_{19.7}$, $Cu_{99.5}Pd_{0.5}$, $Cu_{97.6}$Pd2.4, $Cu_{90.1}Pd_{9.9}$ and $Cu_{92.6}Pd_{3.2}Ag_{4.2}$. (b) Zoomed in (111) diffraction peak of (a).

of the $CO_2$RR performances will be focused on gas-phase products. First, we observed that Cu plates showed lower hydrogen evolution reaction (HER) selectivity and $H_2$ partial current density at -0.9 V, with 34.3 ± 1.2% of $FE_{H_2}$ and -0.08 ± 0.01 mA/cm$^2$ of $j_{H2}$, compared to 66.3 ± 6.6% of $FE_{H_2}$ and -0.19 ± 0.04 mA/cm$^2$ of $j_{H_2}$ on Cu nps (Figure 4.6a and Figure 4.7a). The Cu nps possess a higher density of low-coordinated atoms compared to larger Cu plates with dominated (111) surface exposure. The reduced adsorption of hydrogen (the Volmer reaction) on Cu ($H^+ + e^- + * \rightarrow H_{ad}$) is the rate-determining step of the overall electrochemical HER,[24,25] and is limited by the weak hydrogen binding on Cu[26]. Since stronger chemisorption of protons is expected on low-coordinated atoms, the observed increase in hydrogen production, selectivity, and overall Faradaic activity for Cu nps appear plausible. The Cu plates showed a considerably higher yield of $CH_4$ with an average peak $FE_{CH_4}$ of 65.51 ± 9.5% at around 1.20 V when compared with the Cu nps ($FE_{CH_4}$ = 19.5 ± 2.3%) (Figure 4.6c and Figure 4.7c). We note that the primary $CO_2$RR products of the Cu nps were found to be $C_2H_4$ (around 40%) at 1.1 and -1.2 V (Figure 4.6d), which could be the result of the higher (100) facets (Figure 4.5a) and step sites exposure on the surface. It is well known that $CO_2$RR (111) favors the production of $CH_4$ while (100) is selective toward $C_2H_4$.[27] The discrepancy of hydrocarbons distribution among Cu plates and Cu nps is likely originating from the (111) facets distribution on Cu plates and increased amount of (100) on Cu nps.

When incorporating Ag with Cu plates, HER selectivity is significantly suppressed. With 0.8% Ag, the $FE_{H_2}$ decreased from 34.3 ± 1.2% on Cu plates to 23.6 ± 1.8% on $Cu_{99.2}Ag_{0.8}$ (Figure 4.6a), which is consistent with the assumption that the weak binding of hydrogen on Ag decreased the overall hydrogen binding strength on CuAg plates. It is well known that Ag is a CO-generating catalyst.[28] As Ag content increases, the CO production is drastically promoted at -0.9 V (Figure 4.6b). For 19.7% Ag, the FE of CO reach 88.2 ± 2.1% at -0.9 V, increased by 3-fold compare to copper plates (31.7 ± 5.7%) and the CO partial current density reached 0.5 ± 0.1 mA/cm$^2$ at -1.2 V, increased by 5-fold compare to copper plates

($0.1 \pm 0.02$ mA/cm$^2$) (Figure 4.7b). What's more, incorporating Ag into Cu plates reduced the onsite potential for hydrocarbons ($CH_4$ and $C_2H_4$) and enhanced $C_2H_4$ production. On Cu plates, $CH_4$ and $C_2H_4$ were produced starting at -1.1 V. While on $Cu_{99.2}Ag_{0.8}$, $3.4 \pm 3.2\%$ of $FE_{CH_4}$ and $24.0 \pm 6.0\%$ of $FE_{C_2H_4}$ were observed at -1.0 V. This indicates the reduced kinetic barrier for $CH_4$ and $C_2H_4$ by Ag co-catalysts. It has been reported that the rate-limiting step toward $CH_4$ on Cu(111) is the protonation of $*$CO, forming $*$COH or $*$CHO.[29,30]. For $C_2H_4$ production, $*$COH and/or $*$CHO are necessary reaction intermediates for C-C coupling on the same facet.[31] Therefore, we hypnosis that the dominant hydrocarbon production on CuAg plates is due to the tandem catalysis mechanism. The increasing amount of CO produced by Ag near the Cu surface and the relatively short diffusion length lead to a high CO coverage on Cu. It has been reported that adsorbate-adsorbate interactions of $*$CO typically reduce their adsorption energies.[32] Thus, the high local concentration of $*$CO near the Ag and Cu interface and stronger binding of CO stabilize adsorbed $*$CO and favor more efficient protonation under this condition. However, further increasing Ag concentration from 0.8% to 6.1% and 19.7% does not enhance the $FE_{CH_4}$ and $FE_{C_2H_4}$. The product distribution shift toward CO indicates that the nearby Cu atoms cannot utilize the excess $*$CO produced by Ag with increased Ag atoms. Ag ends up competing with Cu for electrons and shifts the $CO_2$RR selectivity to CO.

Contrary to Ag, Pd exhibits strong hydrogen adsorption,[33]. On CuPd plates, HER is promoted at -0.9V. For $Cu_{90.1}Pd_{9.9}$, the $FE_{H_2}$ increased by 17.4% compared to Cu plates at -0.9V (Figure 4.6a), which is consistent with the HER activity trend predicted by hydrogen binding energy. However, at a potential more negative than -1 V, Pd promotes $C_2H_4$ selectivity. Among CuPd plates, $FE_{C_2H_4}$ peaks on $Cu_{97.6}Pd_{2.4}$ reached $44.8 \pm 0.3\%$ at -1.2 V. Previously experiments reported that DFT calculations showed that the CuPd interface could enhance the $CO_2$ adsorption and decrease the hydrogenation energy barrier, which is the rate-limiting step for $*$CO.[34] Previous research reported that Pd could facilitate the hydrogenation of $*$CO to $*$CHO intermediates through Diffuse Reflectance Infrared Fourier

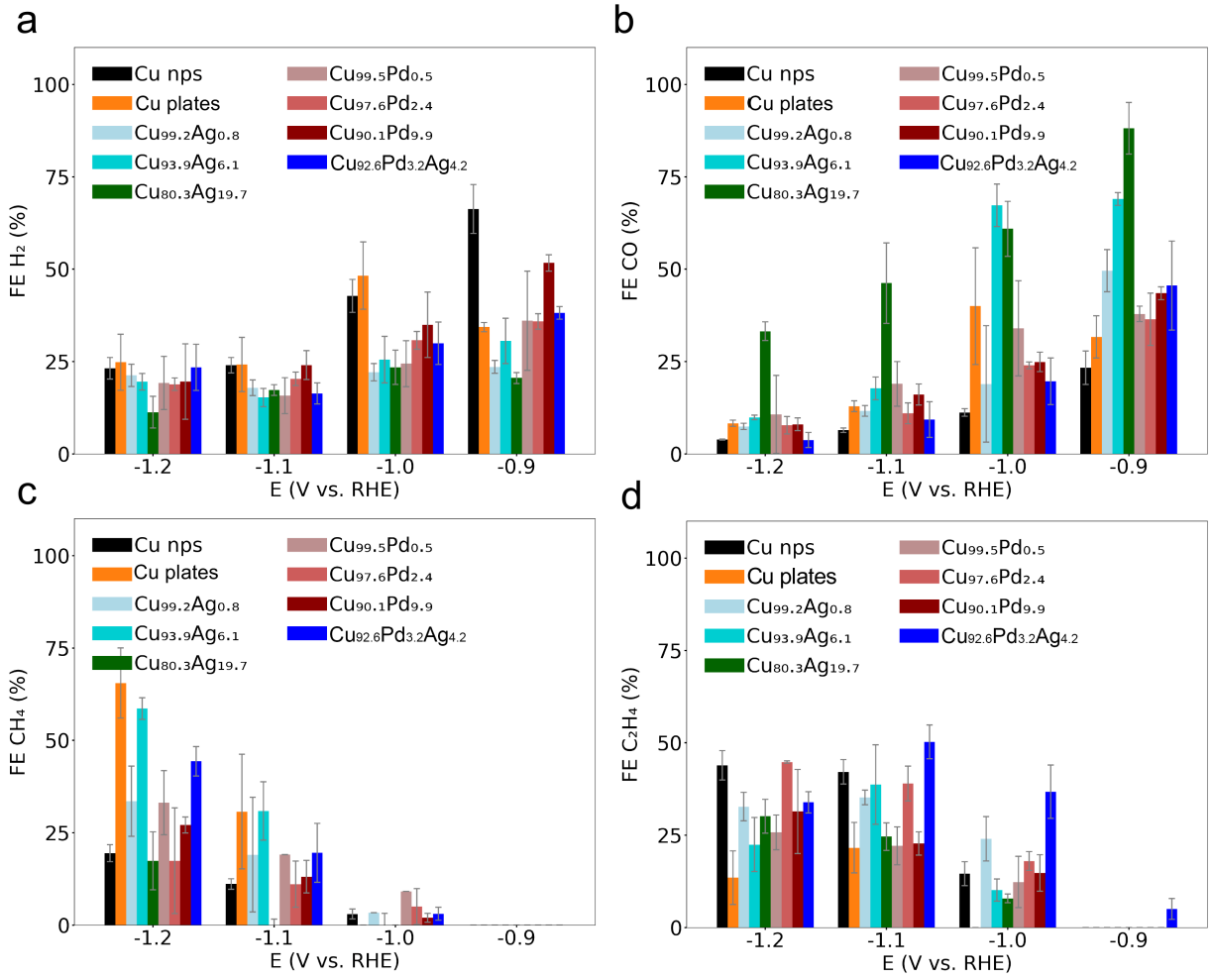


**Figure 4.6:** Comparisons of $CO_2$RR products selectivity of Cu nps, Cu plate, $Cu_{99.2}Ag_{0.8}$, $Cu_{93.9}Ag_{6.1}$, $Cu_{80.3}Ag_{19.7}$, $Cu_{99.5}Pd_{0.5}$, $Cu_{97.6}$Pd2.4, $Cu_{90.1}Pd_{9.9}$ and $Cu_{92.6}Pd_{3.2}Ag_{4.2}$ catalysts in H-cell with 0.1 M $KHCO_3$ electrolyte at room temperature and atmospheric pressure. (a) FE of $H_2$, (b) FE of CO, (c) FE of $CH_4$, (d) FE of $C_2H_4$.

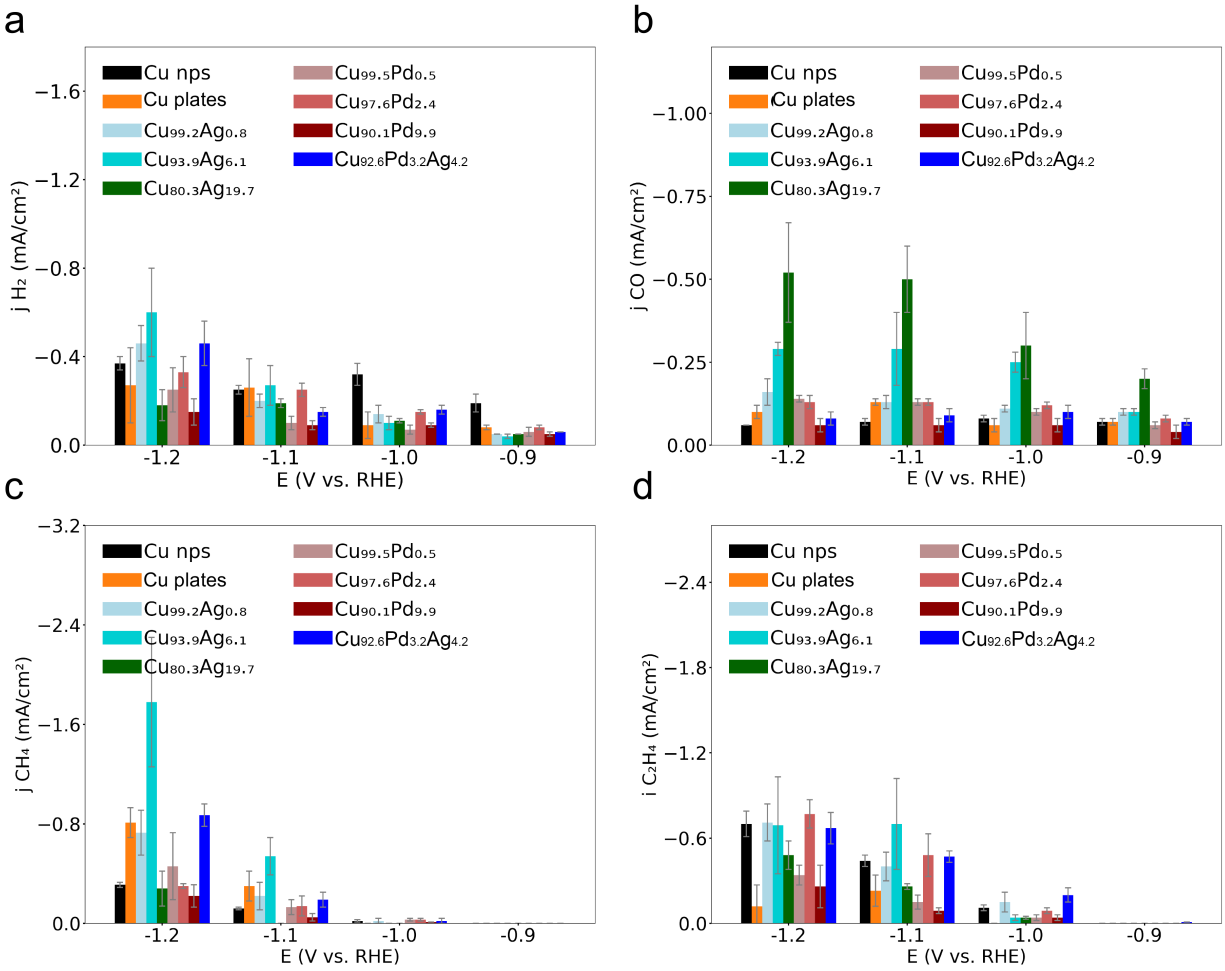


**Figure 4.7:** Comparison of catalytic $CO_2$RR activity of Cu nps, Cu plate, $Cu_{99.2}Ag_{0.8}$, $Cu_{93.9}Ag_{6.1}$, $Cu_{80.3}Ag_{19.7}$, $Cu_{99.5}Pd_{0.5}$, $Cu_{97.6}$Pd2.4, $Cu_{90.1}Pd_{9.9}$ and $Cu_{92.6}Pd_{3.2}Ag_{4.2}$ catalysts in H-cell with 0.1 M $KHCO_3$ electrolyte at room temperature and atmospheric pressure. (a) $H_2$ partial current density $j_{H_2}$, (b) CO partial current density $j_{CO}$, (c) $CH_4$ partial current density $j_{CH_4}$, (d) $C_2H_4$ partial current density $j_{C_2H_4}$. All current densities are normalized by ECSA area.

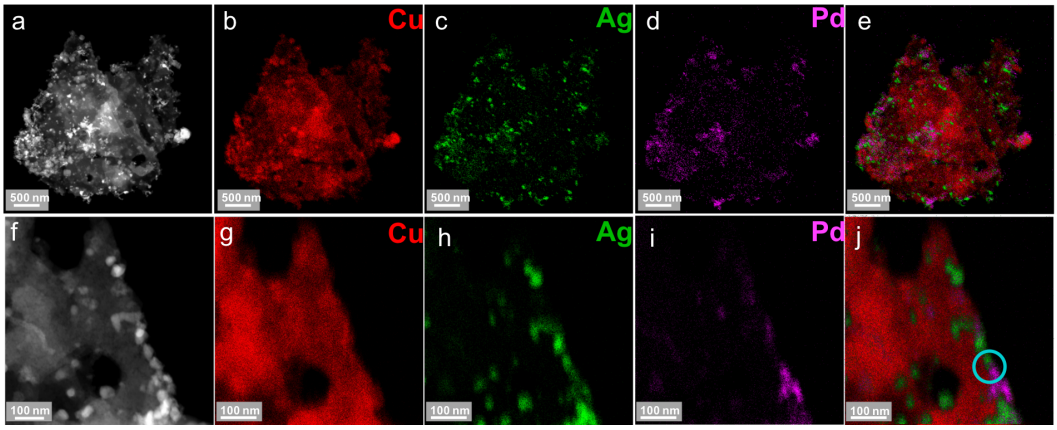


**Figure 4.8:** Electron microscopy analysis of $Cu_{92.6}Pd_{3.2}Ag_{4.2}$ plates. (a,f) High-angle annular dark-field imaging (HAADF) images;(b,g) Cu component in the EDX image; (c,h) Ag component in the EDX image; (d,i) Pd component in the EDX image (e,j) EDX mapping of Cu K, Pd L, and Ag L on $Cu_{92.6}Pd_{3.2}Ag_{4.2}$. The blue circle areas with CuPdAg ensemble. Red indicates Cu, green indicates Ag, and purple indicates Pd.

Transform Spectroscopy (DRIFTS) study.[35] Therefore, we assume the improved $FE_{C_2H_4}$ on CuPd plates is a result of the reduced kinetic barrier to $*$CO and $*$CHO. Similar to Cu co-catalyst with Ag, further increase the amount of secondary element, i.e., Pd atomic ratio to 9.9% reduce the $FE_{C_2H_4}$ in all applied potential range compared to $Cu_{97.6}Pd_{2.4}$ (Figure 4.6d). Therefore, we suspect that the co-catalyst elements need to be aligned with Cu in an optimum manner with dominant neighboring Cu atoms to maximize the synergistic effect toward $C_2$ production and diminish the competition.

To this end, we thought Ag and Pd likely function in separate steps of $C_2H_4$ production. Ag supplies $*$CO to Cu, and Pd facilitates the hydrogenation of $*$CO to $*$CHO. Therefore, we incorporate these two elements with Cu synthesizing trimetallic $Cu_{92.6}Pd_{3.2}Ag_{4.2}$ plates to enhance the synergistic effect. The structure analysis is shown in figure 4.8. EDX mapping reveals that Pd, Ag, and Cu are phase separated. Figure 4.8j show the presence of the three elements interface. XRD patterns of $Cu_{92.6}Pd_{3.2}Ag_{4.2}$ showed a dominant Cu {111} diffraction peak confirming the (111)-exposed plate morphology of the trimetallic

sample. The $CO_2RR$ performance of $Cu_{92.6}Pd_{3.2}Ag_{4.2}$ plates were tested under the same condition described before (Figure 4.6, Figure 4.7). Interestingly, we observe $C_2H_4$ production on $Cu_{92.6}Pd_{3.2}Ag_{4.2}$ at -0.9 V, the lowest among all Cu and Cu bimetallic samples. The $Cu_{92.6}Pd_{3.2}Ag_{4.2}$ plates showed a higher selectivity of $C_2H_4$ with an average peak $FE_{C_2H_4}$ of 50.3 ± 4.6% at around 1.1 V which increased by 28.7% compare to Cu plates ($FE_{C_2H_4}$ = 21.63 ± 6.8% at -1.1 V), 15.0% higher that $Cu_{99.2}Ag_{0.8}$ ($FE_{C_2H_4}$ = 35.2 ± 2.0% at -1.1 V) and 11.3% higher than $Cu_{97.6}$Pd2.4 ($FE_{C_2H_4}$ = 39.0 ± 4.7% at -1.1 V) at the same potential (Figure 4.6d and Figure 4.7d).

To investigate the electronic effect of CuAg, CuPd, and CuPdAg catalysts and their relation with $CO_2RR$ product distributions, we collected the valence band spectra of all samples and analyzed the d-band centers relative to the Fermi level (Figure 4.9). Based on the d-band theory, for transition metals, the higher the d states are in energy relative to the Fermi level, the stronger the binding due to higher energy of the antibonding states.[36] The published d-band center measured by Al k$\alpha$ excitation for Cu, Pd, and Ag are 3.05, 2.09, and 5.28 eV, respectively.[37] The d-band centers we derived from Cu nps (2.98 eV) and Cu plates (3.07 eV) match the literature result. The higher d-band center of Cu nps indicates stronger ∗H and ∗CO binding on Cu nps compared to Cu plates which could explain the greater HER yield ($FE_{H_2}$ = 66.3% ± 6.7%) at -0.9 V and superior $C_2H_4$ selectivity on Cu nps ($FE_{C_2H_4}$ = 42.1% ± 3.3%). We observed that, compared to Cu plates, incorporating Pd with Cu shifts the d-band center closer to the Fermi level while incorporating Ag shifts the d-band away except for $Cu_{99.2}Ag_{0.8}$. The d-band center of $Cu_{99.2}Ag_{0.8}$ (3.00 eV) and $Cu_{97.6}Pd_{2.4}$ (3.03 eV) lay closely with Cu plates (3.07 eV) while exhibiting the highest $FE_{C_2H_4}$ among CuAg and CuPd plates respectively. Therefore, we suspect that the synergistic effect of Pd and Ag probably originated from local geometric effects rather than the alternation of the electronic structure of Cu catalysts which promotes $C_2H_4$ production in this study.

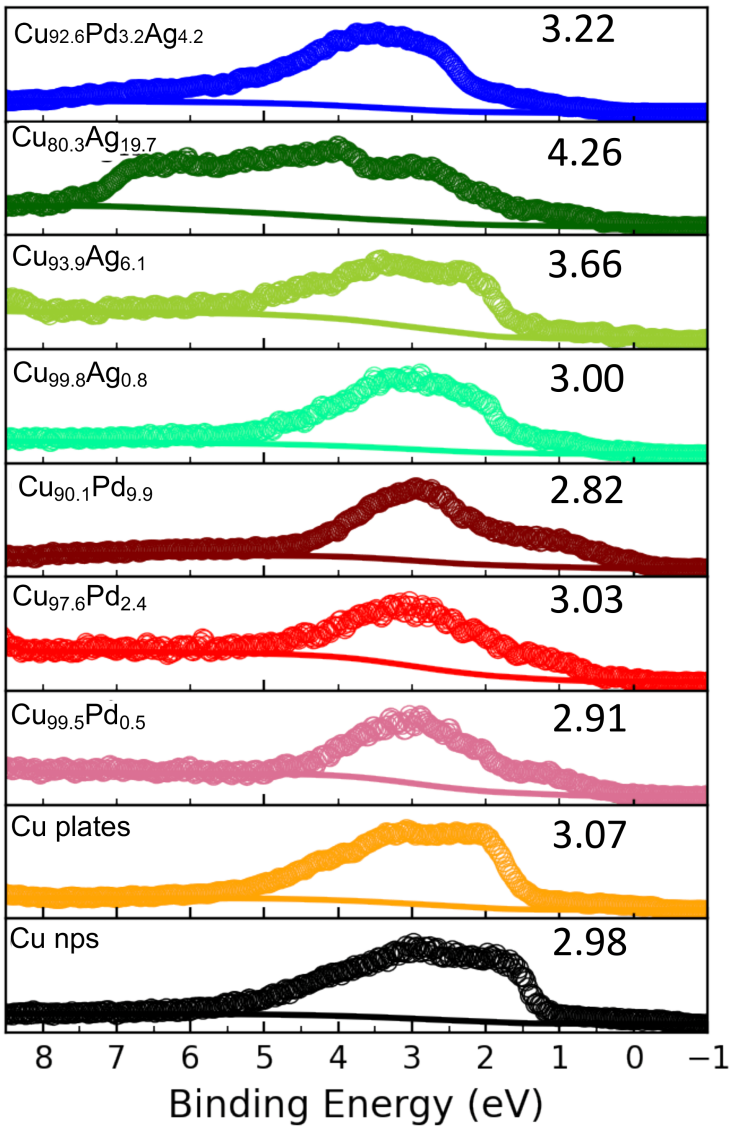


**Figure 4.9:** Valence band spectra of Cu nps, Cu plate, $Cu_{99.2}Ag_{0.8}$, $Cu_{93.9}Ag_{6.1}$, $Cu_{80.3}Ag_{19.7}$, $Cu_{99.5}Pd_{0.5}$, $Cu_{97.6}Pd_{2.4}$, $Cu_{90.1}Pd_{9.9}$ and $Cu_{92.6}Pd_{3.2}Ag_{4.2}$ measured by X-ray photoelectron spectroscopy (XPS) using monochromatized Al K excitation. The Shirley background is determined and shown as a thin line underneath each spectrum. The average energies of the valence band spectral weight (i.e., the d-band center position), derived after subtraction of the background and integration of the spectrum, are marked on the top right corner of each spectrum in eV.

## 4.4 Conclusion

In summary, through the synthesis, characterization, and electrochemical study of bimetallic CuAg, CuPd, and trimetallic CuPdAg plates with varied compositions, we demonstrate that the concentration of co-catalyst is important in determining each catalysts selectivity. The atomic ratio of a secondary element to Cu should be adjusted to optimum for the catalyst to show the most significant co-catalyst effect. We found that trimetallic Cu-based catalysts can be engineered to have active sites for key reaction intermediates with tuned binding energies aligned together for the more reduced product ($C_2H_4$). When incorporating the Ag and Pd together with Cu, $Cu_{92.6}Pd_{3.2}Ag_{4.2}$ plates outperform Cu plates, bimetallic CuAg, and CuPd plates in $C_2H_4$ production at -1 V. These findings suggest an effective way to engineer co-catalyst, not just through bimetallic structures but also through trimetallic structures, to enhance $C_2H_4$ selectivity with lower over potential.

# Bibliography


[1] Kendra P Kuhl, Etosha R Cave, David N Abram, and Thomas F Jaramillo. New insights into the electrochemical reduction of carbon dioxide on metallic copper surfaces. *Energy & Environmental Science*, 5(5):7050–7059, 2012.

[2] Lisheng Guo, Jian Sun, Qingjie Ge, and Noritatsu Tsubaki. Recent advances in direct catalytic hydrogenation of carbon dioxide to valuable $C_{2+}$ hydrocarbons. *Journal of Materials Chemistry A*, 6(46):23244–23262, 2018.

[3] Joseph H Montoya, Chuan Shi, Karen Chan, and Jens K Nørskov. Theoretical insights into a CO dimerization mechanism in $CO_2$ electroreduction. *The journal of physical chemistry letters*, 6(11):2032–2037, 2015.

[4] Younghye Kim, Sojung Park, Seung-Jae Shin, Woong Choi, Byoung Koun Min, Hyungjun Kim, Wooyul Kim, and Yun Jeong Hwang. Time-resolved observation of C–C coupling intermediates on Cu electrodes for selective electrochemical $CO_2$ reduction. *Energy & Environmental Science*, 13(11):4301–4311, 2020.

[5] Wenchao Ma, Shunji Xie, Tongtong Liu, Qiyuan Fan, Jinyu Ye, Fanfei Sun, Zheng Jiang, Qinghong Zhang, Jun Cheng, and Ye Wang. Electrocatalytic reduction of $CO_2$ to ethylene and ethanol through hydrogen-assisted c–c coupling over fluorine-modified copper. *Nature Catalysis*, 3(6):478–487, 2020.

[6] Jason D Goodpaster, Alexis T Bell, and Martin Head-Gordon. Identification of possible pathways for C–C bond formation during electrochemical reduction of $CO_2$: new theoretical insights from an improved electrochemical model. *The journal of physical chemistry letters*, 7(8):1471–1477, 2016.

[7] Chungseok Choi, Jin Cai, Changsoo Lee, Hyuck Mo Lee, Mingjie Xu, and Yu Huang. Intimate atomic Cu-Ag interfaces for high $CO_2$rr selectivity towards $CH_4$ at low over potential. *Nano Research*, 14(10):3497–3501, 2021.

[8] Jianfeng Huang, Mounir Mensi, Emad Oveisi, Valeria Mantella, and Raffaella Buonsanti. Structural sensitivities in bimetallic catalysts for electrochemical $CO_2$ reduction revealed by Ag –Cu nanodimers. *Journal of the American Chemical Society*, 141(6):2490–2499, 2019.

[9] Yuguang C Li, Ziyun Wang, Tiange Yuan, Dae-Hyun Nam, Mingchuan Luo, Joshua Wicks, Bin Chen, Jun Li, Fengwang Li, F Pelayo García de Arquer, et al. Binding site diversity promotes $CO_2$ electroreduction to ethanol. *Journal of the American Chemical Society*, 141(21):8584–8591, 2019.

[10] Thao TH Hoang, Sumit Verma, Sichao Ma, Tim T Fister, Janis Timoshenko, Anatoly I Frenkel, Paul JA Kenis, and Andrew A Gewirth. Nanoporous copper–silver alloys by additive-controlled electrodeposition for the selective electroreduction of $CO_2$ to ethylene and ethanol. *Journal of the American Chemical Society*, 140(17):5791–5797, 2018.

[11] Zhiyuan Chang, Shengjuan Huo, Wei Zhang, Jianhui Fang, and Hailiang Wang. The tunable and highly selective reduction products on Ag @ Cu bimetallic catalysts toward $CO_2$ electrochemical reduction reaction. *The Journal of Physical Chemistry C*, 121(21):11368–11379, 2017.

[12] Wenjin Zhu, Lei Zhang, Piaoping Yang, Xiaoxia Chang, Hao Dong, Ang Li, Congling Hu, Zhiqi Huang, Zhi-Jian Zhao, and Jinlong Gong. Morphological and compositional design of Pd–Cu bimetallic nanocatalysts with controllable product selectivity toward $CO_2$ electroreduction. *Small*, 14(7):1703314, 2018.

[13] Sichao Ma, Masaaki Sadakiyo, Minako Heima, Raymond Luo, Richard T Haasch, Jake I Gold, Miho Yamauchi, and Paul JA Kenis. Electroreduction of carbon dioxide to hydrocarbons using bimetallic Cu–Pd catalysts with different mixing patterns. *Journal of the American Chemical Society*, 139(1):47–50, 2017.

[14] Mu Li, Junjie Wang, Peng Li, Kun Chang, Cuiling Li, Tao Wang, Bo Jiang, Huabin

Zhang, Huimin Liu, Yusuke Yamauchi, et al. Mesoporous palladium–copper bimetallic electrodes for selective electrocatalytic reduction of aqueous $CO_2$ to CO. *Journal of Materials Chemistry A*, 4(13):4776–4782, 2016.

[15] Paul Sabatier. Hydrogénations et déshydrogénations par catalyse. *Berichte der deutschen chemischen Gesellschaft*, 44(3):1984–2001, 1911.

[16] Selwyn Hanselman, Marc TM Koper, and Federico Calle-Vallejo. Computational comparison of late transition metal (100) surfaces for the electrocatalytic reduction of CO to $C_2$ species. *ACS Energy Letters*, 3(5):1062–1067, 2018.

[17] Roland Geyer, Jenna R Jambeck, and Kara Lavender Law. Production, use, and fate of all plastics ever made. *Science advances*, 3(7):e1700782, 2017.

[18] Luis M Liz-Marzán and Marek Grzelczak. Growing anisotropic crystals at the nanoscale. *Science*, 356(6343):1120–1121, 2017.

[19] Joseph S DuChene, Wenxin Niu, John M Abendroth, Qi Sun, Wenbo Zhao, Fengwei Huo, and W David Wei. Halide anions as shape-directing agents for obtaining high-quality anisotropic gold nanostructures. *Chemistry of Materials*, 25(8):1392–1399, 2013.

[20] Jill E Millstone, Wei Wei, Matthew R Jones, Hyojong Yoo, and Chad A Mirkin. Iodide ions control seed-mediated growth of anisotropic gold nanoparticles. *Nano letters*, 8(8):2526–2529, 2008.

[21] Jin-Won Lee, Jiyoon Han, Dong Su Lee, Sukang Bae, Sang Hyun Lee, Seoung-Ki Lee, Byung Joon Moon, Chel-Jong Choi, Gunuk Wang, and Tae-Wook Kim. 2d single-crystalline copper nanoplates as a conductive filler for electronic ink applications. *Small*, 14(8):1703312, 2018.

[22] H Shinotsuka, S Tanuma, CJ Powell, and DR Penn. Calculations of electron inelastic

mean free paths. x. data for 41 elemental solids over the 50 ev to 200 kev range with the relativistic full penn algorithm. *Surface and Interface Analysis*, 47(9):871–888, 2015.

[23] Cameron F Holder and Raymond E Schaak. Tutorial on powder x-ray diffraction for characterizing nanoscale materials, 2019.

[24] Jens Kehlet Nørskov, Thomas Bligaard, Ashildur Logadottir, JR Kitchin, Jingguang G Chen, S Pandelov, and U Stimming. Trends in the exchange current for hydrogen evolution. *Journal of The Electrochemical Society*, 152(3):J23, 2005.

[25] Jeff Greeley, Jens K Nørskov, Ludwig A Kibler, Ahmed M El-Aziz, and Dieter M Kolb. Hydrogen evolution over bimetallic systems: Understanding the trends. *ChemPhysChem*, 7(5):1032–1035, 2006.

[26] Egill Skúlason, Vladimir Tripkovic, Mårten E Bjorketun, Sigrídur Gudmundsdóttir, Gustav Karlberg, Jan Rossmeisl, Thomas Bligaard, Hannes Jónsson, and Jens K Nørskov. Modeling the electrochemical hydrogen oxidation and evolution reactions on the basis of density functional theory calculations. *The Journal of Physical Chemistry C*, 114(42):18182–18197, 2010.

[27] Y Hori, I Takahashi, O Koga, and N Hoshi. Electrochemical reduction of carbon dioxide at various series of copper single crystal electrodes. *Journal of Molecular Catalysis A: Chemical*, 199(1-2):39–47, 2003.

[28] System design rules for intensifying the electrochemical reduction of $CO_T$O CO ON AG NANOPARTICLES, author=Bhargava, Saket S and Proietto, Federica and Azmoodeh, Daniel and Cofell, Emiliana R and Henckel, Danielle A and Verma, Sumit and Brooks, Christopher J and Gewirth, Andrew A and Kenis, Paul JA, journal=ChemElectroChem, volume=7, number=9, pages=2001–2011, year=2020, publisher=Wiley Online Library.

[29] Qing Zhao, John Mark P Martirez, and Emily A Carter. Revisiting understanding of electrochemical $CO_2$ reduction on Cu (111): competing proton-coupled electron transfer

reaction mechanisms revealed by embedded correlated wavefunction theory. *Journal of the American Chemical Society*, 143(16):6152–6164, 2021.

[30] Qing Zhao and Emily A Carter. Revisiting competing paths in electrochemical $CO_2$ reduction on copper via embedded correlated wavefunction theory. *Journal of Chemical Theory and Computation*, 16(10):6528–6538, 2020.

[31] Ling Chen, Cheng Tang, Yan Jiao, and Shi-Zhang Qiao. Anomalous C–C coupling on under-coordinated Cu (111): A case study of Cu nanopyramids for $CO_2$ reduction reaction by molecular modelling. *ChemSusChem*, 14(2):671–678, 2021.

[32] Adam C Lausche, Andrew J Medford, Tuhin Suvra Khan, Yue Xu, Thomas Bligaard, Frank Abild-Pedersen, Jens K Nørskov, and Felix Studt. On the effect of coverage-dependent adsorbate–adsorbate interactions for CO methanation on transition metal surfaces. *Journal of catalysis*, 307:275–282, 2013.

[33] Xinyan Liu, Jianping Xiao, Hongjie Peng, Xin Hong, Karen Chan, and Jens K Nørskov. Understanding trends in electrochemical carbon dioxide reduction rates. *Nature communications*, 8(1):1–7, 2017.

[34] Li Zhu, Yiyang Lin, Kang Liu, Emiliano Cortés, Hongmei Li, Junhua Hu, Akira Yamaguchi, Xiaoliang Liu, Masahiro Miyauchi, Junwei Fu, et al. Tuning the intermediate reaction barriers by a CuPd catalyst to improve the selectivity of $CO_2$ electroreduction to c2 products. *Chinese Journal of Catalysis*, 42(9):1500–1508, 2021.

[35] Shuxing Bai, Qi Shao, Pengtang Wang, Qiguang Dai, Xingyi Wang, and Xiaoqing Huang. Highly active and selective hydrogenation of $CO_2$ to ethanol by ordered Pd–Cu nanoparticles. *Journal of the American Chemical Society*, 139(20):6827–6830, 2017.

[36] Jens K Nørskov, Frank Abild-Pedersen, Felix Studt, and Thomas Bligaard. Density functional theory in surface chemistry and catalysis. *Proceedings of the National Academy of Sciences*, 108(3):937–943, 2011.

[37] Timo Hofmann, Ted H Yu, Michael Folse, Lothar Weinhardt, Marcus Bar, Yufeng Zhang, Boris V Merinov, Deborah J Myers, William A Goddard III, and Clemens Heske. Using photoelectron spectroscopy and quantum mechanics to determine d-band energies of metals for catalytic applications. *The Journal of Physical Chemistry C*, 116(45):24016–24026, 2012.

# CHAPTER 5

# Conclusion and Perspective

## 5.1 Conclusion

In summary, during my Ph.D. study, I researched and designed high-performance Cu-based catalysts for electrochemical $CO_2$ reduction reactions, including Cu foil with rich twin boundaries (tw-Cu); Cu-Ag NWs with the atomically intimate interface; and trimetallic CuPdAg plates.

In chapter 2, I introduced a highly-(111)-oriented Cu foil electrocatalyst with dense twin boundaries (TB) (tw-Cu) that showed high Faradaic efficiency of 86.1 $\pm$ 5.3% towards $CH_4$ at -1.2 $\pm$ 0.02 V vs. the reversible hydrogen electrode (RHE). Theoretical studies suggested that tw-Cu can significantly lower the reduction barrier for the rate-determining hydrogenation of CO compared to planar Cu(111) under working conditions, which suppressed the competing C-C coupling step, leading to the experimentally observed high $CH_4$ selectivity. Through this work, I developed a catalyst showing high $CO_2$RR selectivity towards $CH_4$ production and a mechanistic understanding of the influence of the twin-boundaries on $CO_2$RR selectivity, thus opening a path towards the rational design of Cu-based catalysts for tunable $CO_2$RR.

In chapter 3, I report the generation of a co-catalyst with intimate atomic Cu-Ag interfaces on the surface of Cu nanowires via galvanic replacement from Cu to Ag and following in-situ electrochemical activation to produce $CH_4$ with high efficiency. The attractive Cu-Ag interface showed a 63.3 $\pm$ 4.9% $FECH_4$ at -1.1 $\pm$ 0.01 V vs. RHE, and an impressive maximum $FE_{CH_4}$ of 72% at a low potential of -1.2 V. Well-integrated experimental measurements

supported that the atomic Cu-Ag interfaces were responsible for the high $CH_4$ selectivity. This investigation opens the path toward designing atomically intimate Cu co-catalyst interfaces for $CO_2$RR.

In Chapter 4, taking a step further in co-catalyst design on Cu, I incorporated Pd and Ag with Cu plates with various atomic ratios. I demonstrate that co-catalyst concentration is important in determining each catalyst's selectivity and should be adjusted to the optimum. I further designed the trimetallic catalyst ($Cu_{92.6}Pd_{3.2}Ag_{4.2}$ plates), aligning weak $*$CO binding element (Ag) and strong $*$CO binding element (Pd) together to produce $C_2H_4$ selectively. $Cu_{92.6}Pd_{3.2}Ag_{4.2}$ plates outperform Cu plates, bimetallic CuAg, and CuPd plates in $C_2H_4$ production at -1V. These findings suggest efficacious design strategies for coupling Cu with a secondary metal to reduce the activation barriers for $C_2H_4$.

## 5.2 Perspective

As described throughout this thesis, the advancement of design catalysts with superior activity and selectivity for deeply reduced products with high energy density is a critical focus of electrochemical $CO_2$ reduction. To design catalysts that show high performance of $CO_2$RR, a better understanding of the reaction mechanism is required for guidance. The obstacle to understanding the mechanism is the complexity of $CO_2$RR. $CO_2$RR includes multiple steps and key intermediate. Reaction pathways are determined not only by the catalyst structure but also by the electrolyzer environment (applied potential, PH, cation concentration, $CO_2$ concentration, etc.), which leads to enormous possibilities to consider, especially for deeply reduced products ($C_{2+}$). As a graduate student, the more I dig into this reaction, the more I realize the complexity and the necessity of utilizing simulation and in situ/operando spectroscopy to measure events occurring at the surface under operating conditions. To date, DFT simulation, which is largely used in the $CO_2$ mechanism study, still suffers from the limited capability of describing charge at the catalyst-electrolyte interface and evaluating

kinetics and reaction barriers under reaction conditions. Questions including what are the protonation steps that convert $*CO$ into $CH_4$ and detailed $C_2$ routes remain open. Therefore, combining in situ/operando spectroscopy with high space and time resolution and advanced microkinetic modeling together is necessary to complete the $CO_2$RR reaction mechanism map.

A deep understanding of the reaction mechanism will accelerate the rational design of $CO_2$RR electrocatalysts and save researchers from the traditional trial-and-error approach. The development of machine learning also presents an opportunity to screen and predict materials while it needs reliable data engineering of the experiment reports. Building a database with well-defined and standardized experimental results of catalyst performance will accelerate statistical understanding and boost reliable model training for catalyst screening.

The other issue of catalyst development is the precise control of the catalyst's structure, both in ex-situ and in-situ electrochemical conditions. In other words, the specific activation site for each elementary step should be assembled optimally and performed stably to achieve the most efficient generation, transformation, and consumption of intermediates on the catalyst. This likely requires the synthesis of elaborate structures that go beyond a single crystal or single element.

Besides the catalyst, it is important to realize other critical electrolyzer system aspects, such as electrolyte condition, ion exchange membrane engineering, gas diffusion layer design, and process conditions. For scaled-up electrolyzers, the uniform delivery of electricity field, efficient heat transfer (prevent overheating), and control of cell pressure condition should also be optimized for effective and durable operation.

In summary, rapid progress has been made in understanding and improving the catalyst performance of electrochemical $CO_2$ reduction in recent years. Multiple independent techno-economic assessments suggest that with the state-of-the-art electrolyzer performance, carbon monoxide and formic acid production costs are already competitive with conventional processes.[1] With the ever-increasing avenues of fundamental understanding followed by the

efficient catalyst and electrolyzer development, there are reasons to believe the step approaching industrialized electrochemical $CO_2$ reduction will continue.

## Bibliography

[1] Haeun Shin, Kentaro U Hansen, and Feng Jiao. Techno-economic assessment of low-temperature carbon dioxide electrolysis. *Nature Sustainability*, 4(10):911–919, 2021.